HEDL-TME 80-85
UC-70

DATA SUMMARY REPORT FOR THE DESTRUCTIVE EXAMINATION OF RODS G7, G9, J8, I9, AND H6 FROM TURKEY POINT FUEL ASSEMBLY B17

Hanford Engineering Development Laboratory

R.B. Davis
V. Pasupathi*

April 1981

*Battelle Columbus Laboratories

HANFORD ENGINEERING DEVELOPMENT LABORATORY
Operated by Westinghouse Hanford Company
P.O. Box 1970 Richland, WA 99352
A Subsidiary of Westinghouse Electric Corporation
Prepared for the U.S. Department of Energy
under Contract No. DE-AC14-76FF02170.

DISCLAIMER

HEDL-TME 80-85
UC-70

DATA SUMMARY REPORT FOR THE DESTRUCTIVE EXAMINATION OF RODS G7, G9, J8, I9, AND H6 FROM TURKEY POINT FUEL ASSEMBLY B17

R. B. Davis
V. Pasupathi

ABSTRACT

Destructive examination results of five spent fuel rods from a Turkey Point Unit 3 pressurized water reactor are reported. Examinations included fission gas analysis, cladding hydrogen content analysis, fuel burnup analysis, metallographic examination, autoradiography and shielded electron microprobe analysis. All rods were found to be of sound integrity with an average burnup of 27 GWd/MTU and a 0.3% fission gas release.

CONTENTS

CONTENTS (Cont'd)

FIGURES

FIGURES (Cont'd)

FIGURES (Cont'd)

FIGURES (Cont'd)

TABLES

DATA SUMMARY REPORT FOR THE DESTRUCTIVE EXAMINATION OF RODS G7, G9, J8, I9, AND H6 FROM TURKEY POINT FUEL ASSEMBLY B17

I. SUMMARY

This document summarizes the results of the destructive examination of five fuel rods from a spent fuel assembly from the Turkey Point Unit 3 pressurized water reactor (PWR). The work was conducted at the Battelle Columbus Laboratories (BCL) under the direction of the Hanford Engineering Development Laboratory (HEDL). Procedures and techniques used in this examination were developed by BCL.[1] The examination was conducted to document the internal condition of these fuel rods quantitatively and qualitatively. The results, in combination with nondestructive examination results, establish a pretest baseline condition of a batch of 20 fuel rods from sibling fuel assemblies presently in dry surface storage demonstration (DSSD) tests. Upon completion of the DSSD tests, the sibling rods will be destructively examined in a similar manner. Comparison of posttest results to the pretest condition will enable the evaluation of test rod performance during storage testing.

Destructive examinations included fission gas analysis and rod void volume measurements, metallographic examination, fuel burnup analysis, cladding hydrogen content analysis, autoradiography, and shielded electron microprobe analysis.

The rod condition was found to vary more with axial location than from rod-to-rod. All five rods were found to be of good integrity. The fission gas was analyzed to have an approximate 0.3% fission gas release. Metallography of surfaces from 21 samples showed no abnormalities. The fuel showed no evidence of restructuring and there were few cracks and relatively large pieces of fuel. Reaction product layers on the cladding inner surface ranged from 5 to 40 microns in thickness. Zirconium hydrides were oriented longitudinally and circumferentially in the cladding. Oxide thickness

layers on the cladding outer surface were found to vary in average thickness from 0.00015 to 0.00070 inch along the rod and average cladding width varied from 0.0242 to 0.0248 inch along the rod. The peak fuel burnup was determined to be approximately 27,000 MWd/MTU at 70 inches from the bottom of the fuel rod. The maximum cladding hydrogen content was found to vary axially, increasing towards the upper end with the maximum value of 77 ppm. Autoradiography showed no gross redistribution of uranium or plutonium in the fuel. Microprobe analysis found several iron-nickel-chromium impurities in the fuel and a uranium, cerium, molybdenum, and cesium reaction product on the cladding inner surface. In addition to the aforementioned examinations and analyses, stress rupture testing is planned for sections of the cladding to establish mechanical properties.

II. INTRODUCTION

This work was conducted as part of the Department of Energy's (DOE) National Waste Terminal Storage program under the management of the Office of Nuclear Waste Isolation (ONWI). A primary objective of the program is to develop and demonstrate the technology for safe disposal of nuclear waste including spent commercial reactor fuel. A major HEDL objective is to develop a performance prediction model for spent fuel disposal to support disposal technology and licensing of nuclear waste disposal repositories.

Performance modeling is based on data obtained from field disposal and in separate laboratory tests. Performance is established by comparing pre- and posttest conditions, which are qualified and quantified by a series of nondestructive and destructive tests conducted on the fuel assemblies and rods at BCL. The fuel assemblies used for demonstration testing are nondestructively examined prior to testing followed by posttest nondestructive and destructive examinations. A companion fuel assembly with nearly identical fabrication and operating characteristics is nondestructively and destructively examined as part of the pretest characterization. Pretest nondestructive and destructive data from the companion assembly serve to establish the pretest condition of the demonstration assemblies. The pretest condition will be compared to the posttest condition to establish and quantify changes that occur as a result of demonstration testing.

This document summarizes the data from the pretest destructive examination of five rods (G7, G9, H6, J8, and I9) from the companion fuel assembly B17. It does not attempt to evaluate the condition of the fuel but does serve to document the data obtained. It was not practicable to include all the data in their original form; consequently, only a summary of the data obtained is presented. The original data are being maintained by the Spent Fuel Research and Development group at HEDL.

III. FUEL HISTORY AND CHARACTERISTICS

The five fuel rods that are the subject of this report were removed from a fuel assembly used during the first two reactor operating cycles at the Turkey Point Unit 3 power station. The reactor is of Westinghouse design and is owned and operated by Florida Power and Light. This fuel assembly was a companion fuel assembly to four others with nearly identical operating and fabrication histories that are currently in field disposal tests at the Nevada Test Site. Table 1 lists reactor operating statistics for all five fuel assemblies; Table 2 lists pertinent fabrication statistics.

TABLE 1

TURKEY POINT UNIT 3 OPERATING STATISTICS
DURING THE FIRST TWO CYCLES OF OPERATION

Date Charged	January 12, 1972
Date Discharged	November 25, 1975
Irradiation Time	827 Effective Full-Power Days
Reactor Average Thermal Power	13.96 MW/Assembly
Reactor Operating Power Density	82.6 kW/Liter
Core Average Linear Power	182 W/cm
Core Peak-to-Average Power Ratio	1.141
Core Average Burnup	25,665 MWd/MTU
Core Peak Burnup	28,564 MWd/MTU

TABLE 2

FABRICATION STATISTICS FOR TURKEY POINT
FUEL ASSEMBLIES B02, B03, B17, B41, AND B43

Vendor		Westinghouse Electric Corp.
Type (rod array)		15 x 15
Assembly Parameters		
Transverse Dimension		8.426 in.
Assembly Weight		1,420 lb
Assembly Length		161.3 in.
Guide Tubes:	Number	20
	Upper OD	0.544 in.
	Lower OD	0.489 in.
	Wall Thickness	0.017 in.
	Material	Zr-4
Instrument Tubes:	Number	1
	OD	0.544 in.
	Wall Thickness	0.017 in.
	Material	Zr-4
Spacer Grids:	Number	7
	Material	Inconel 718
	Spring Material	Inconel 718
Fuel Rods:	Number	204
	Length	152.0 in.
	OD	0.422 in.
	Wall Thickness	0.0243 in.
	Material	Zr-4
	Fuel Length	144.0 in.
	Prepressurization	335 psig He
Orifice Plate Material		304 SS
Plenum Springs:	Working Length	6.80 in.
	Material	Inconel 718
Fuel Pellet:	Material	UO_2
	Enrichment	2.559 wt% ^{235}U
	Density	92% theoretical
	Weight/Assembly	0.448 MTU

IV. A REVIEW OF NONDESTRUCTIVE EXAMINATION RESULTS

Nondestructive examination results for the fuel assemblies and rods were reported previously.[2] A brief review of the findings on these five rods is provided below.

The fuel assembly sip test indicated all rods from assembly B17 to be of sound integrity. The visual examination showed three general regions of rod surface appearance: a dark adherent "crud" layer at the bottom of the rod, black spalling crud layers in the middle, and a spotty gray loose powdery coating with dark crud or oxide underneath towards the top. Rod lengths varied from 152.395 to 152.707 inches. Maximum rod box measurements for rods G9, I9, and G7 were 0.038 to 0.040 inch and 0.022 inch for rods H6 and J8. Results from profilometry scans showed the maximum ovality for these five rods to be 0.0066 inch with average diameters ranging from 0.4187 to 0.4198 inch. Extensive ridging from pellet-cladding interaction over the entire length was evident on all rods. Gamma scan results showed no cesium peaking and no pellet gaps greater than 0.025 inch. No unusual areas were seen in the eddy current results other than ridging and possible fuel-cladding bonding.

V. DESTRUCTIVE EXAMINATION

The destructive examination served to document the internal condition of the fuel rods qualitatively and quantitatively. The examinations and analyses were chosen for longtime reproducibility and to provide data sensitive to the level of changes thought to occur on the basis of the proposed storage degradation mechanisms.

The specific examinations included fission gas collection and analysis, void volume determination, prepuncture rod pressure calculation, metallographic examination of the fuel and cladding, burnup analysis, autoradiography, hydrogen analysis, and shielded electron microprobe analysis. A process flow diagram indicating the sequence of examinations is presented in Figure 1.

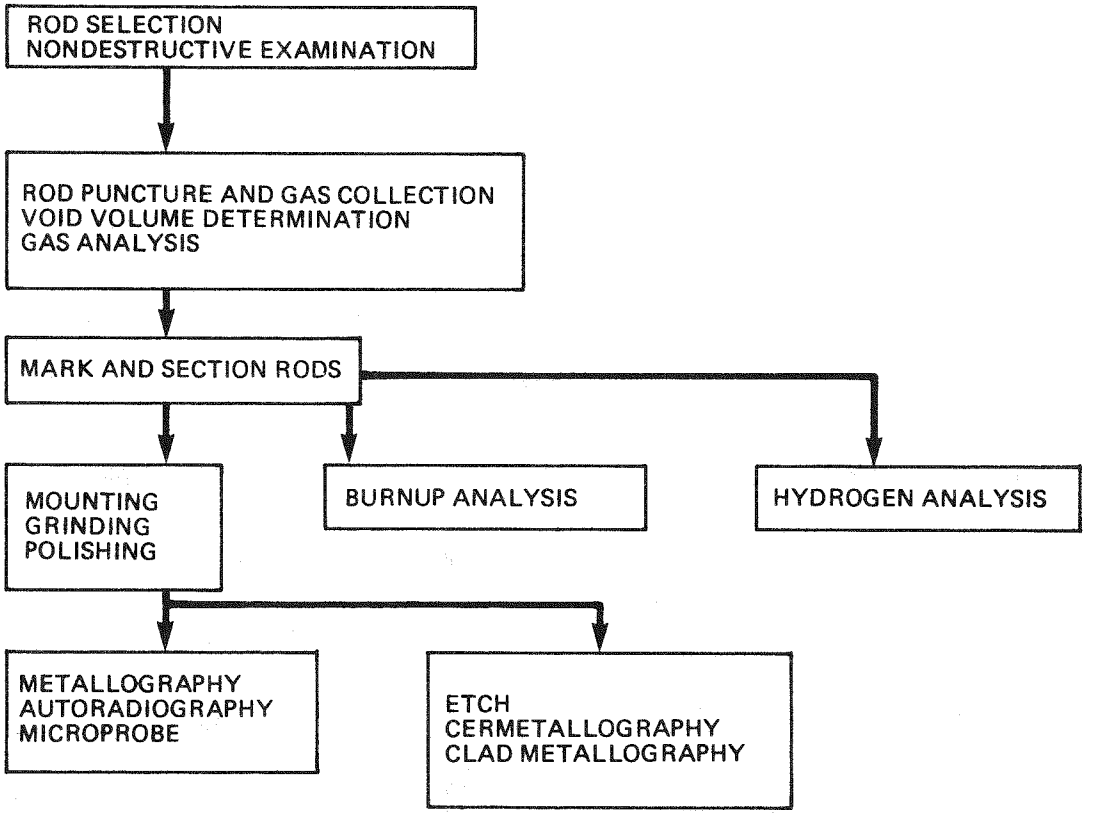

FIGURE 1. Process Flow Diagram for Destructive Characterization.

The first destructive examination was fuel rod puncture and gas collection. Analysis of the gas collected from this operation provided an indication of the fission gas released from the fuel. From the gas volume measured in this operation and the rod void volume measured in a subsequent operation, the prepuncture rod gas pressure was calculated. This allows calculation of the cladding stresses experienced during the demonstration disposal tests and laboratory rod tests.

Metallographic examination on fuel rod samples was conducted to characterize the cladding and features associated with fuel rod degradation. Characteristics such as cladding hydriding, cladding oxidation, fuel-cladding chemical interaction (FCCI), fuel pellet breakup, and fuel grain size were documented. These characteristics are important for defining spent fuel performance and the abilities of fuel and cladding to contain and retain radionuclides. Each characteristic has been defined in terms that will allow direct comparison with posttest characterization data. Autoradiography was performed on metallography samples to contribute to the qualitative understanding of radionuclide distribution and migration.

Chemical burnup analyses were performed on selected fuel rod sections to allow a burnup profile to be established using the gamma scan profile for correlation purposes. The burnup and actinide content analyses provide valuable information for calibrating and validating nuclear models.

Hydrogen analysis of selected cladding samples was performed to characterize the extent of zirconium hydride formation in the cladding. Changes in hydride concentrations and distribution during disposal demonstration tests may affect cladding degradation mechanisms and fission product containment.

The microprobe examination provided both qualitative and quantitative element identification as well as a distribution of the elements. Three regions were examined: fuel, gap, and cladding with major emphasis on the cladding and fuel-cladding gap. The examination determined the distribution of elements that are known to have the potential for altering the properties

of the cladding (e.g., cesium, iodine, tellurium, selenium, antimony, etc.) and measured the extent of their penetration into the cladding. Using this information, penetration modes and rates can be established for use in the spent fuel performance prediction model.

Stress rupture tests will be performed on selected cladding sections to characterize the creep strength and ductility of the cladding. Measurement of these properties will provide quantitative data relating to the ability of the fuel rod to retain radioactive species over an extended time period.

The rod position and length reference schemes that were used to facilitate the examination are shown in Figures 2 and 3. Fuel rod identification numbers were used to maintain traceability throughout the examinations. The zero degree radial orientation on the fuel rod was specified to be the radius perpendicular to assembly face A and was marked when the rods were removed from the assembly. Degrees were counted clockwise when viewed from the top. Fuel rod identification numbers were based on the grid position in the fuel assembly. The faces were lettered sequentially as shown in Figure 3. Rod axial measurements were referenced with respect to the bottom end plug.

A. FISSION GAS COLLECTION

The fuel rods were punctured, and internal gas was collected and analyzed. Pressure and volume measurements were made to determine the prepuncture pressure. This operation makes it possible to calculate cladding stresses during disposal testing of parent and similar fuel assemblies.

Table 3 shows the results of the gas volume, prepunch rod pressure, and rod void volume measurement. The mass spectrometric analysis of the gas for each rod is given in Table 4. The amount of fission gas release to the plenum region was at maximum 0.3% (see Appendix D). The internal gas volume was determined with a precision of 2% relative standard deviation and an accuracy of 3%. The isotopic analysis was accurate to 1% and a precision of ±2% relative standard deviation.

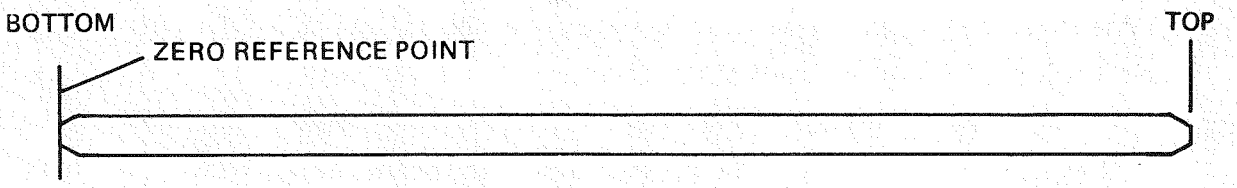

FIGURE 2. Turkey Point Fuel Rod Length Reference Scheme.

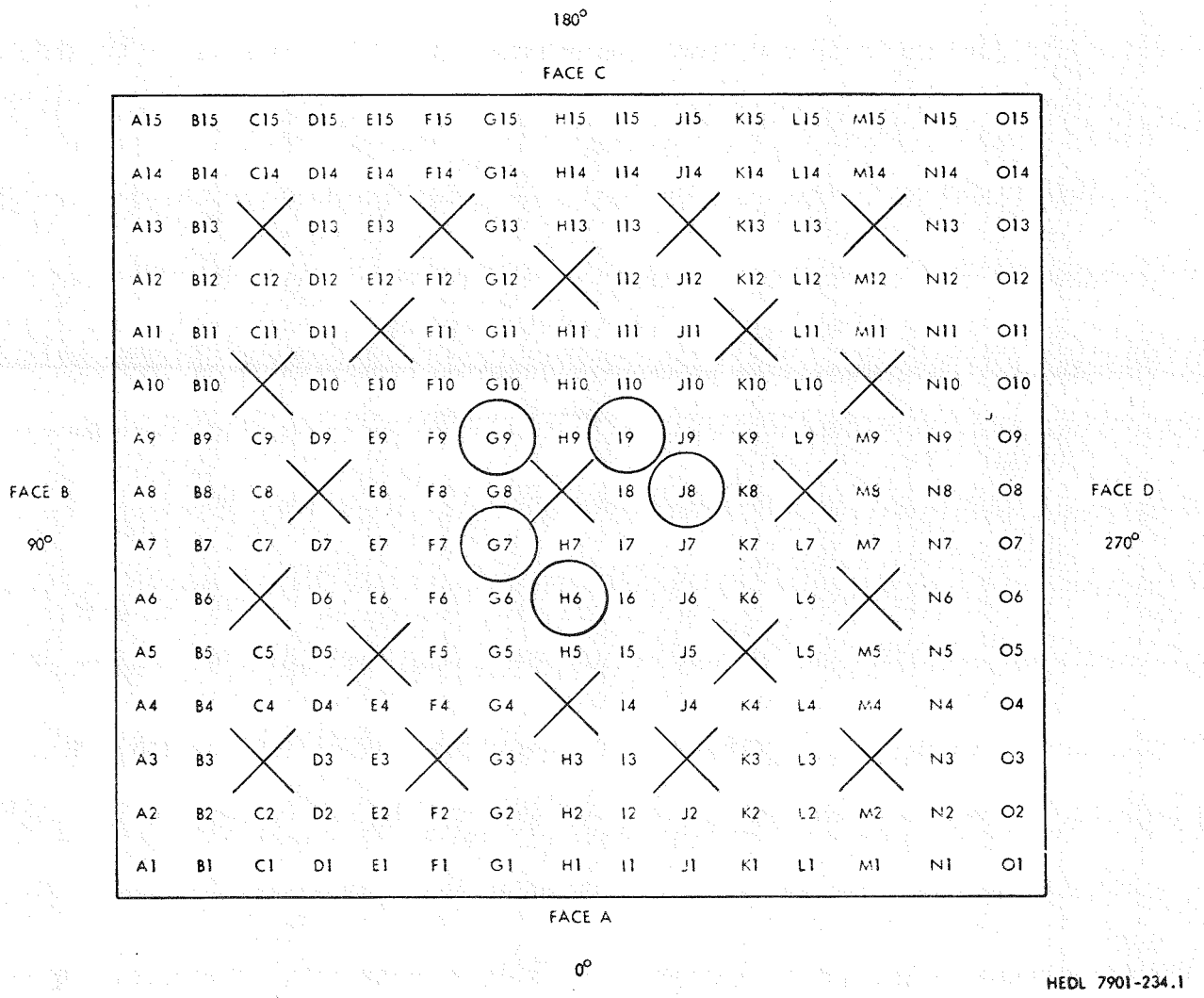

FIGURE 3. Turkey Point Fuel Assembly and Rod Position Scheme.

TABLE 3

VOID VOLUME AND INTERNAL PRESSURE
MEASUREMENTS FOR RODS G7, G9, I9, J8, AND H6

Rod Identification	Rod Void Volume (cc)	Rod Internal Pressure (psia)	Fuel Rod Temperature (°F)
G9	22.00	401.03	77
G7	23.71	360.90	78
I9	24.26	330.86	80
J8	22.12	385.19	77
H6	21.70	386.47	78

TABLE 4

INTERNAL ROD GAS ANALYSIS FOR RODS G7, G9, I9, J8, AND H6

	Percent Volume						1σ[(a)]
	Rod H6	Rod J8	Rod G7	Rod G9	Rod I9	Avg	Deviation
Temp (°C)	24.9	25.0	25.1	25.8	25.9	25.34	
H_2	<0.01	0.02	0.01	0.01	0.02	0.012	0.008
CH_4	<0.01	<0.01	<0.01	<0.01	<0.01	<0.01	--
H_2O	<0.01	<0.01	<0.01	<0.01	<0.01	<0.01	--
O_2	<0.01	<0.01	<0.01	0.02	<0.01	0.004	0.009
N_2	0.03	0.03	0.04	0.09	0.02	0.042	0.028
A	0.54	0.84	0.17	0.15	2.43	0.826	0.941
CO_2	<0.01	<0.01	<0.01	<0.01	<0.01	<0.01	--
Kr	0.071	0.061	0.064	0.118	0.086	0.080	0.023
Xe	0.615	0.540	0.586	0.979	0.738	0.692	0.177
Ratio Xe/Kr	8.66	8.85	9.16	8.30	8.58	8.71	0.32
He	98.744	98.509	99.12	98.633	96.706	98.342	0.943

(a)
$$\sigma = \sqrt{\frac{\Sigma X^2 - \frac{(\Sigma X)^2}{n}}{n - 1}}$$

The gas collection system consisted of a punch, collection chamber, two calibrated pressure gauges, roughing pump, expansion chambers, and toepler pump. Figure 4 is a schematic of the gas collection system.

Fuel rods were inserted through a gas-tight puncture chamber, and gas tightness was maintained by mechanical compressive fittings and Teflon seals around the rods at each end of the chamber. The entire system was evacuated to approximately five microns and checked for leak tightness. Before the rod was punctured, the chamber was pressurized with helium to 80 psi and allowed to expand into a known volume and the punch chamber volume determined.

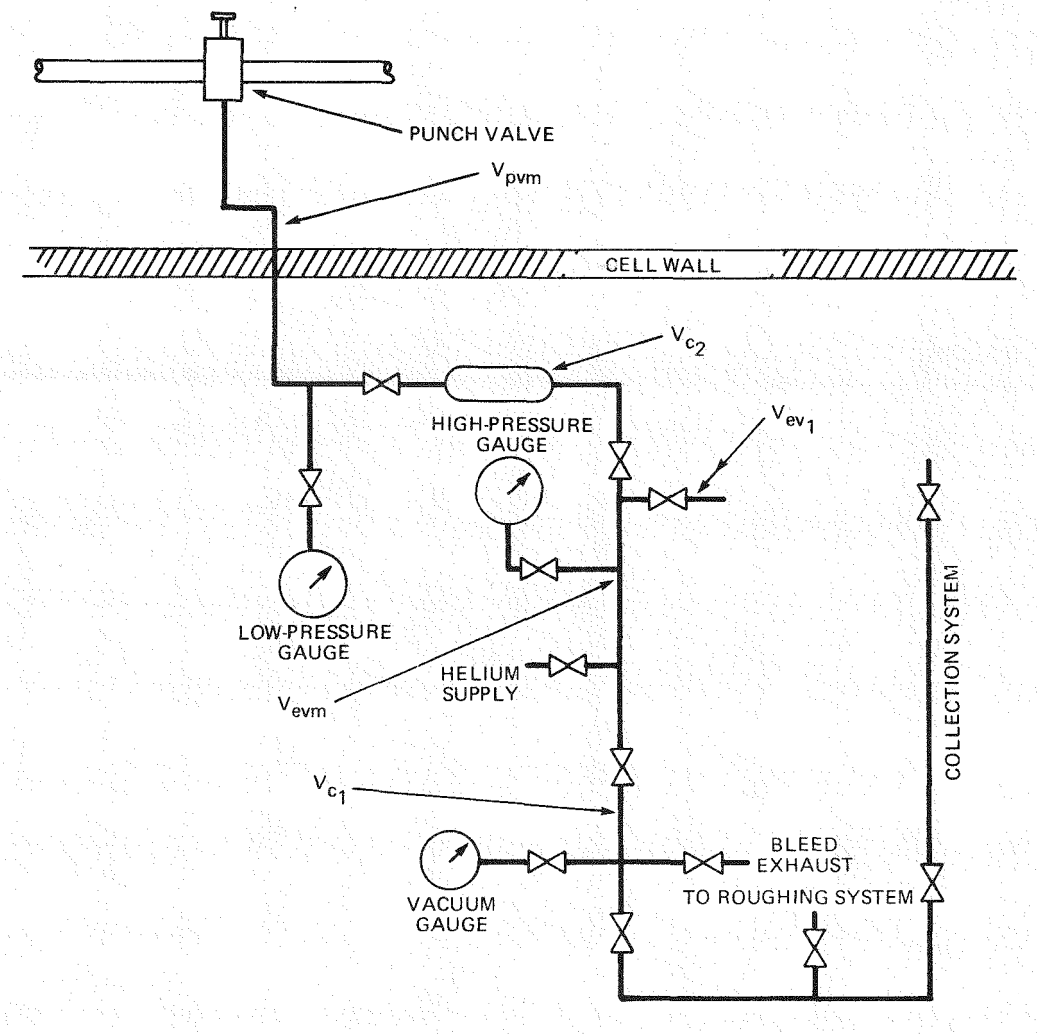

FIGURE 4. Gas Collection System Schematic.

This operation was repeated 10 times to determine the average volume. Next the system was evacuated and the rod punctured. Pressure readings and temperature of the punch chamber were recorded at the time of puncture and at two- and five-minute intervals thereafter until the system equalibrated. The gas was then expanded a second time into the known volume, and the amount of gas from the rod was calculated and recorded.

Gas was collected by allowing it to expand through the toepler pump into two containers until the system pressure was 1×10^{-3} torr. One of the containers was retained as a backup sample; the other was sent to the mass spectrometer laboratory for analysis.

B. FUEL ROD SAMPLING MATRIX

Fuel rod samples were removed from rods G9, G7, I9, J8, and H6 for metallographic examination, chemical analysis, and biaxial stress rupture testing. The fuel rod sample selection was based partially on nondestructive examination results and partially on previous experience with light water reactor (LWR) fuel. Observations from the nondestructive examinations (e.g., visual examinations, profilometry, gamma scan, and eddy current results) showed fuel rod condition to vary more along the axis than between the rods from an assembly or rods from all five assemblies characterized in the demonstration program. Consequently, the primary effort in the destructive examination was directed at obtaining a comprehensive characterization of fuel rod condition along the axis.

The condition of the fuel rod was examined at six locations along the length and at each end cap. The different sample types (e.g., metallography, hydrogen analysis, microprobe, and stress rupture) were clustered together at the six rod locations to aid development of interrelationships between the examination results (e.g., rod morphology and stress rupture behavior or hydrogen content). Variations in rod-to-rod conditions were determined by sampling from the same axial locations on all five rods but not to the same extent on each rod. A hierarchy was established for determining which

examinations should be conducted on which samples based on the type of information, the importance of that information, and the expected variations in the properties that the examination would yield. Table 5 summarizes the number and type of individual examinations conducted on the same sample (e.g., cladding thickness and oxide thickness). Rods G7 and G9 were the most extensively examined.

Figure 5 shows the rod cutting diagrams for all five rods. Rods H6, J8, and I9 were sectioned similarly but were not examined exactly the same.

TABLE 5

EXAMINATIONS PERFORMED ON EACH FUEL ROD

	Number of Examinations				
	Rod Identification				
Purpose	G7	G9	I9	H6	J8
Metallography					
Mosaic	6	6	5	3	1
Fuel Transverse	2	3	1	0	0
Cladding Thickness	6	6	2	3	1
Oxide Thickness	6	6	2	3	1
Cladding Hydrides	2	3	2	0	0
Autoradiography	3	1	1	1	1
Microprobe Examination	3	1	0	0	0
Longitudinal Mount	0	3	0	0	0
Chemical Analysis					
Burnup Analysis	4	1	1	1	1
Hydrogen Analysis	1	4	1	1	1
Biaxial Stress Rupture					
Fueled	4	3	4	4	4
Defueled	12	10	13	13	13

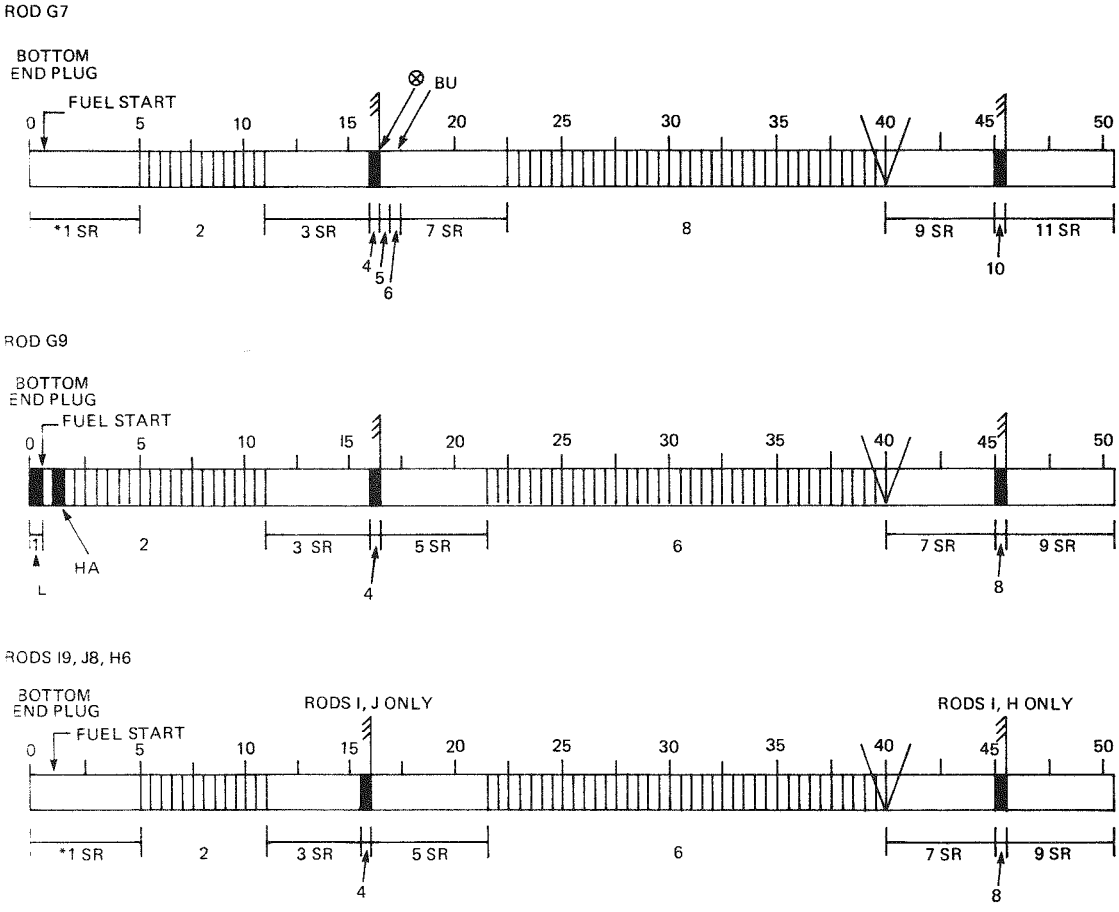

ROD CUTTING DIAGRAM
TURKEY POINT REACTOR ASSEMBLY B-17

SR - STRESS RUPTURE SAMPLE
* - FUEL STRESS RUPTURE SAMPLE
V - CUT POSITIONS FOR CELL TRANSFER
⊗ - ALPHA AND BETA-GAMMA AUTORADIOGRAPH
BU - BURNUP SAMPLE
HA - HYDROGEN ANALYSIS SAMPLE
L - LONGITUDINAL MOUNTED SAMPLE
▨ - MET SAMPLES POLISH LEFT SIDE
▮ - METALLURGICAL SAMPLE

FIGURE 5. Cutting Diagrams for Fuel Rods G9, G7, I9, J8, and H6.

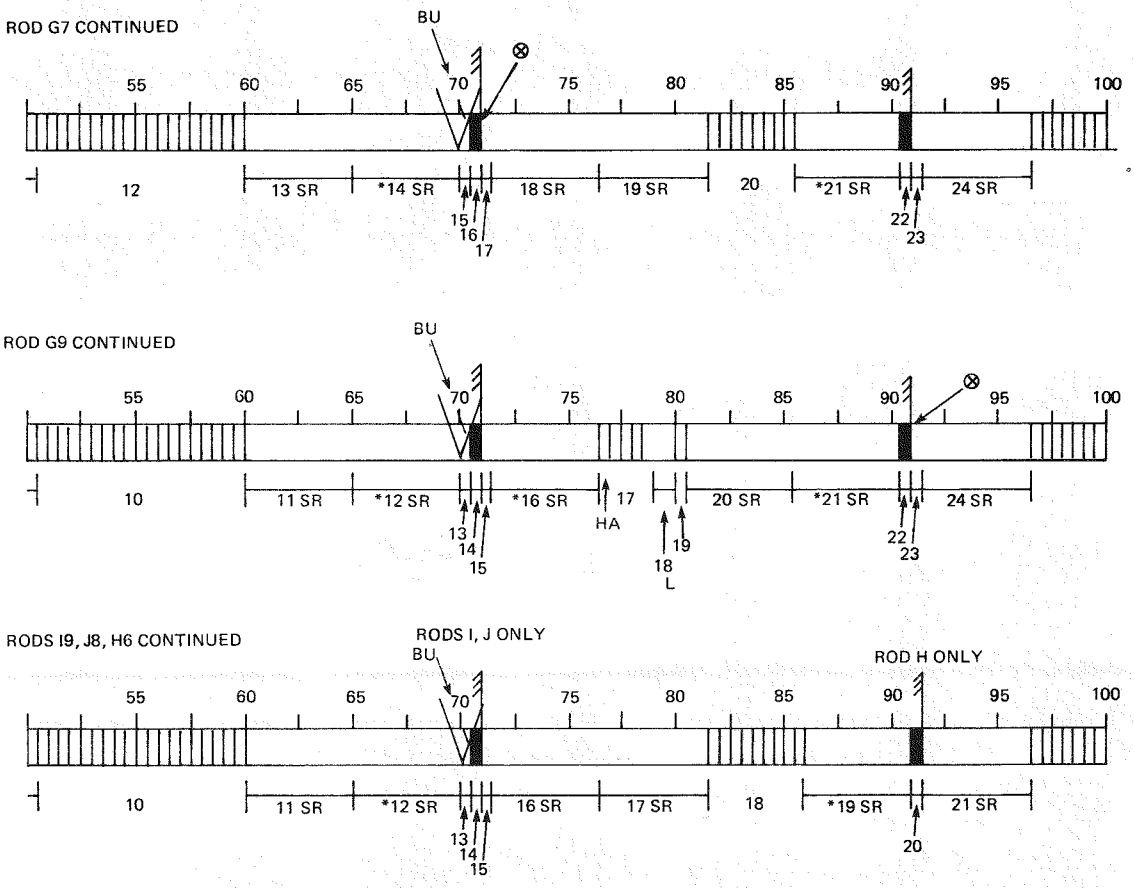

ROD CUTTING DIAGRAM
TURKEY POINT REACTOR ASSEMBLY B-17

SR - STRESS RUPTURE SAMPLE
* - FUEL STRESS RUPTURE SAMPLE
V - CUT POSITIONS FOR CELL TRANSFER
⊗ - ALPHA AND BETA-GAMMA AUTORADIOGRAPH
BU - BURNUP SAMPLE
HA - HYDROGEN ANALYSIS SAMPLE
L - LONGITUDINAL MOUNTED SAMPLE
▮ - MET SAMPLES POLISH LEFT SIDE
▮ - METALLURGICAL SAMPLE

FIGURE 5 (continued).

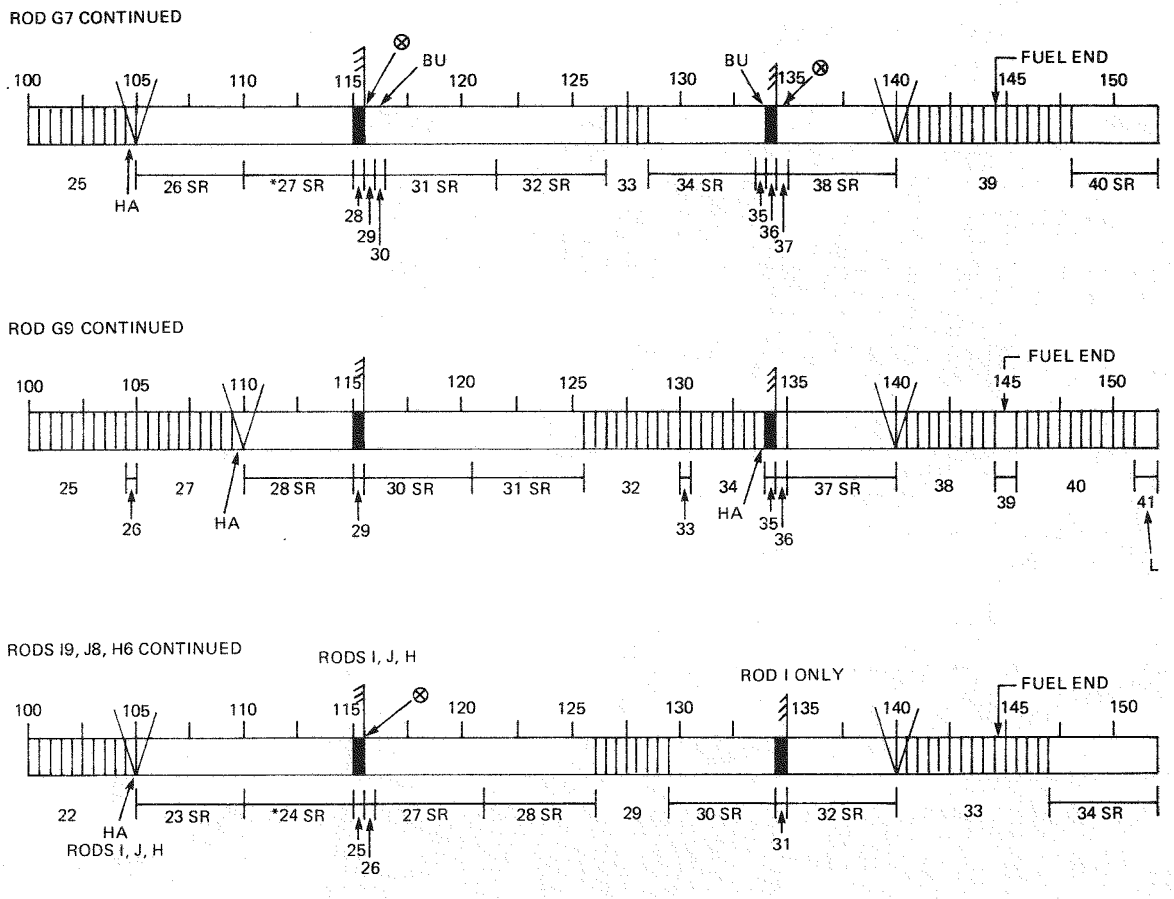

ROD CUTTING DIAGRAM
TURKEY POINT REACTOR ASSEMBLY B-17

SR - STRESS RUPTURE SAMPLE
* - FUEL STRESS RUPTURE SAMPLE
V - CUT POSITIONS FOR CELL TRANSFER
⊗ - ALPHA AND BETA-GAMMA AUTORADIOGRAPH
BU - BURNUP SAMPLE
HA - HYDROGEN ANALYSIS SAMPLE
L - LONGITUDINAL MOUNTED SAMPLE
▌ - MET SAMPLES POLISH LEFT SIDE
▌ - METALLURGICAL SAMPLE

FIGURE 5 (continued).

The cutting diagrams show that the half-inch samples were removed from nearly identical locations. The stress rupture specimens were taken next to the shorter samples. Fueled and defueled samples were selected on the basis of obtaining replicate sets both in axial location and from rod to rod.

Fuel rod samples were cut in 1/4-, 1/2-, 1-, and 5-inch lengths from the five fuel rods. Quarter-inch samples were used for cladding hydrogen content analysis. Half-inch samples were used for metallography (transverse mount), burnup analysis, autoradiography, and electron beam analysis. One-inch samples were mounted for metallography (longitudinal mount). Five-inch specimens were used for biaxial stress rupture testing.

C. ROD MARKING AND CUTTING OPERATION

The fuel rods were marked at cutting locations specified on the rod cutting diagram; the rods were then cut into four sections and transferred to a smaller hot cell for specimen cutting.

Marking was accomplished by placing the rod in a horizontal frame with a movable tubing cutter and burring punch mounted to the frame. The cutter wheel lightly contacted the rod at the position indicated by the measuring tape attached to the frame. The rod was rotated while contact with the cutter wheel was maintained, thereby scribing a circumferential mark on the rod. A light punch mark was made adjacent to the scribe mark to indicate the radial orientation and top of the cut section.

After transferring the marked rods, samples were cut with an abrasive disk rotating cutting wheel mounted on a portable pedestal and holding vice. The cuts were made using water as a lubricant and coolant to minimize distortions caused by cutting.

D. SAMPLE PREPARATION

Fuel rod sample preparation fell into three groups according to end use. Metallographic samples required mounting and polishing; stress rupture

samples needed defueling and cleaning; and no preparation was required for those samples that were to be analyzed chemically.

Samples for metallographic examination were mounted either transversely or longitudinally to the rod axis. Identical mounting procedures were followed for both types of specimens with the only difference being the size of the mount holder. They were first placed in stainless steel sleeves to prevent edge rounding during final polishing. The samples and sleeves were positioned in a 1-1/4 inch diameter Bakelite holder with a marker to designate the 0° orientation; mounting compound was poured over the sample to fill the cavity. The holder was held under a vacuum for several minutes to draw out the air trapped in the compound. Additional compound was added as needed, and the vacuum process was repeated until satisfactory impregnation was achieved. A 12-hour period was needed to cure the mounting compound.

Rough finishing was accomplished using an automet attachment on a low-speed grinding wheel. The samples were ground in batches of five in the automet holder. The specimens were ground sequentially on 120-, 240-, 400-, and 600-grit silicon carbide papers to approximately 0.050 inch from the cut surface. For longitudinally mounted samples, depth marking pins measuring 0.226, 0.216, and 0.206 inch were placed in the mounting compound and used as depth indicators during grinding and polishing operations.

Polishing was accomplished on a low-speed polishing wheel using texmet cloth with Linde-A and water slurry. On occasion, a finer polish was required on a vibratory polisher with micro-cloth and Linde-B water slurry.

Fuel and cladding etches were required for microstructural characterization and were performed by swabbing the sample surface with a cotton ball soaked in the proper etchant. Immediately after etching, the specimen was washed with water and then rinsed with alcohol and blown dry. The etchant used for examination of the fuel microstructure consisted of 85 parts H_2O_2 and 15 parts H_2SO_4. The cladding was etched with a freshly mixed solution of 48 volume percent (vol%) H_2O_2, 48 vol% HNO_3 and 4 vol% HF.

Both fueled and defueled specimens were prepared for biaxial stress rupture testing. The fuel in most sections was relatively loose and fell out of the cladding with a slight tapping motion. An aluminum plunger was used to knock out some of the pieces that did not fall out as easily.

Stringent contamination levels ($\leq$500 dpm/cm^2 alpha) were required for the defueled samples, which made additional chemical cleaning necessary. The cladding samples were soaked in a 50 vol% solution of nitric acid for five minutes and rinsed in tap water. The samples were then brushed using nylon bristles, resoaked in nitric acid, placed in a water bath, and cleaned ultrasonically. The samples were rinsed again with tap water, and smearable contamination levels were measured for compliance. Several samples required rebrushing and soaking to reduce contamination to the required level.

Fueled samples were partially defueled on each end; the aluminum plunger was inserted in one end, and the fuel was gently pushed out the other. About 1 1/2 inches of fuel was pushed out of the end and broken off. The plunger was removed and placed in the other end, and the fuel was centered in the sample so that there was approximately 0.75 inch of fuel removed from each end. All stress rupture samples were subsequently placed in aluminum vials and shipped to HEDL for testing.

E. METALLOGRAPHIC EXAMINATION

The metallographic examination provided a qualitative documentation of the fuel rod microstructure. Photomicrographs were taken of the fuel and cladding microstructure at selected areas of interest.

1. General Microstructure

Photographs of sample surfaces were taken to provide documentation of cracks, porosity, degree of pellet cracking, reaction products, and hydrides. Mosaics (35X) were made of all samples in the mounted and as-polished condition before further metallographic examination. These mosaics are shown in Appendix A.

Based on published literature[3] the general appearance and features shown in the mosaics were typical of that expected from fuel rods with the same operating history. There was no evidence of fuel pellet restructuring. Table 6 indicates the relationship between the amount of pellet cracking and the axial position of the sample. Nearly all fractures were oriented radially, most with the wide crack openings at the center of the pellet (see Appendix A). The remainder of the radially oriented cracks showed the wider crack width on the outer surface of the fuel. Some evidence of crack healing was seen on samples taken from the axial center of the rod. Circumferential cracks were seen in a few samples taken from the middle. Fuel pellet fragmentation was seen in only a few samples. Fuel particles were shown in the gap where fragmentation of the pellet outer surface occurred.

Qualitative determination of the void fraction was hampered by fuel fallout that occurred during the polishing operation. Bright, shiny, metallic particles (fission product agglomerates or impurities) were seen in some of the voids.

TABLE 6

NUMBER OF PELLET PIECES FOUND IN
SAMPLES TAKEN FROM RODS G7, G9, I9, J8, AND H6

Axial Location (in.)[a]	Number of Pieces					
	Rod G7	Rod G9	Rod I9	Rod H6	Rod J8	Average
16.5	12	17	17	--[b]	--	15.3
45.5	14	11	11	17	--	13.2
71.0	14	19	22	--	--	18.0
91.0	11	17	--	12	--	13.3
115.5	13	10	17	14	11	13.0
135.0	8	7	8	--	--	7.6

[a] From bottom of fuel rod.

[b] Metallurgical specimens not prepared at these locations (--).

A distinct gap between the fuel and cladding could be seen circumferentially around the pellet outer surface on all the samples. The gaps ranged from 0.001 to 0.010 inch, with the smallest gaps observed in samples taken from the middle of the rod. Several samples from mid-rod regions showed pellet-cladding contact at one or two places on the circumference. Evidence of localized fuel-cladding bonding was seen at areas of pellet-cladding contact.

The cladding in all samples appeared uniform and of good integrity. As expected, some hydride precipitation was evident; hydride concentrations are discussed more thoroughly in the Metallurgical Examination and Hydrogen Analysis sections.

2. Fuel Microstructural Analysis

Seven samples* were selected for detailed documentation and analysis of the fuel microstructure. The samples were fuel-etched and photomicrographed at 100X and 500X. The 100X photomicrographs were taken along a radius from the outer fuel surface to the central axis and were pieced together to form a mosaic of the fuel radius. The 500X photomicrographs were taken every 500 to 1,000 microns along the same radius to provide a more detailed view of the microstructure.

Two radial mosaics of the fuel surface are shown for samples I9-14 (71.0 in.) and I9-31 (134.5 in.) in Figure 6. The polyhedral grains appeared equiaxed and varied in size along the radius. Grain boundary counting was conducted using the linear intercept method (ASTM E-112-77, Section 10). Grain boundary intercepts were counted on a 50-mm line drawn on a 100X photomicrograph oriented perpendicular to the pellet radius. Grain boundary intercepts were counted every 500 microns along the radius, beginning adjacent to the fuel outer surface.

*G9-4 (16.5 in.), G7-10 (45.5 in.), I9-14 (71.0 in.), G9-14 (71.0 in.), G7-22 (91.0 in.), G9-29 (115.0 in.), and I9-31 (134.5 in.).

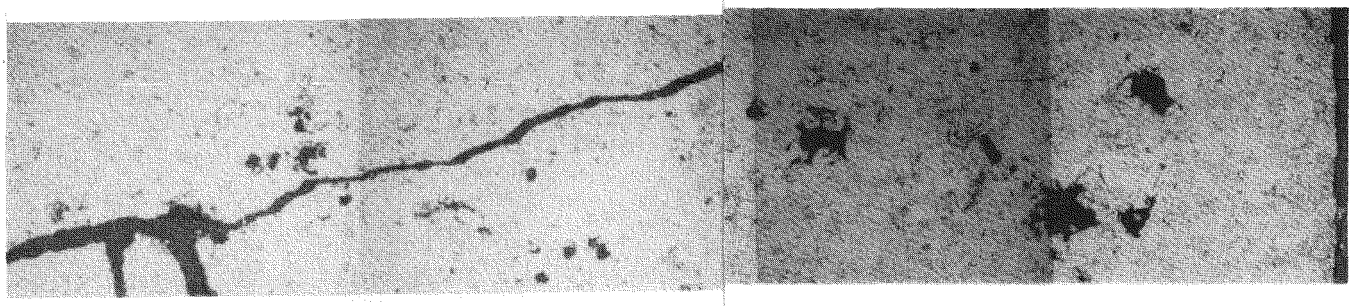

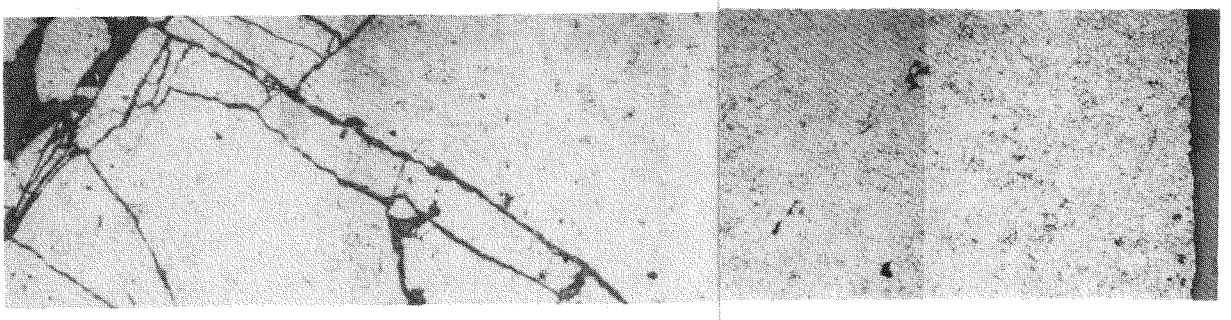

6. Radial Mosaics of Etched Fuel Samples I9-31 (134.5 in.) and I9-14 (71.0 in.). (Fuel center is at left. Right edge is adjacent to cladding. Neg 7907678-4

Counting was conducted on each radial mosaic; the results are presented in Table 7. Due to the lack of an accepted shape factor for the uranium dioxide grains, data are presented as the number of grain boundary intercepts at 100X magnification. The data indicate smaller grains on the fuel outer surface than at the central axis.

TABLE 7

NUMBER OF GRAIN BOUNDARY INTERCEPTS
PER MILLIMETER AT 100X FOR RODS G7, G9, AND I9

Rod Identification	Distance From Rod Bottom (in.)	Fuel Outer Surface	Distance From Outer Surface (microns)								Fuel Central Axis
			500	1000	1500	2000	2500	3000	3500	4000	
G9	16.5	0.41	0.27	0.23	0.20	0.25	0.24	0.29	0.27	0.30	0.32
G7	45.5	0.67	0.55	0.46	0.51	0.52	0.49	0.42	0.47	0.47	0.51
G9	71.0	0.60	0.5	0.54	0.55	0.55	0.48	0.51	0.54	0.56	0.44
I9	71.0	0.70	0.63	0.44	0.63	0.57	0.55	0.52	0.50	0.50	0.62
G7	91.0	0.61	0.66	0.56	0.66	0.52	0.56	0.53	0.53	0.48	0.57
G9	115.5	0.37	0.35	0.37	0.23	0.27	0.27	0.27	0.26	0.29	0.28
I9	135.0	0.68	0.61	0.51	0.51	0.57	0.54	0.54	0.56	0.53	0.58

Photomicrographs of the fuel taken at 500X provided a more detailed view of the grain structure and porosity. Figures 7, 8, and 9 indicate the change across the radius for the two samples (I9-14 and I9-31). The photomicrographs were taken at the center, mid-radius, and outer surface. The porosity shown is both intergranular and intragranular at the fuel outer surface and almost exclusively intergranular in the center of the pellet. The porosity at the mid-radius is shown both at the grain boundaries and in the grains. Photomicrographs of the sample taken from the axial middle of the rod exhibits a much finer pore structure at the grain boundaries than the sample taken from the top of the rod. The larger pores were seen to be located at the intersections of three or more grains.

Photomicrographs at 500X of inclusions or impurities found in the fuel are shown in Figure 10.

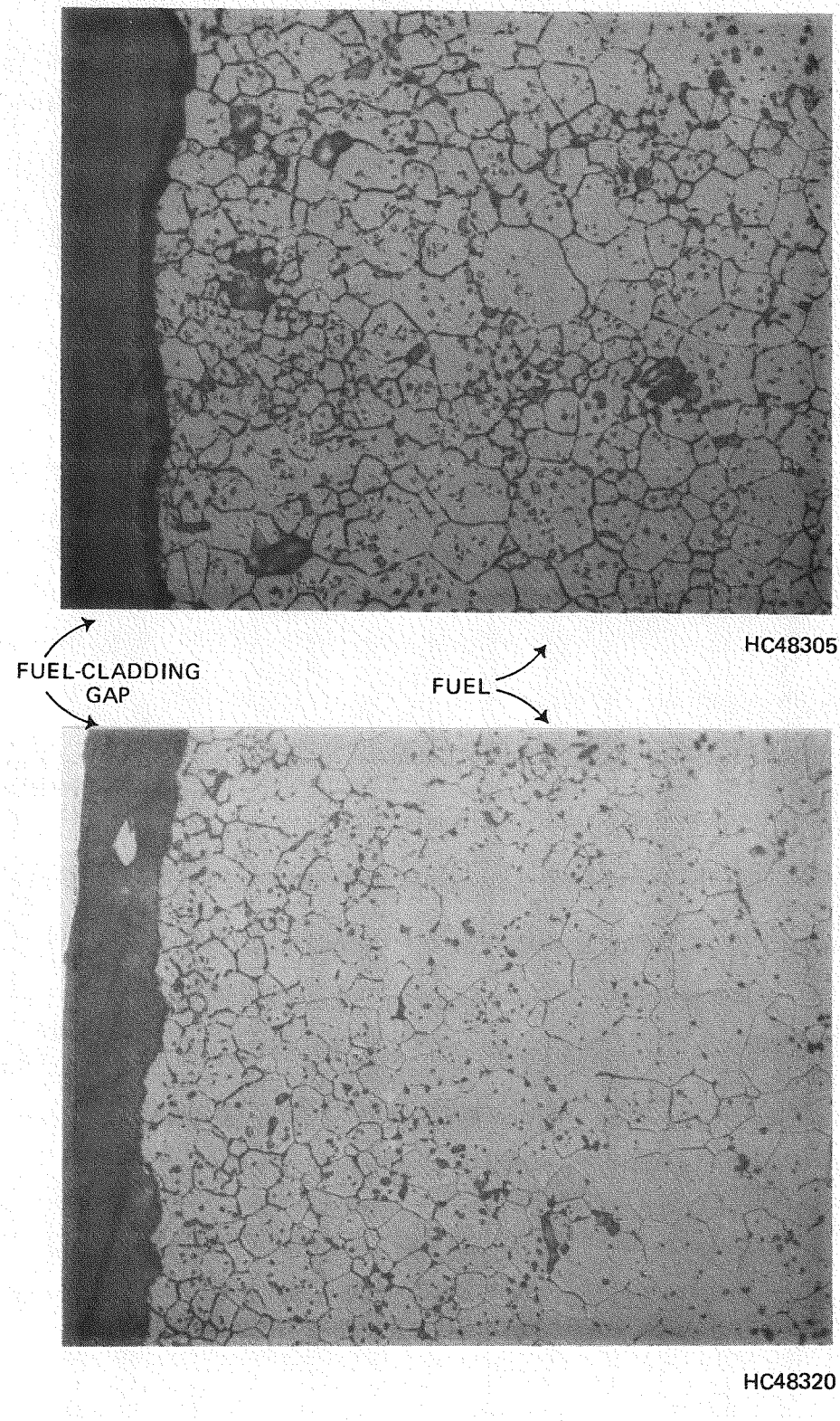

FIGURE 7. Photomicrographs of Fuel Microstructure at Fuel Outer Surface of Samples I9-14 (71.0 in.) and I9-31 (134.5 in.) at 500X.

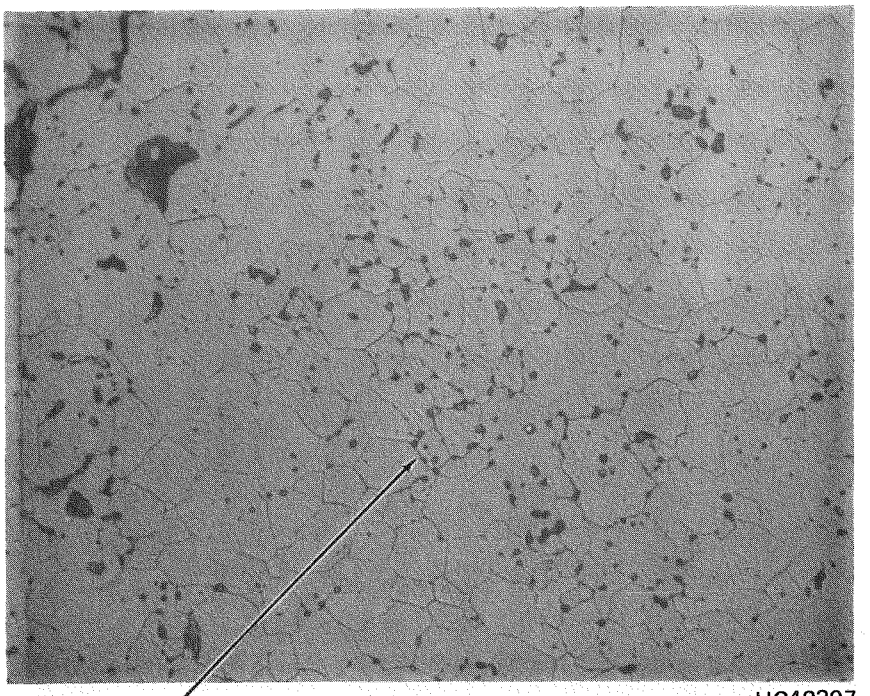

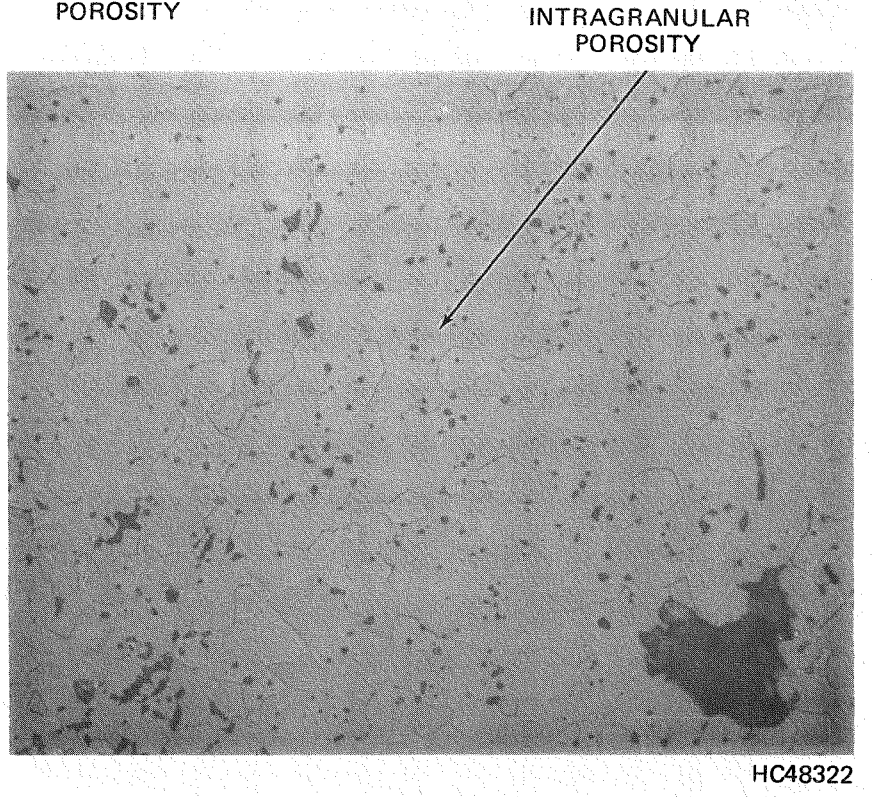

FIGURE 8. Photomicrographs of Fuel Microstructure at Mid-Radius of Samples I9-14 (71.0 in.) and I9-31 (134.5 in.) at 500X.

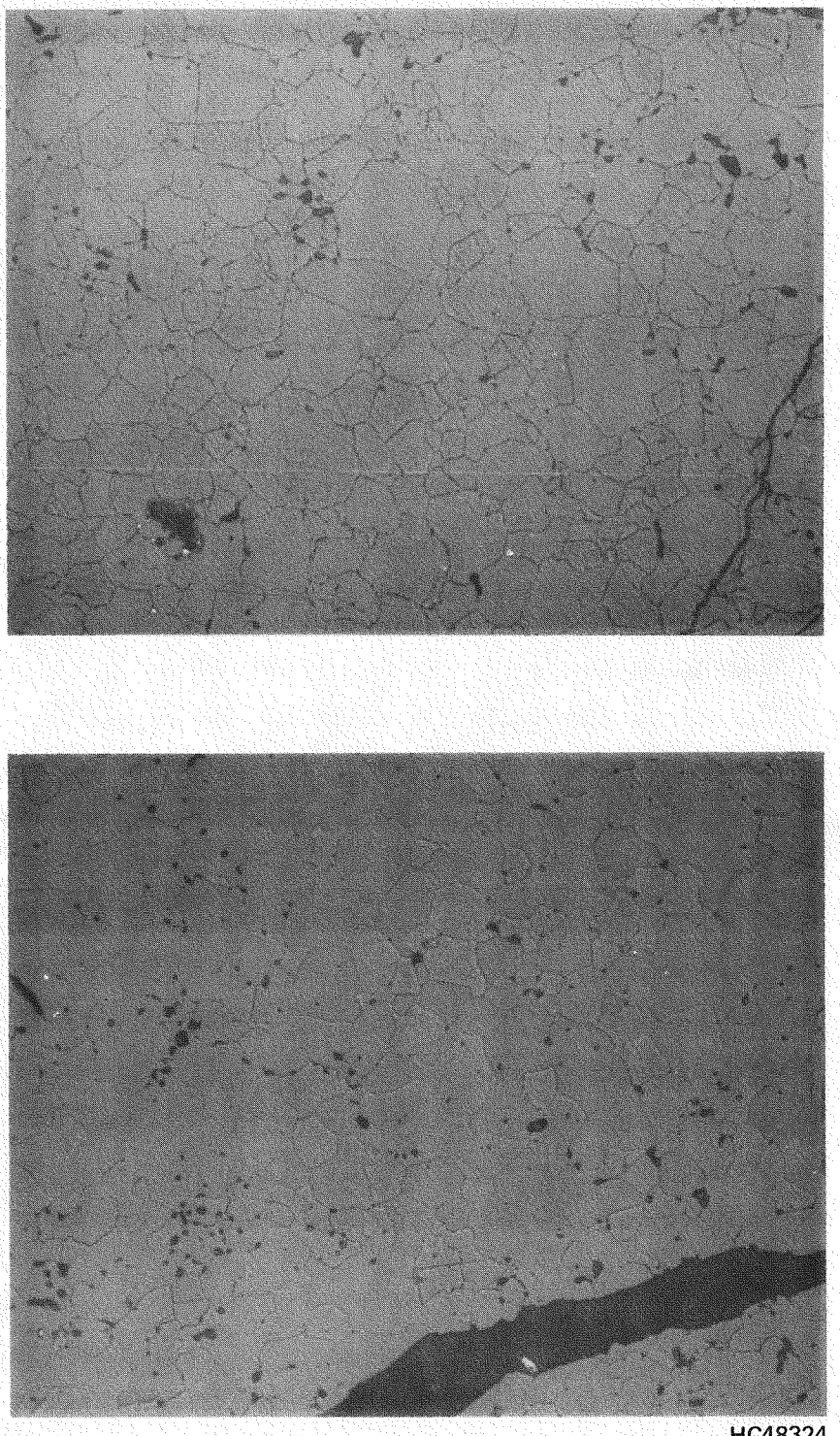

FIGURE 9. Photomicrographs of Fuel Microstructure at Central Axis of Samples I9-14 (71.0 in.) and I9-31 (134.5 in.) at 500X.

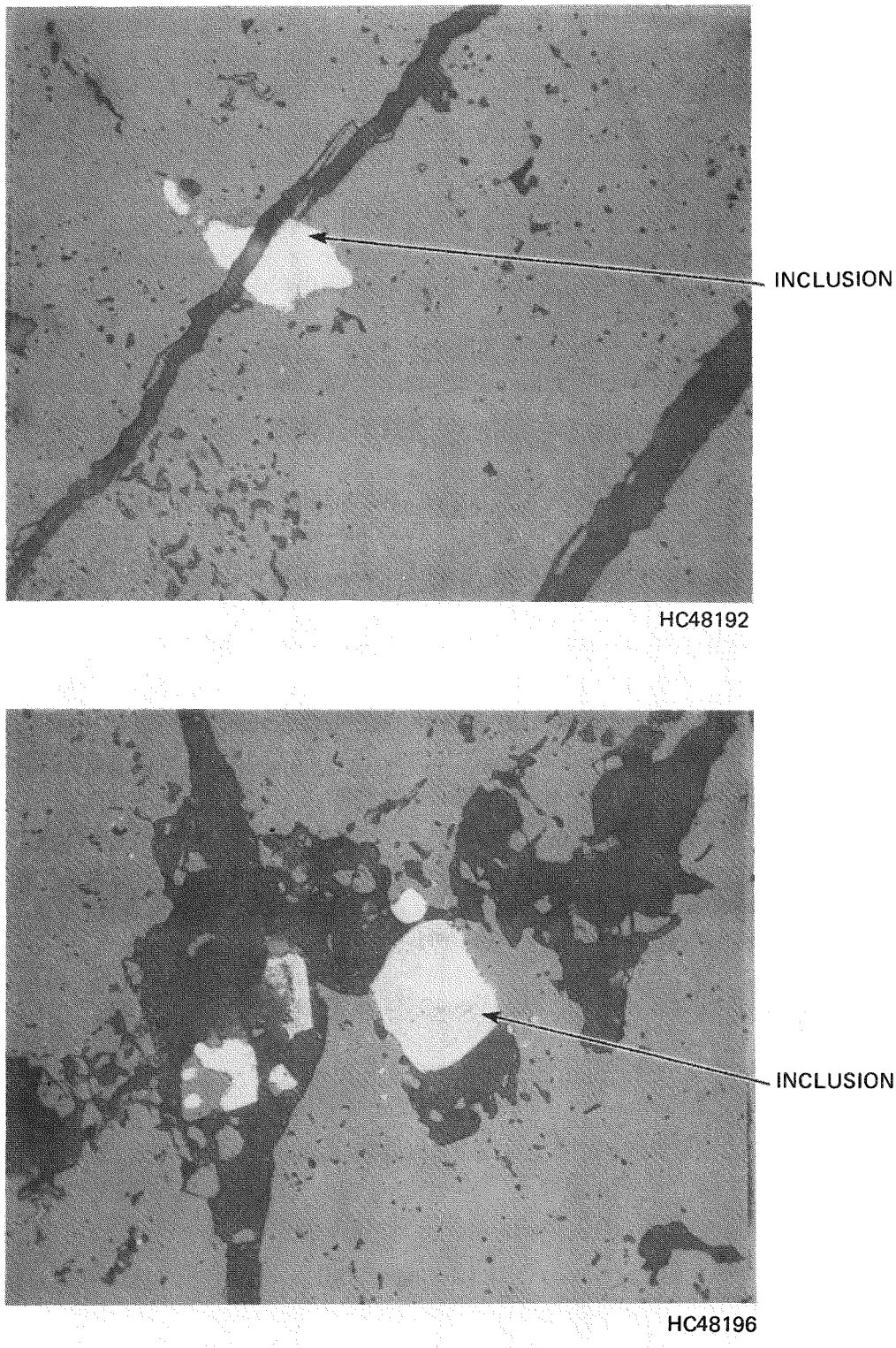

FIGURE 10. Photomicrographs of Fuel Inclusion on Samples I9-31 (134.5 in.) and H6-8 (45.5 in.) at 500X.

3. Cladding Microstructural Analysis

Eighteen metallographic samples were selected for cladding and oxide thickness measurements at 16.5, 45.5, 71.0, 91.0, 115.5, and 134.5 inches from the rod bottom. Each sample was examined and photomicrographed in the as-polished condition at 0°, 90°, 180°, and 270° radial orientations. Photomicrographs were taken of the cladding and the oxide at magnifications of 100X and 500X, respectively. The oxide layer that existed on the outer surface of the fuel rods was not chemically analyzed; however, from previous experience[3] these layers can be expected to contain a combination of zirconium oxide and deposits from the reactor coolant (crud).

The photomicrographs were used for measuring cladding thickness and oxide thickness. Plots of the oxide thickness and cladding width versus the radial orientation for all 18 samples are presented in Appendices B and C. Rod-to-rod variations for both oxide and cladding thickness were negligibly small as compared to the axial change. Both oxide and cladding thickness layers were circumferentially uniform below 70 inches, at which a greater radial change in the oxide layer and to a lesser degree the cladding thickness was shown.

The oxide layers showed good adherence to the cladding. Analysis of the data indicates oxide thickness layers increased and became less uniform and more porous as the samples increased in distance from the bottom of the rod. The greatest variation was observed in samples taken at 90 and 115 inches from the rod bottom. Figure 11 shows the varying oxide thickness on samples I9-25 (115.5 in.) and G7-22 (91.0 in.). A transition from a dense oxide layer to a porous oxide layer was found. Figure 12 illustrates the oxide layer change along the length of rod G7, which coincides with the transition noticed in the visual examination at approximately 90 inches; the transition that occurs is illustrated by these photomicrographs taken at five locations on rod G7.

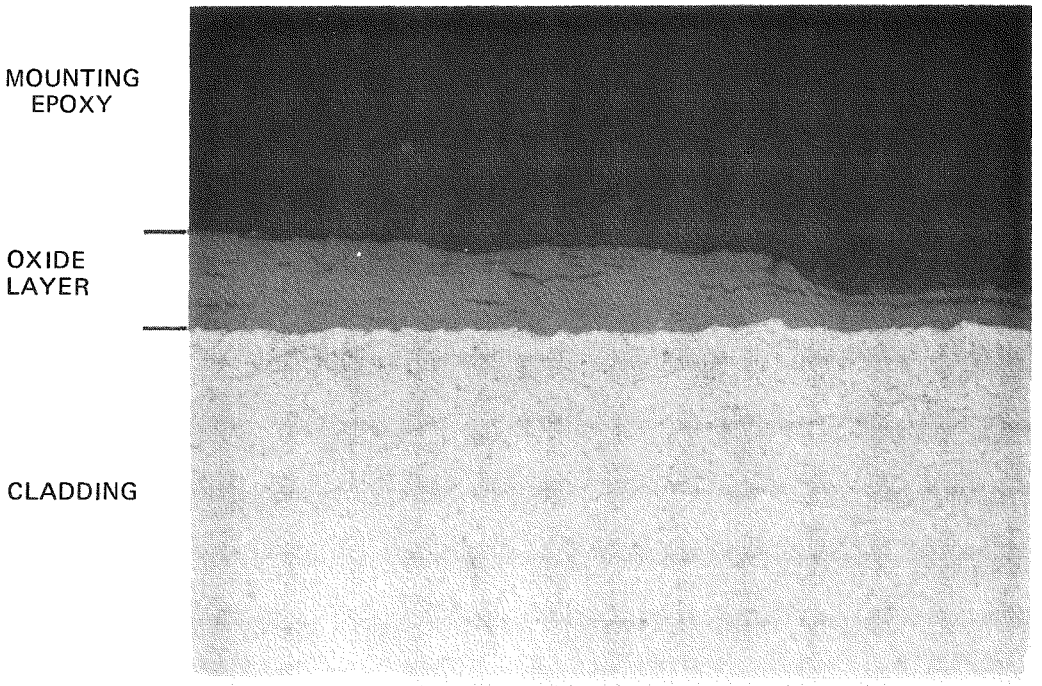

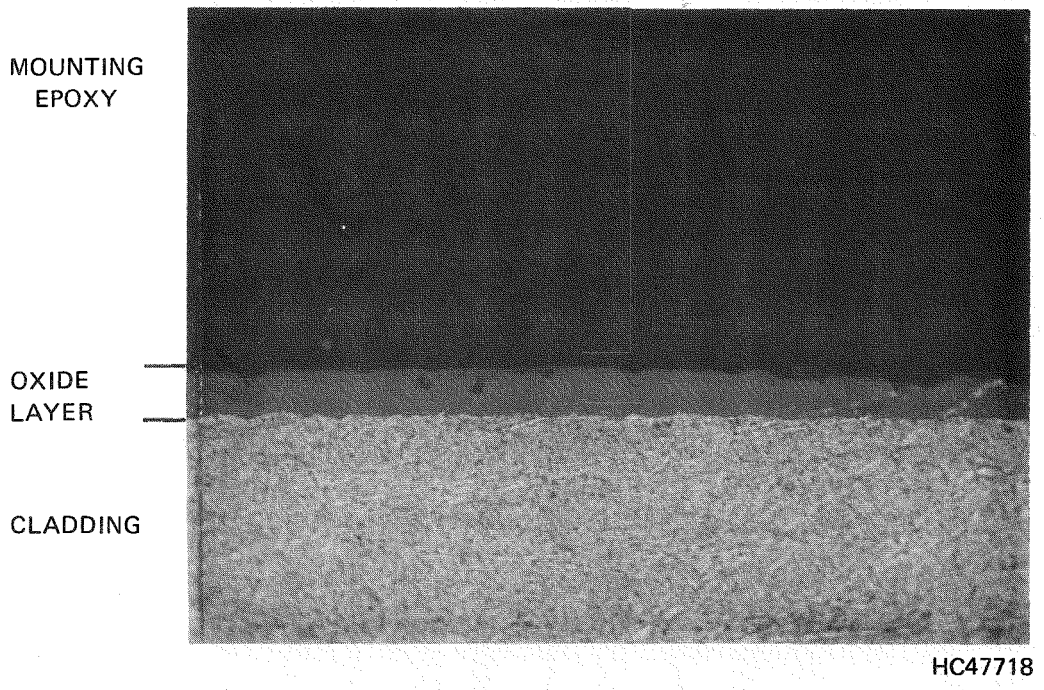

FIGURE 11. Phtomicrographs of Oxide Layer on Cladding Outer Surface of Samples I9-25 (115.5 in.) and G7-22 (91.0 in.) at 500X.

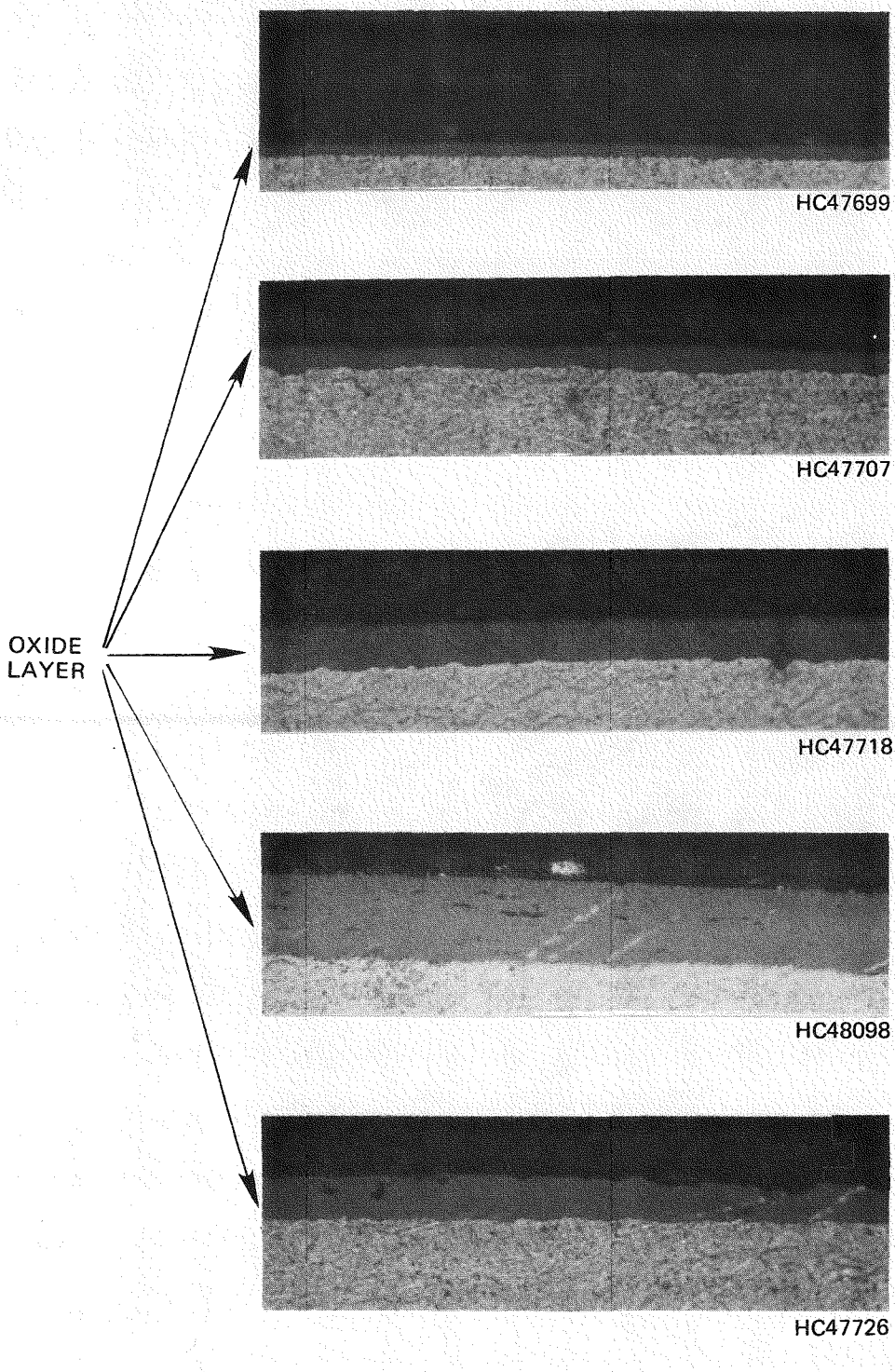

FIGURE 12. Photomicrographs of Cladding Oxide Layer Change Along Rod G7; Samples Taken from 45.5, 71.0, 91.0, 115.5, and 134.5 Inches from the Bottom of the Rod at 500X.

An interesting area on rod H6 was found where the oxide layer was in the process of being spalled off, as shown in Figure 13. Note the thickness of the layer and the absence of voids and pores.

Analysis of cladding widths showed variations from 0.0233 to 0.0250 inch, with larger cladding widths measured at the bottom of the rods. Figures 14, 15, and 16 plot the average cladding width and oxide thickness measured at four circumferential orientations at various axial locations for rods G7, G9 and H6. Oxide thickness and cladding width are inversely related. The ratio of cladding-to-oxide thickness exhibits similar patterns for all rods, as shown in Figure 17.

Seven samples* were selected for detailed documentation of the cladding microstructure and the zirconium hydride concentration and distribution. The samples were clad-etched and photomicrographed at 0°, 90°, 180°, and 270°.

The cladding microstructure was typical of a cold-worked material; it exhibited a fine grain size and the texture was perpendicular to the plane of the photomicrograph (on a transversely mounted sample). No gross abnormalities were seen.

The hydrides appeared as long stringers or squiggly lines in the photomicrographs. Figure 18 illustrates extreme examples of hydride formation at 115.5 and 134.5 inches from the bottom of rod G9-29. The majority of the hydrides were oriented circumferentially in the cladding. There was a noted lack of hydrides oriented radially in most photomicrographs. Hydride distribution was concentrated towards the inner radius of the cladding on samples taken from the lower end of the rod, and the distribution was uniform for those samples taken from the middle or top region of the rods. The greatest concentration of hydrides was found in samples taken from 115 inches from rod bottom. The majority of the hydrides ranged

*G9-4 (16.5 in.), G7-10 (45.0 in.), I9-14 (71.0 in.), G9-14 (71.0 in.), G9-22 (91.0 in.), G9-20 (115.5 in.), and I9-31 (134.5 in.).

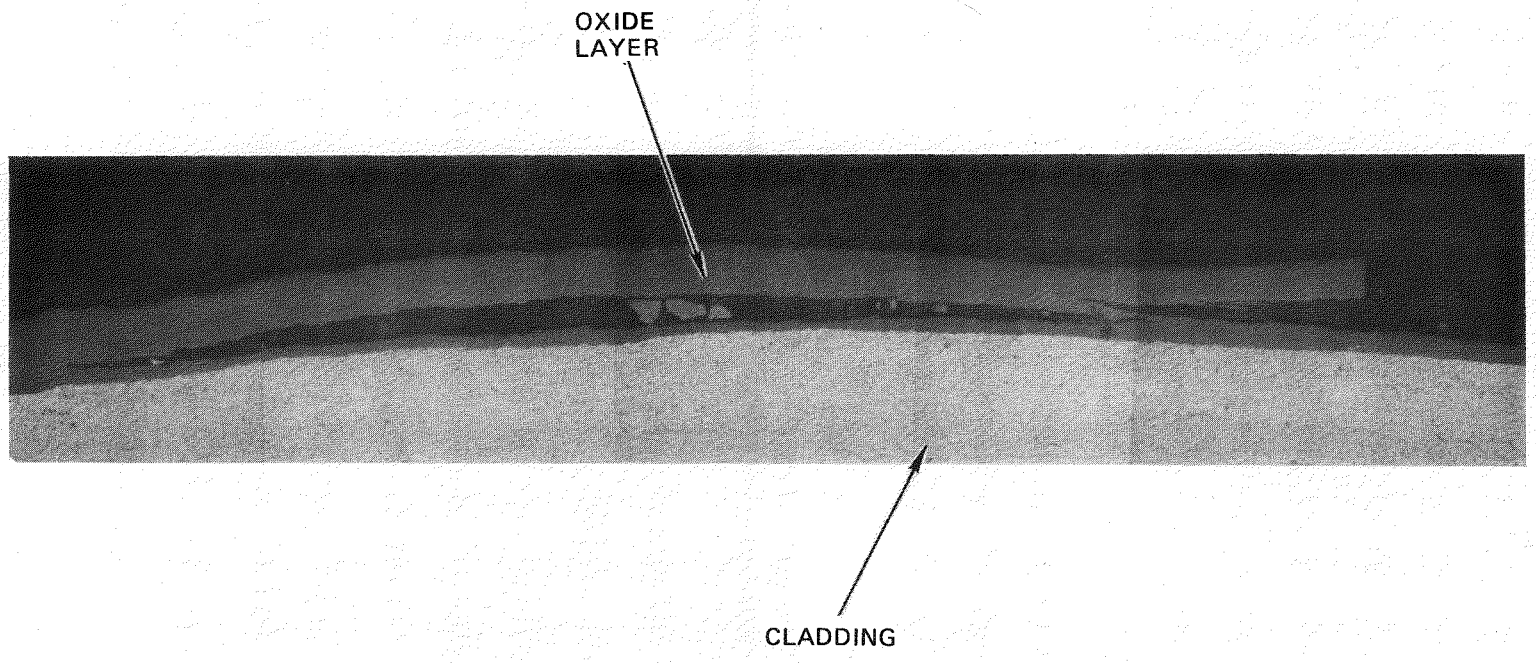

FIGURE 13. Photomicrograph of Cladding Oxide Layer on Outer Surface of Sample H6-25 (115.5 in.) Reduced to 250X.

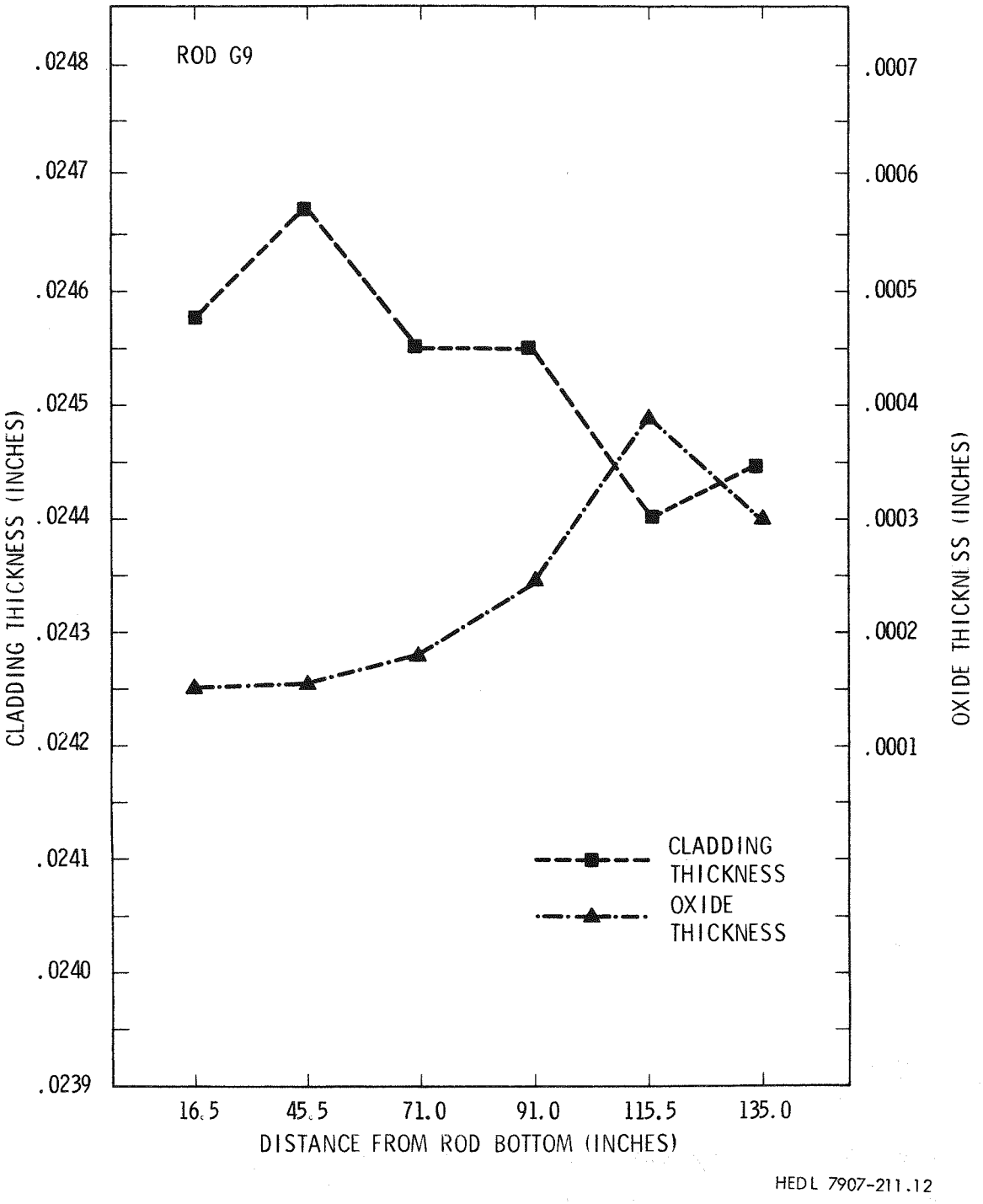

FIGURE 14. Plots of the Oxide Thickness and Cladding Width Measurements at 16.5, 45.5, 71.0, 91.0, 115.5, and 134.5 Inches from the Bottom of Rod G9.

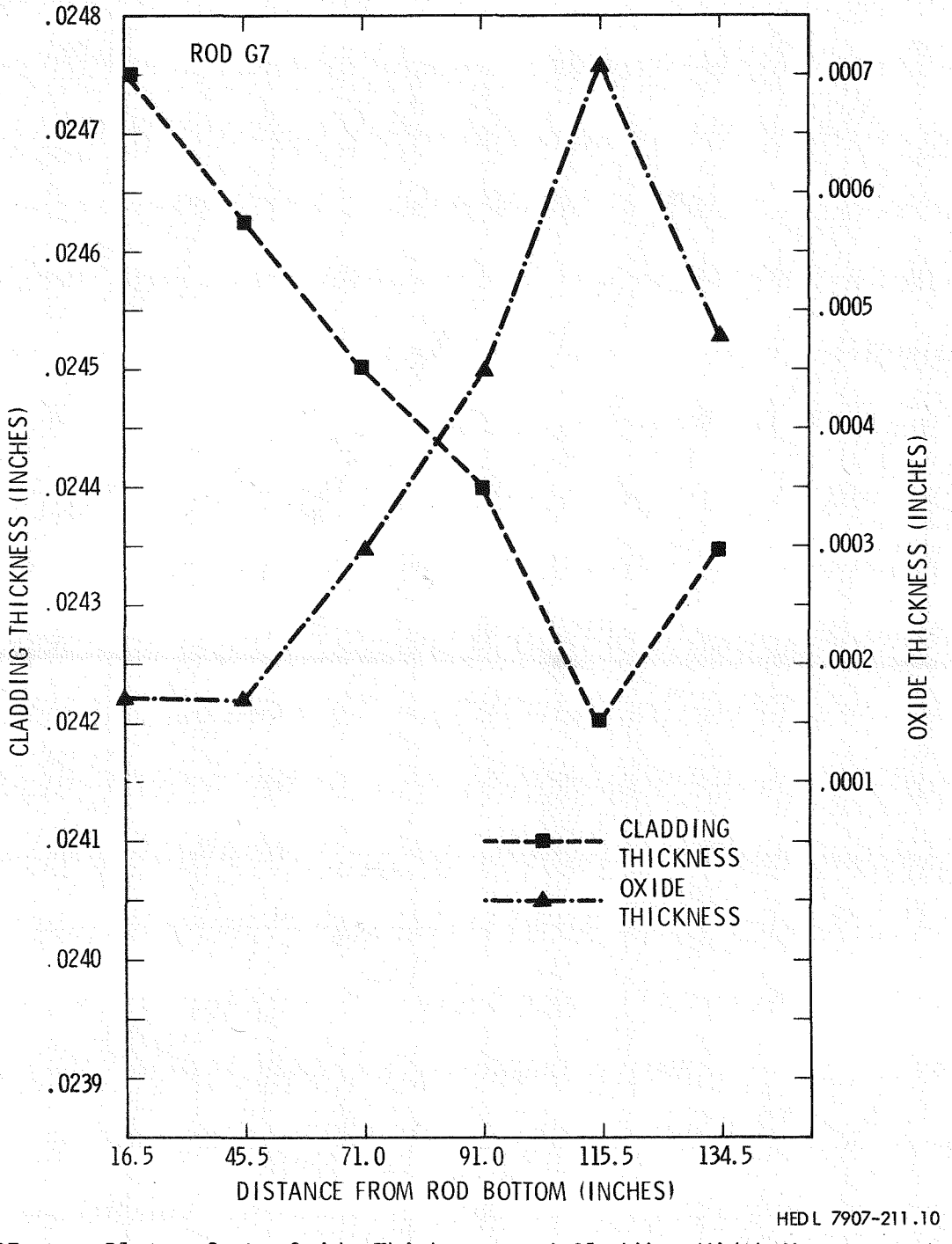

FIGURE 15. Plots of the Oxide Thickness and Cladding Width Measurements at 16.5, 45.5, 71.0, 91.0, 115.5, and 134.5 Inches from the Bottom of Rod G7.

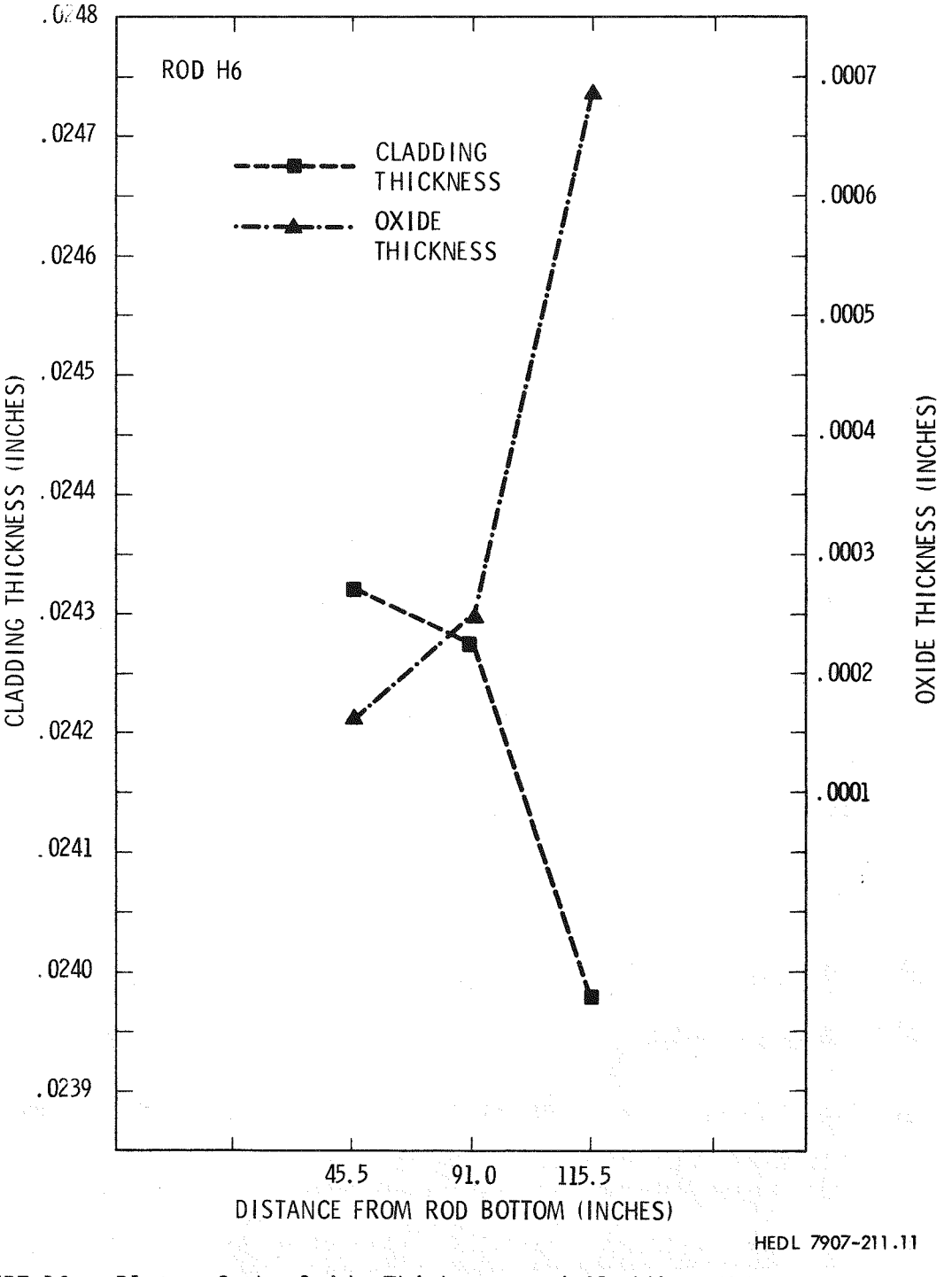

FIGURE 16. Plots of the Oxide Thickness and Cladding Width Measurements at 45.5, 91.0, and 115.5 Inches from the Bottom of Rod H6.

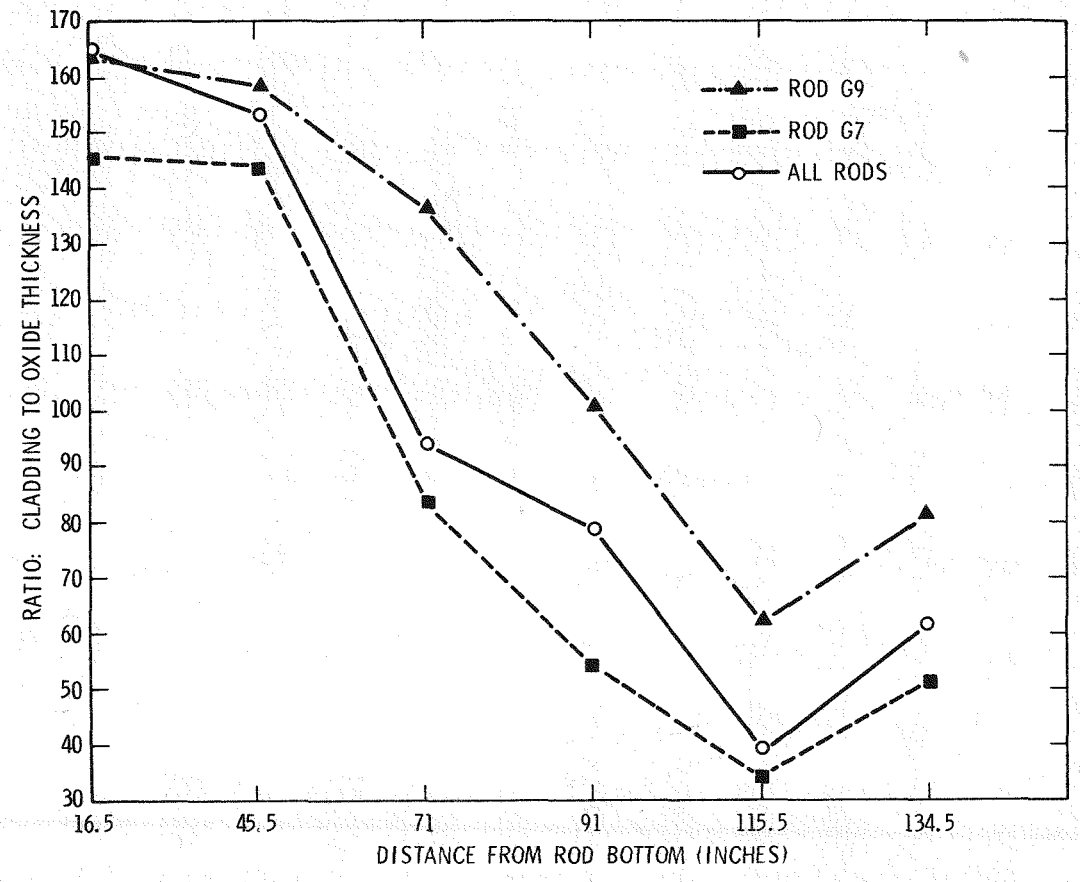

FIGURE 17. Plots of Cladding Width to Oxide Thickness Ratios for Rods G9 and G7 and the Average for All Rods at 16.5, 45.5, 71.0, 91.0, 115.5, and 134.5 Inches from the Bottom of the Fuel Rod.

from 0.001 to 0.020 inch in length. However, several hydrides were much longer (covering 0.10 inch).

Figures 19, 20, and 21 show the axial variation of the hydride concentrations at six locations on rods G9, G7, and I9. Note the evidence of some radially oriented hydrides connecting the circumferentially oriented stringers on the cladding inner surface. Quantitative values of hydride concentration are further discussed in the Hydrogen Analysis Section.

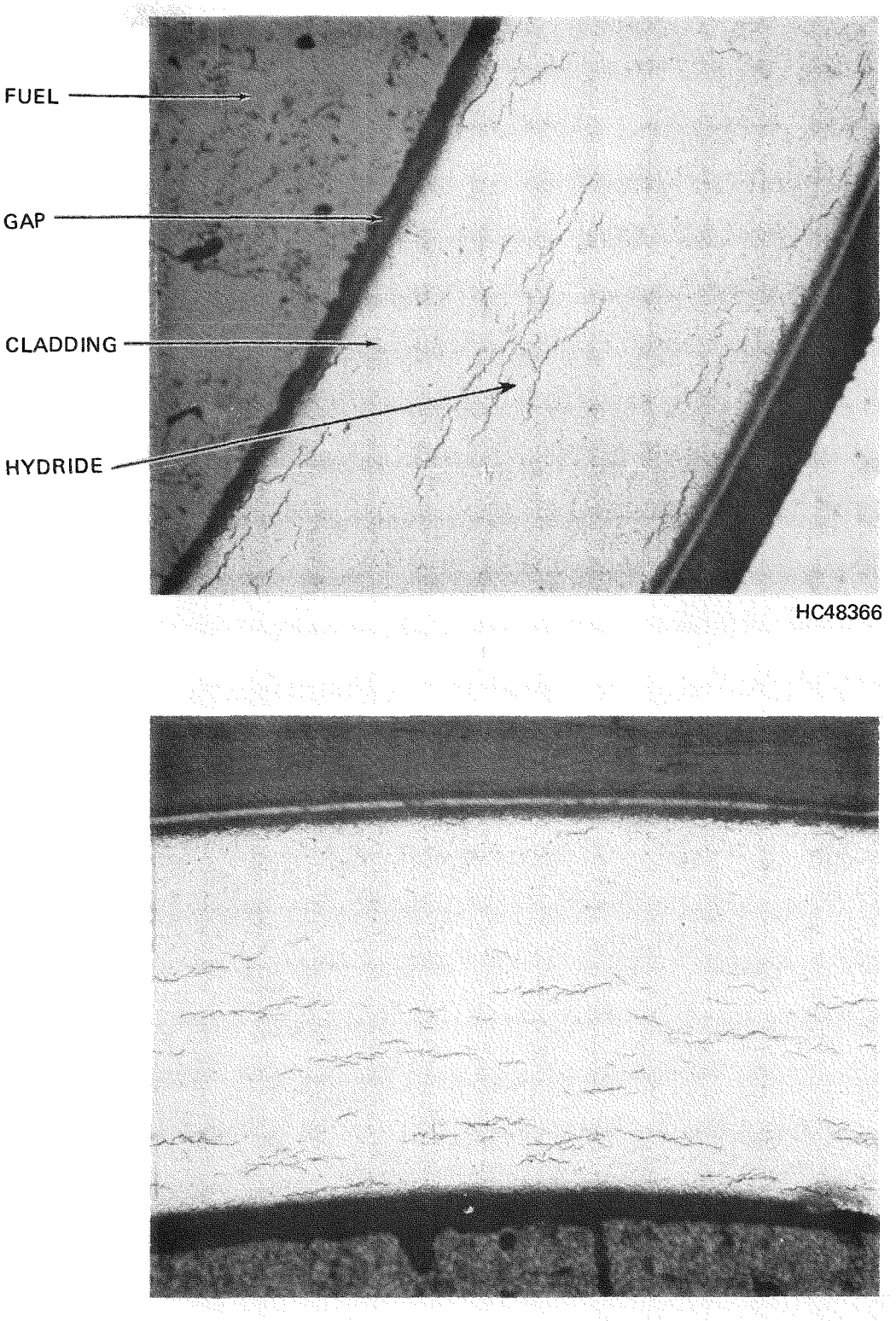

FIGURE 18. Photomicrographs of More Prevalent Zirconium Hydride Formation in Cladding of Samples G9-29 (115.5 in.) and I9-31 (134.5 in.) at 500X.

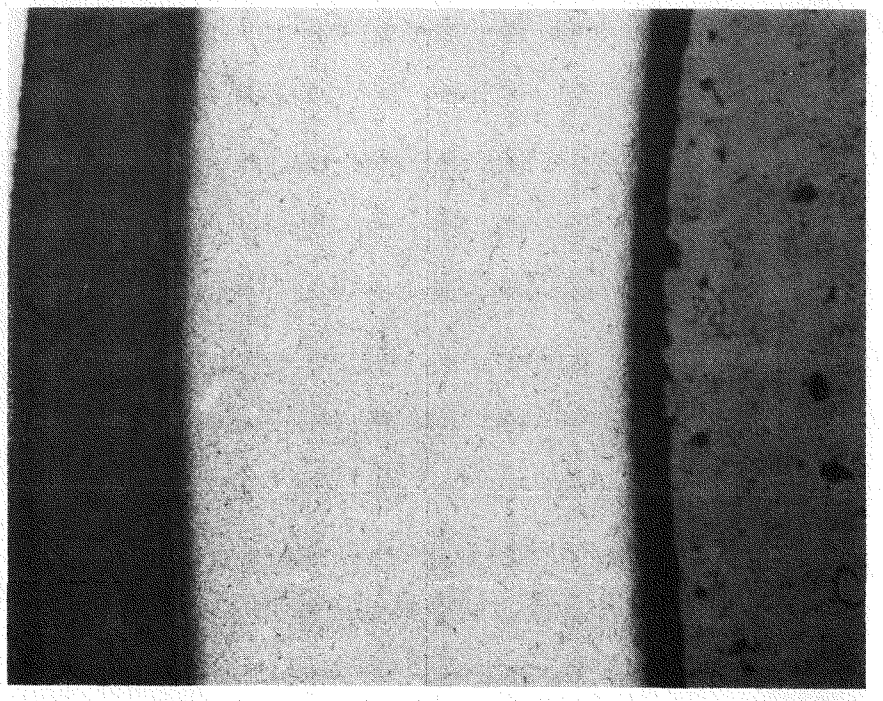

HC48354

MOUNTING EPOXY | CLADDING | GAP | FUEL

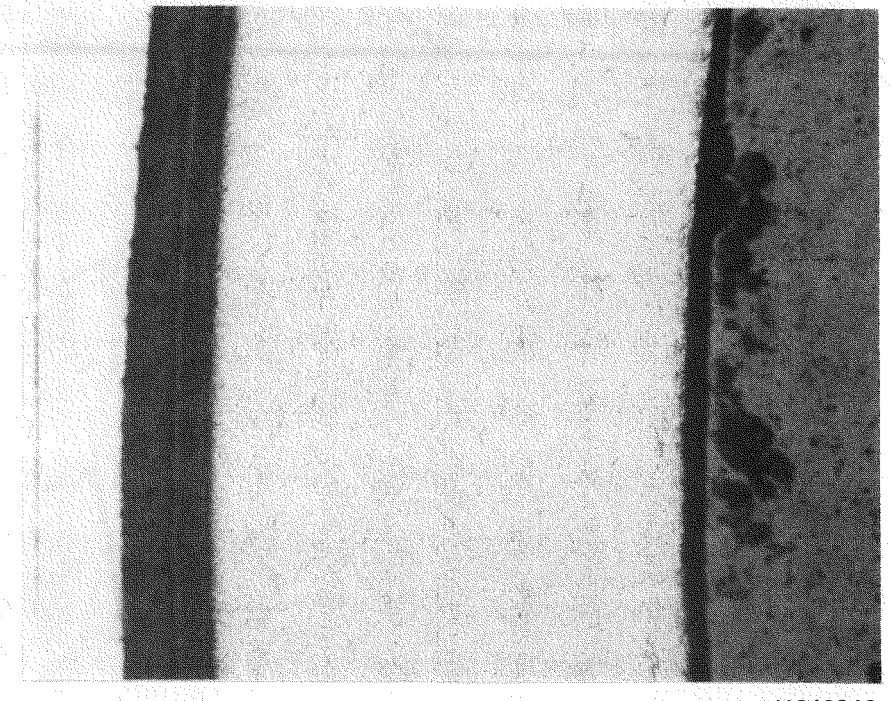

HC48346

FIGURE 19. Photomicrographs of Cladding Microstructure of Samples G9-4 (16.5 in.) and G7-10 (45.0 in.) at 100X.

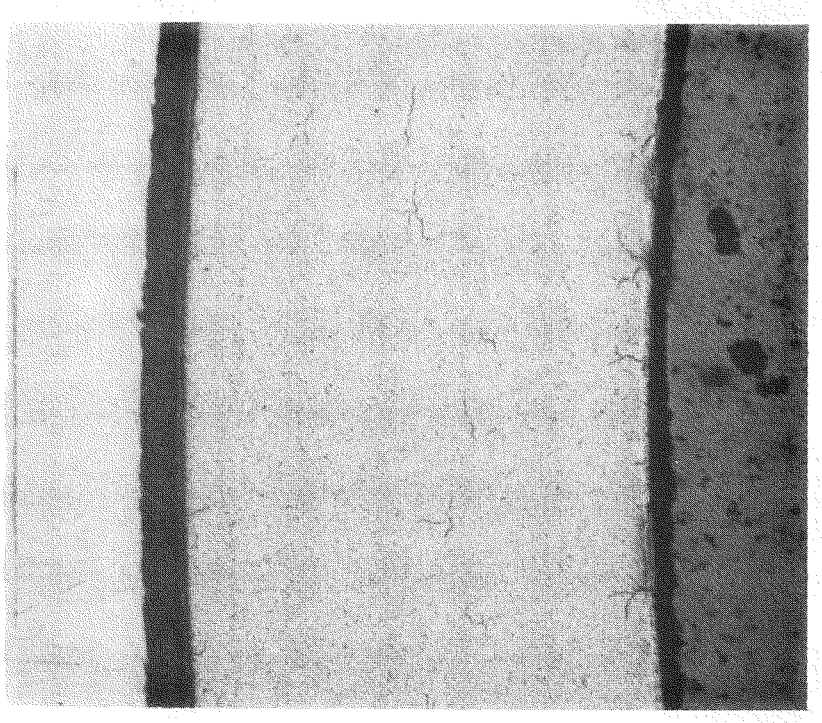

HC48358

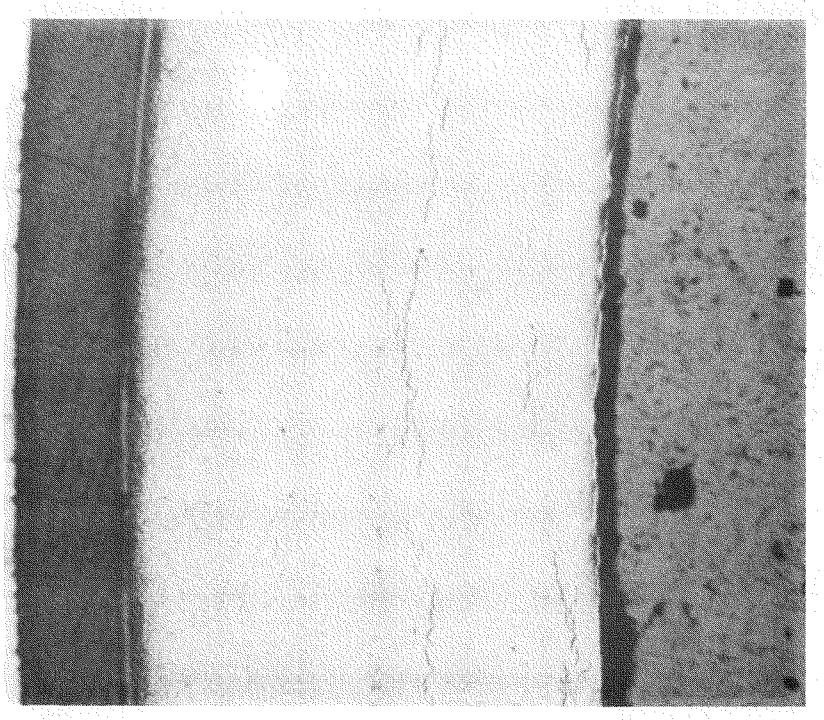

HC48350

FIGURE 20. Photomicrographs of Cladding Microstructure of Samples G9-14 (71.0 in.) and G7-22 (91.0 in.) at 100X.

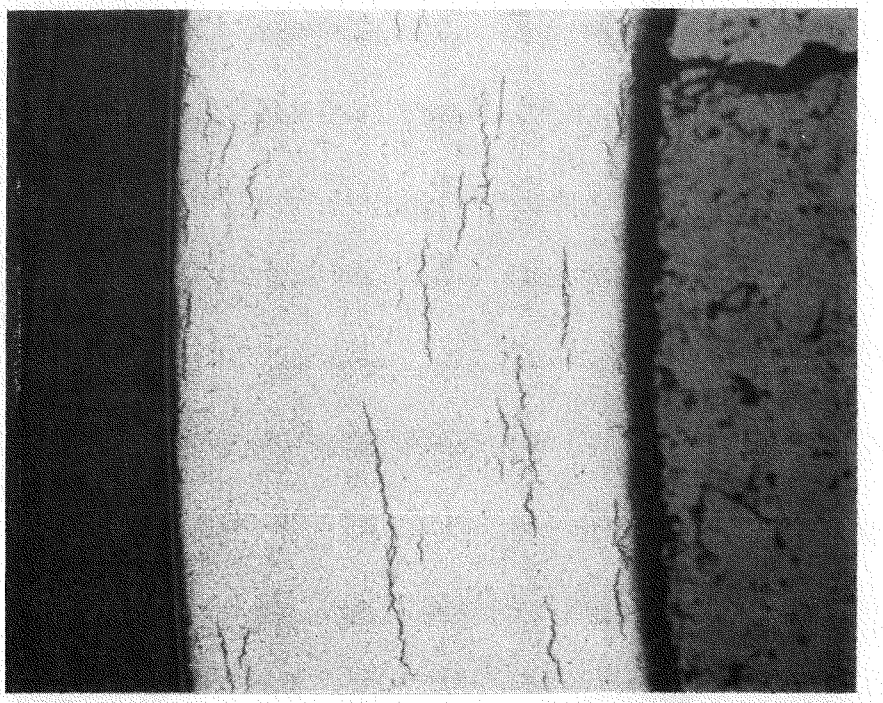

HC48362

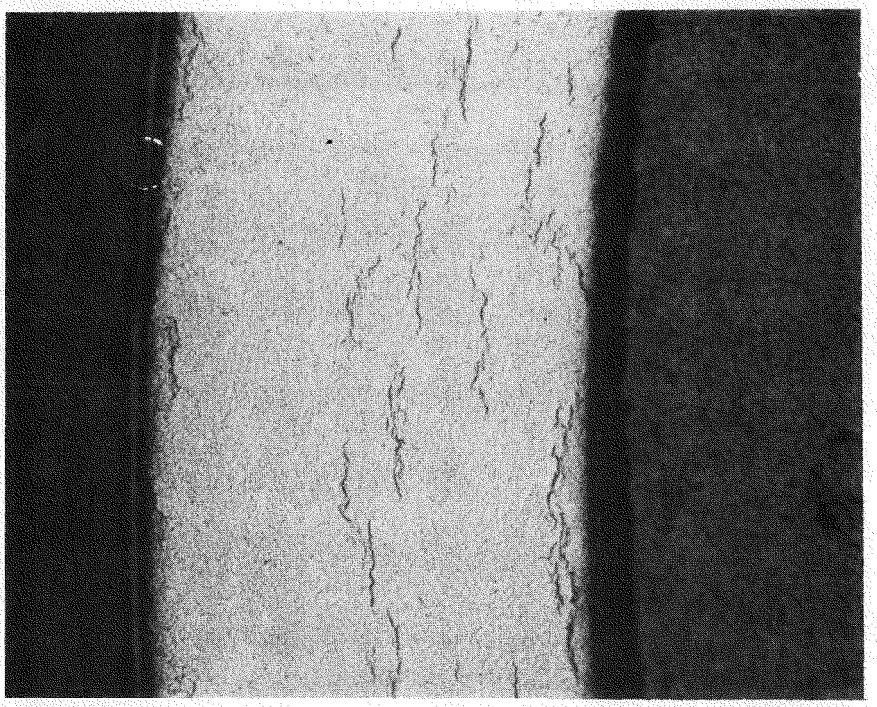

HC48371

FIGURE 21. Photomicrographs of Cladding Microstructure of Samples G9-29 (115.5 in.) and I9-31 (134.5 in.) at 100X.

4. Fuel-Cladding Chemical Interaction

All samples showed evidence of fuel-cladding chemical interaction. The reaction products (a compound of fuel, cladding, and fission products) appeared as localized globules (see Figure 22) and semicontinuous layers (see Figure 23). The localized reaction products appeared in samples taken from the bottom of the rod, and the layered reaction products were prevalent in samples from the middle and top of the rod.

The reaction products penetrated the cladding 5 to 40 microns. Reaction products also appeared adjacent to pieces of fuel lodged in the gap as shown in Figure 24. Figure 25 shows a reaction product directly adjacent to a fuel crack and a reaction layer with a two-phase appearance.

5. End Cap Examination

The top and bottom end caps of rod G9 were sectioned and mounted longitudinally. Macrographs were taken of the end caps at 7X magnification in the as-polished and etched condition. The etched samples showed the heat-affected zone caused during fabrication. A noted difference in the grain size at the weld areas was seen between the top and bottom end caps. The grain size in the top end cap was larger than that of the bottom end cap. Figures 26 and 27 show the longitudinal cross section of the end caps from rod G9. Photomicrographs show the deformed cladding where the end caps tapered inside the rod. No reaction products or deposits were seen.

6. Sample from Spacer Grid Location

Sample G9-18 (77.5 in.) was mounted longitudinally and examined in the as-polished condition. A 7X-macrograph (shown in Figure 28) was taken to document cladding and fuel structures. This sample, taken from a grid spacer location where the nondestructive examination results showed a scuffed surface, indicated no evidence of grid spacer wear or cladding thinning. The fuel microstructure showed cracks extending axially along the length of the pellet that appeared as if they extended through the

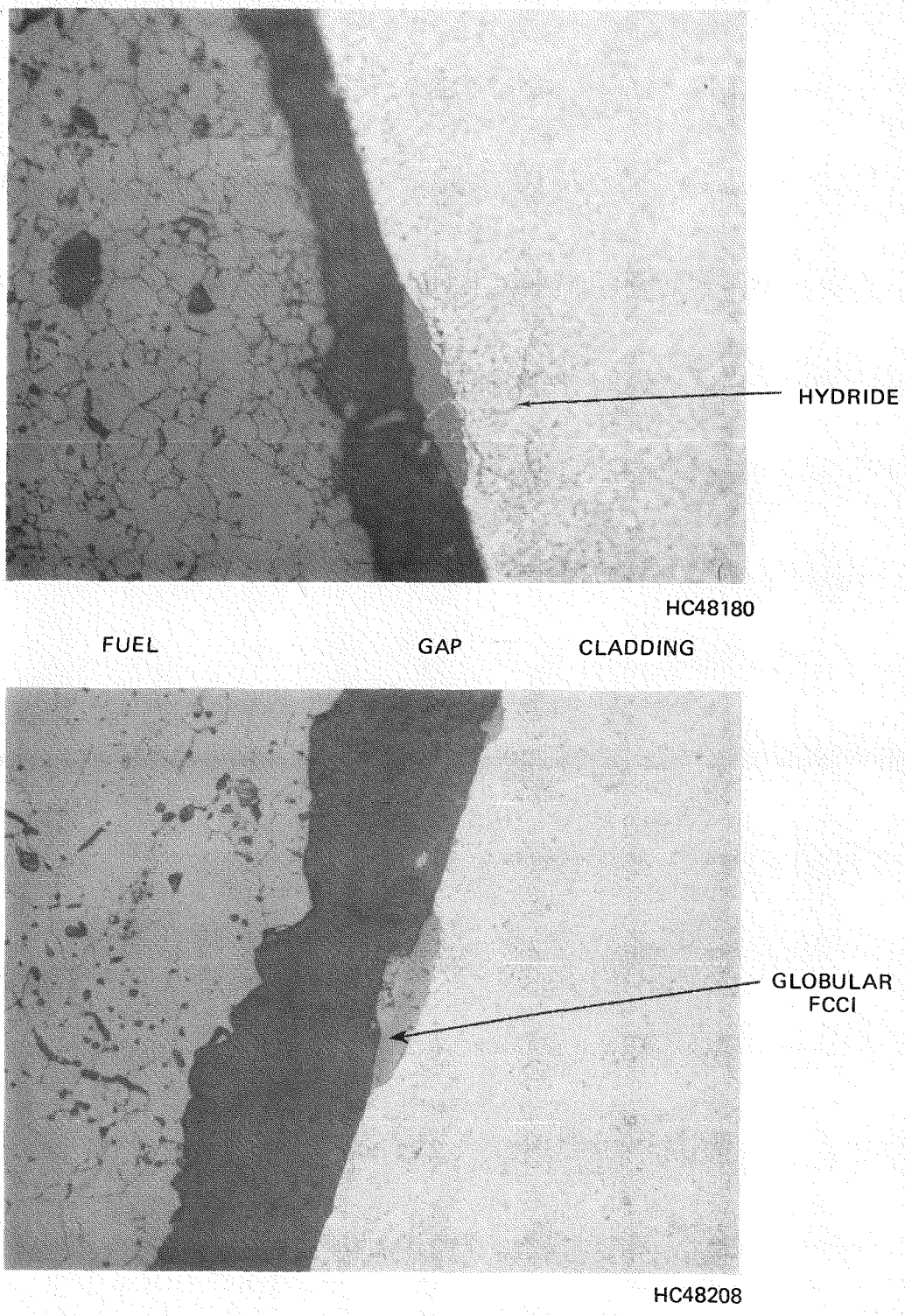

FIGURE 22. Photomicrographs of Globular Fuel-Cladding Chemical Interaction on Samples G9-16 (71.0 in.) and G9-4 (16.5 in.) at 500X.

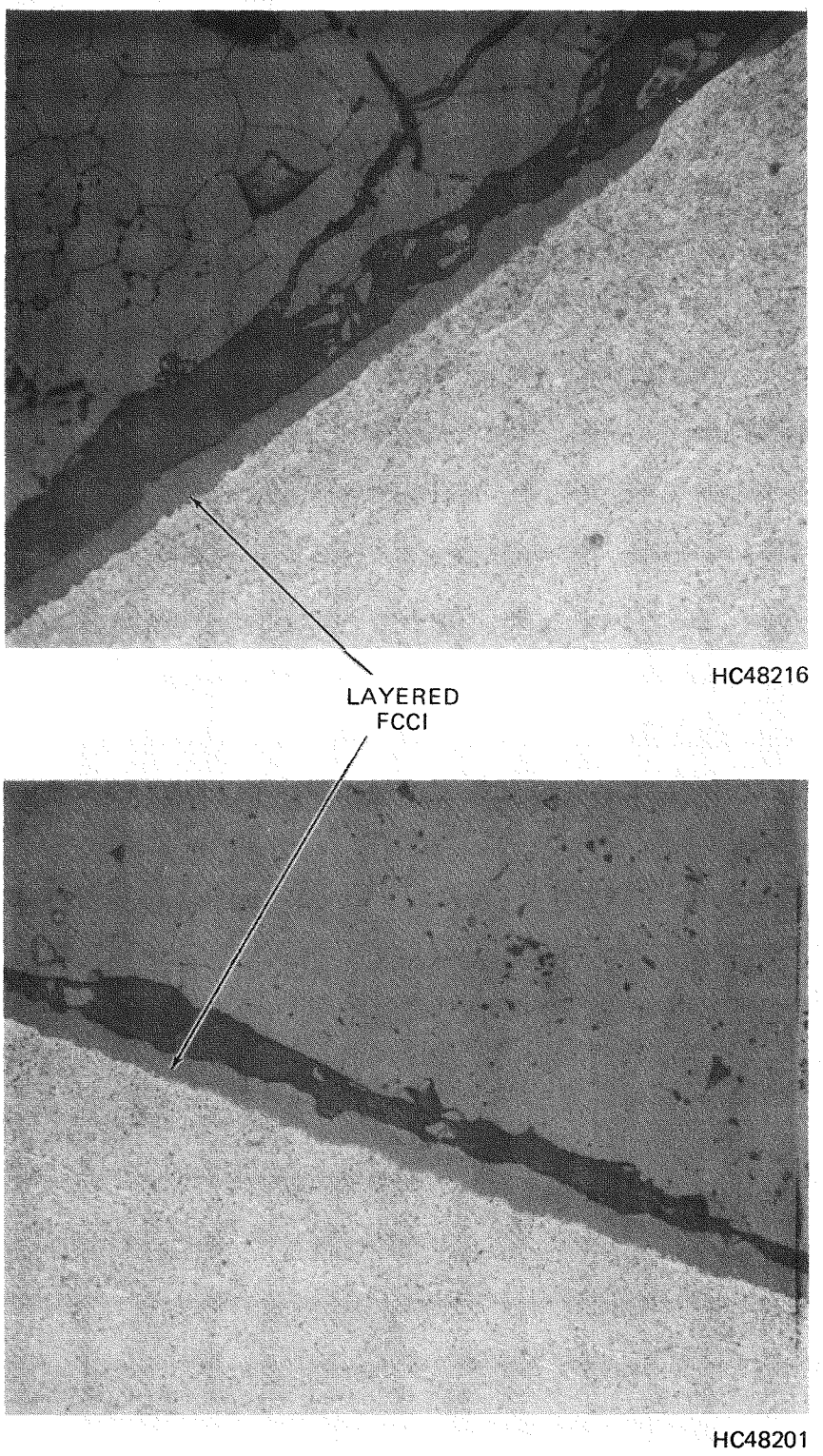

FIGURE 23. Photomicrographs of Layered Fuel-Cladding Chemical Interaction on Samples G9-29 (115.5 in.) and H6-20 (91.0 in.) at 500X.

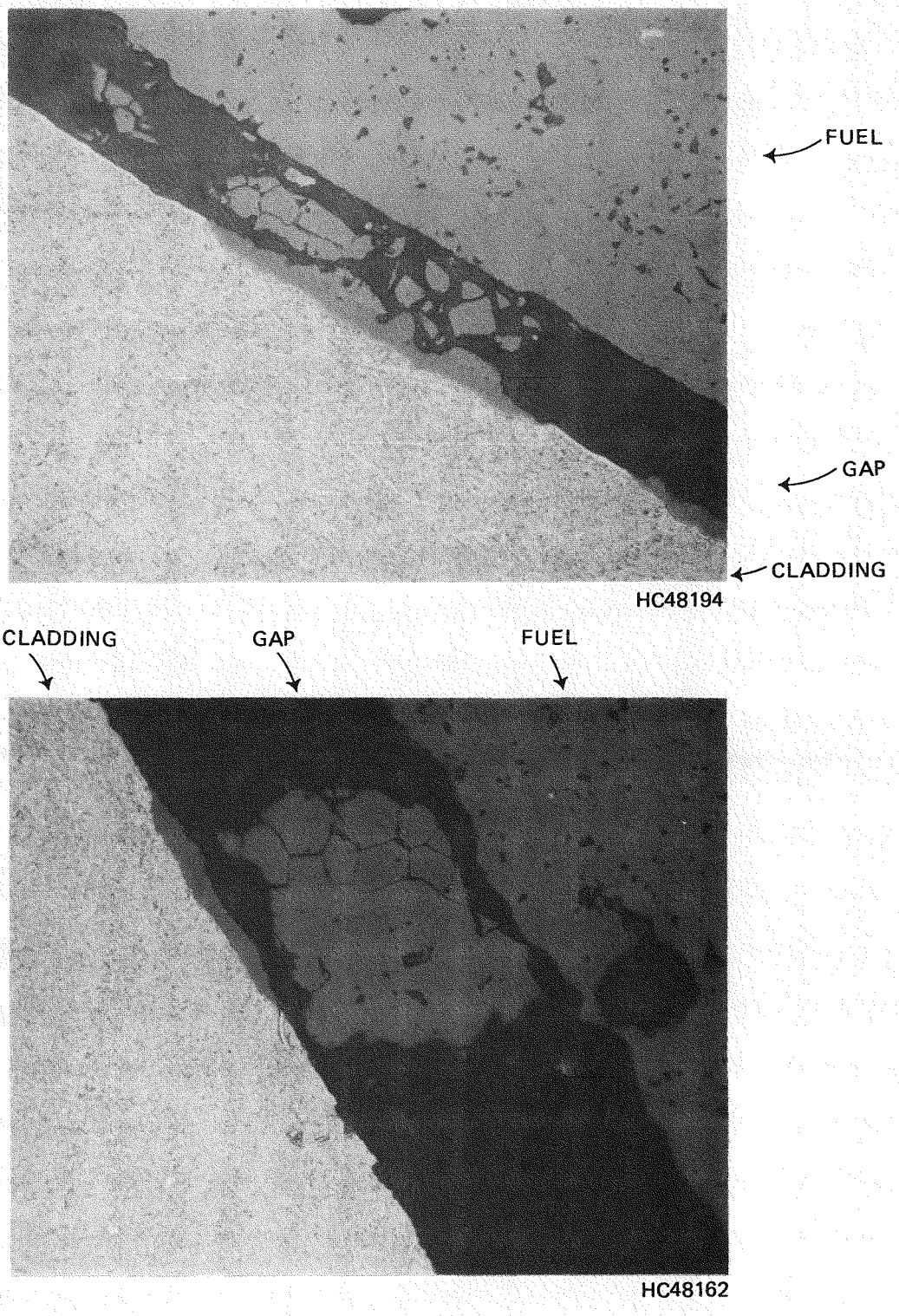

FIGURE 24. Photomicrographs of Fuel-Cladding Chemical Interaction and Fuel Particle in Gap on Samples I9-14 (71.0 in.) and J8-25 (115.5 in.) at 500X.

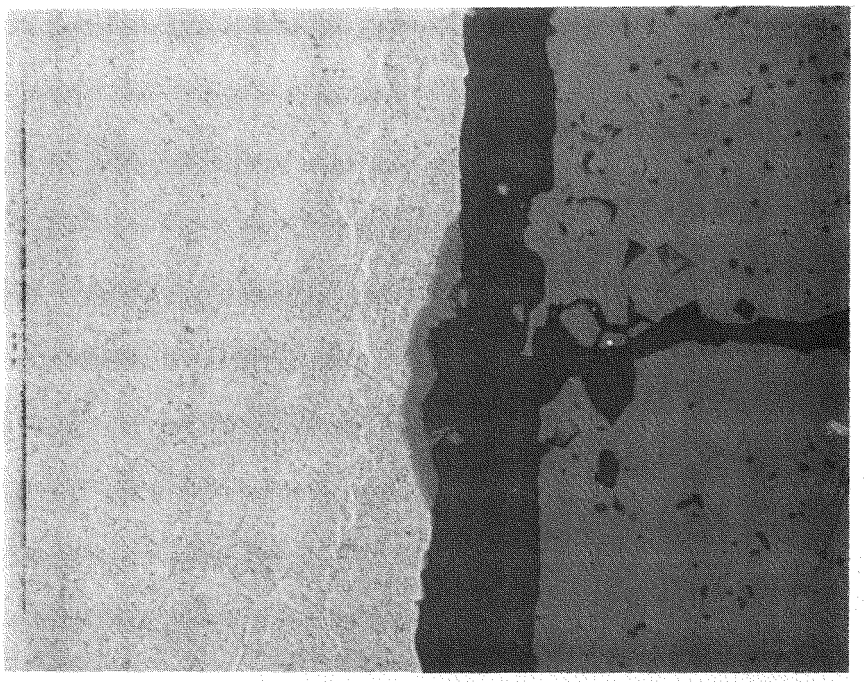

HC48161

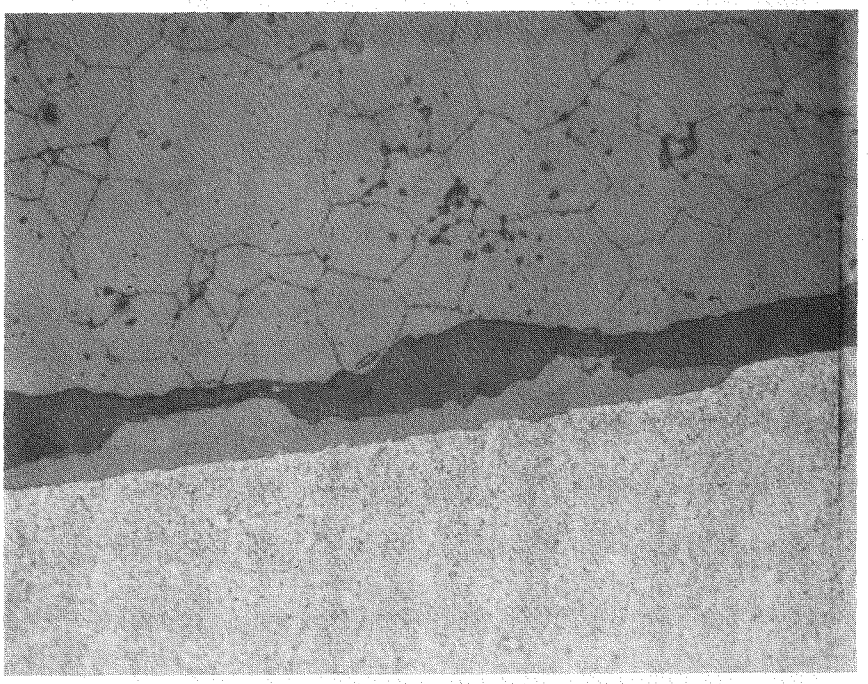

HC48211

FIGURE 25. Photomicrographs of Fuel-Cladding Chemical Interaction on Samples J8-25 (115.5 in.) and G9-8 (45.5 in.) at 500X.

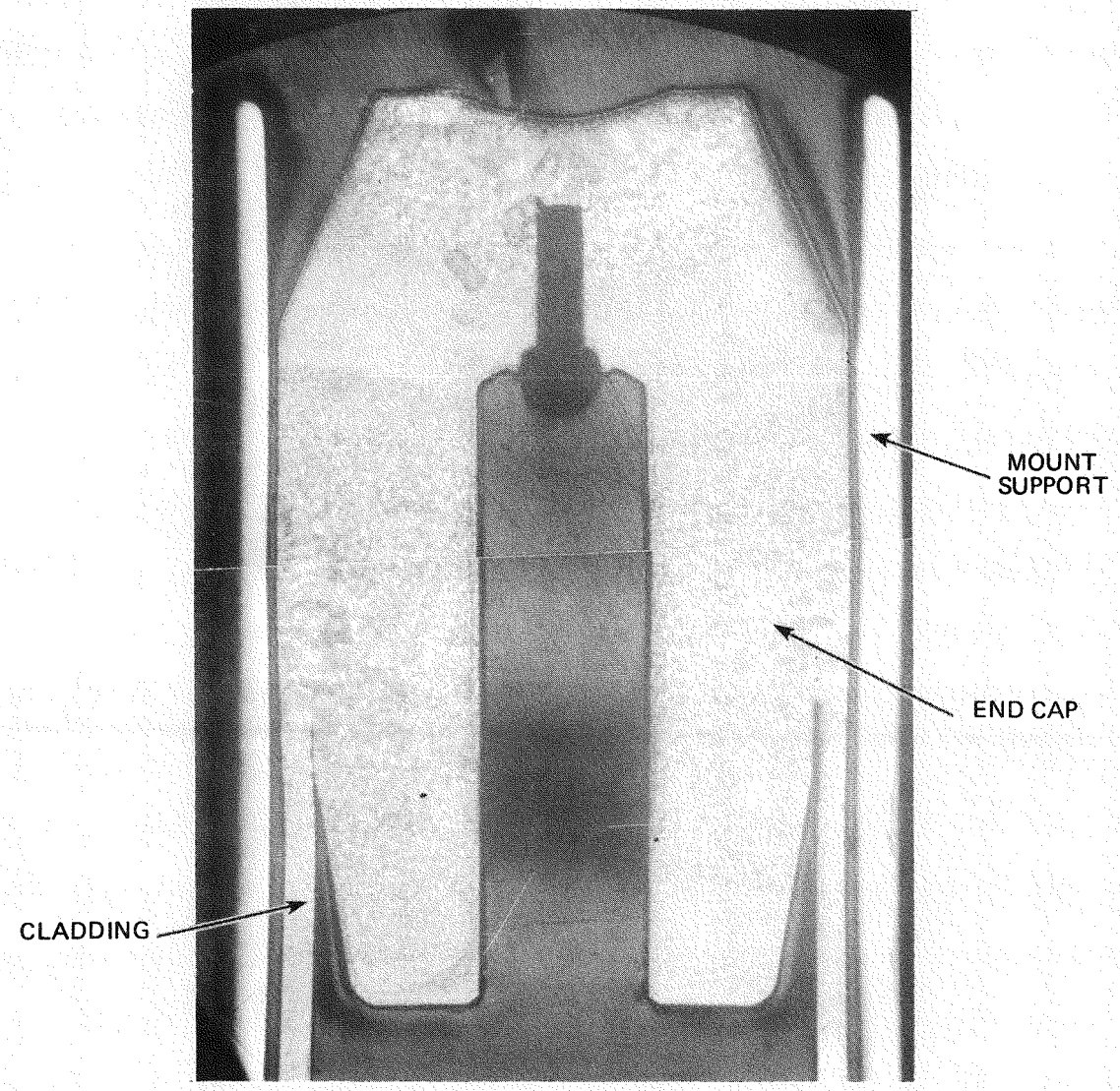

FIGURE 26. Photomicrograph of Top End Cap Microstructure of Sample G9-41 (152.0 in.) at 7X.

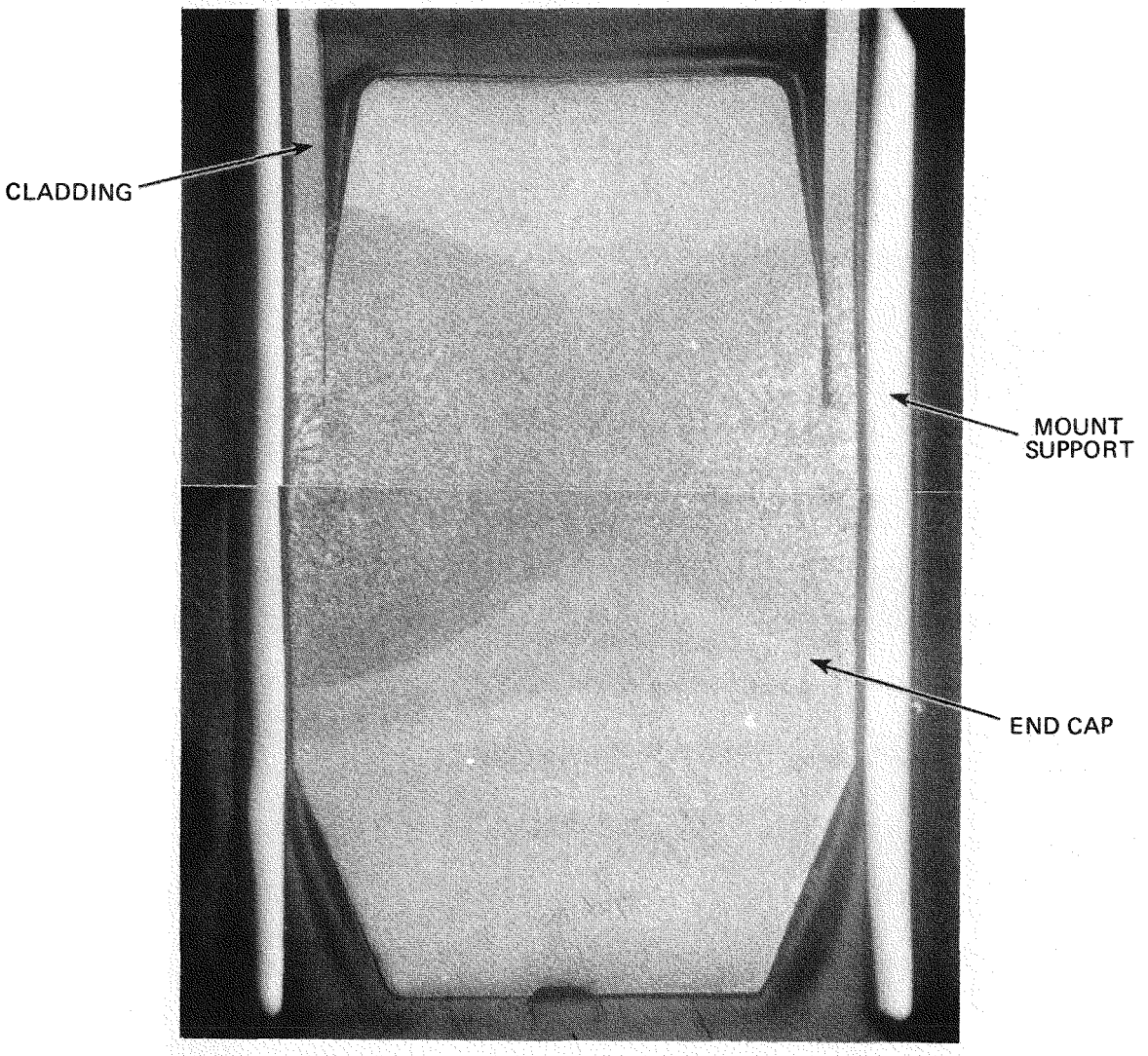

FIGURE 27. Photomicrograph of Bottom End Cap Microstructure of Sample G9-1 (1.0 in.) at 7X.

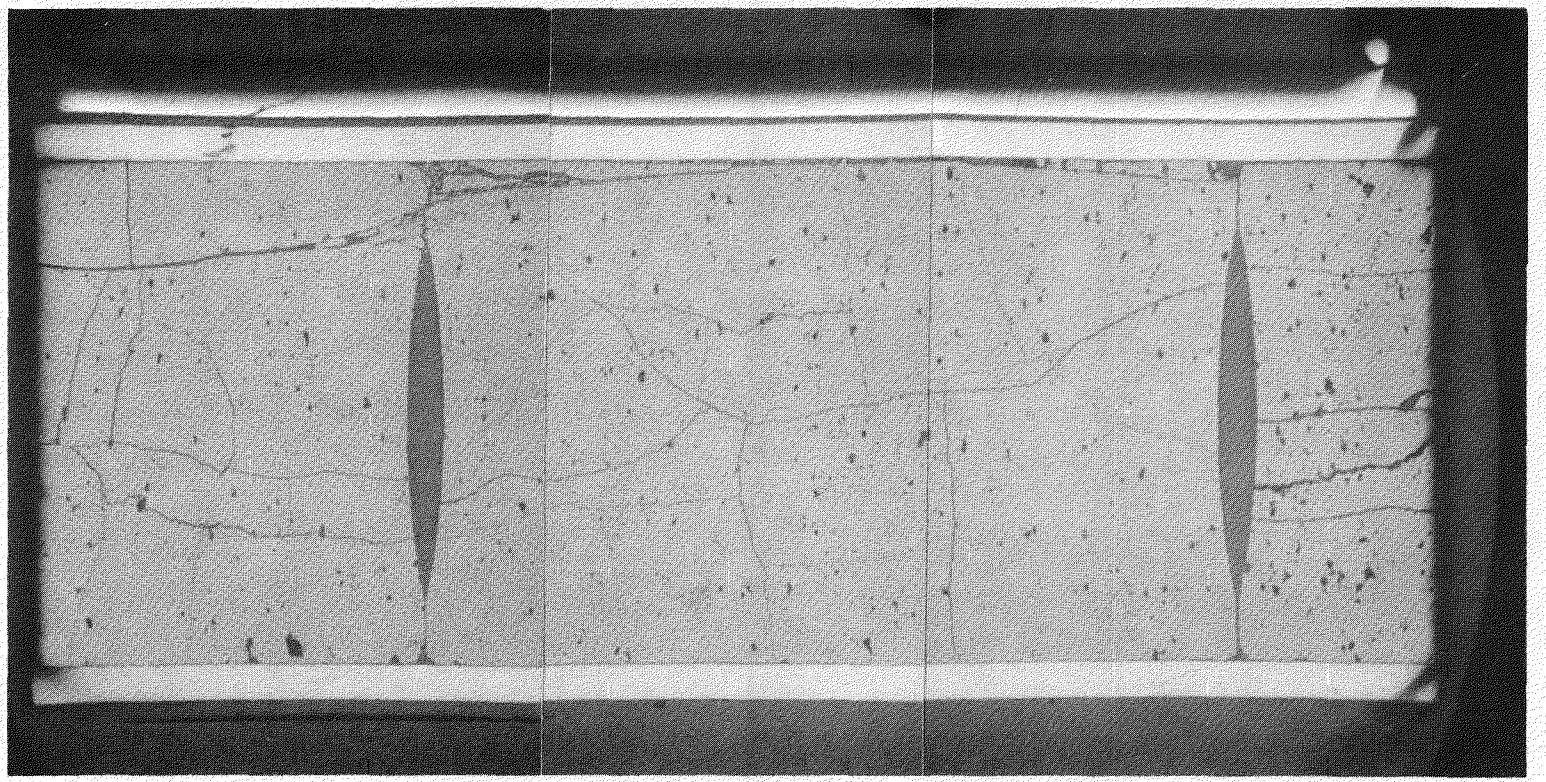

FIGURE 28. Mosaic of Longitudinal Cross Section of Fuel Rod at Spacer Grid Location of Sample G9-18 (79.0 in.) at 7X.

pellet-pellet interface into the adjacent pellet on both sides. The corner of one pellet fragmented, and pieces fell into the gap. The gap was shown to have fuel fragments measuring several hundred microns and areas of bonded fuel and cladding. A uniform layer of reaction product (∿40 microns thick) was shown on the cladding inner surface. The zirconium hydrides were oriented longitudinally in the cladding.

F. AUTORADIOGRAPHY

The purpose of alpha and beta-gamma autoradiography is to qualitatively determine the relative distributions of alpha and beta-gamma emitting species in an irradiated fuel sample. The principal alpha emitters are plutonium and transuranics (Np, Am, and Cm). The beta and gamma emitters are uranium and fission products.

The samples were typical metallographic fuel sections with as-polished surfaces. The apparatus for autoradiography consists of an out-of-cell light-tight glovebox, transfer tube through the cell wall, in-cell film exposure device, and transfer mechanism. Alpha autoradiography uses a special cellulose nitrate film; beta-gamma autoradiography uses a common high-resolution photographic film.

The samples for autoradiography were slightly etched and washed with ethyl alcohol before being placed in the exposure device. The film was placed in contact with the sample and the exposure was made. The film was then removed and developed using standard photographic techniques.

Seven samples* were selected for autoradiography; Figures 29 and 30 show typical autoradiographs of G9-22 (91.0 in.). Figure 31 shows the as-polished surface for comparision. Alpha emitters and beta-gamma emitters are indicated by light gray on the autoradiographs. The alpha autoradiograph

*G7-4 (16.5 in.), G7-28 (115.5 in.), G7-36 (134.5 in.), G9-22 (91.0 in.), J8-25 (115.5 in.), I9-25 (115.5 in.), and H6-25 (115.5 in.).

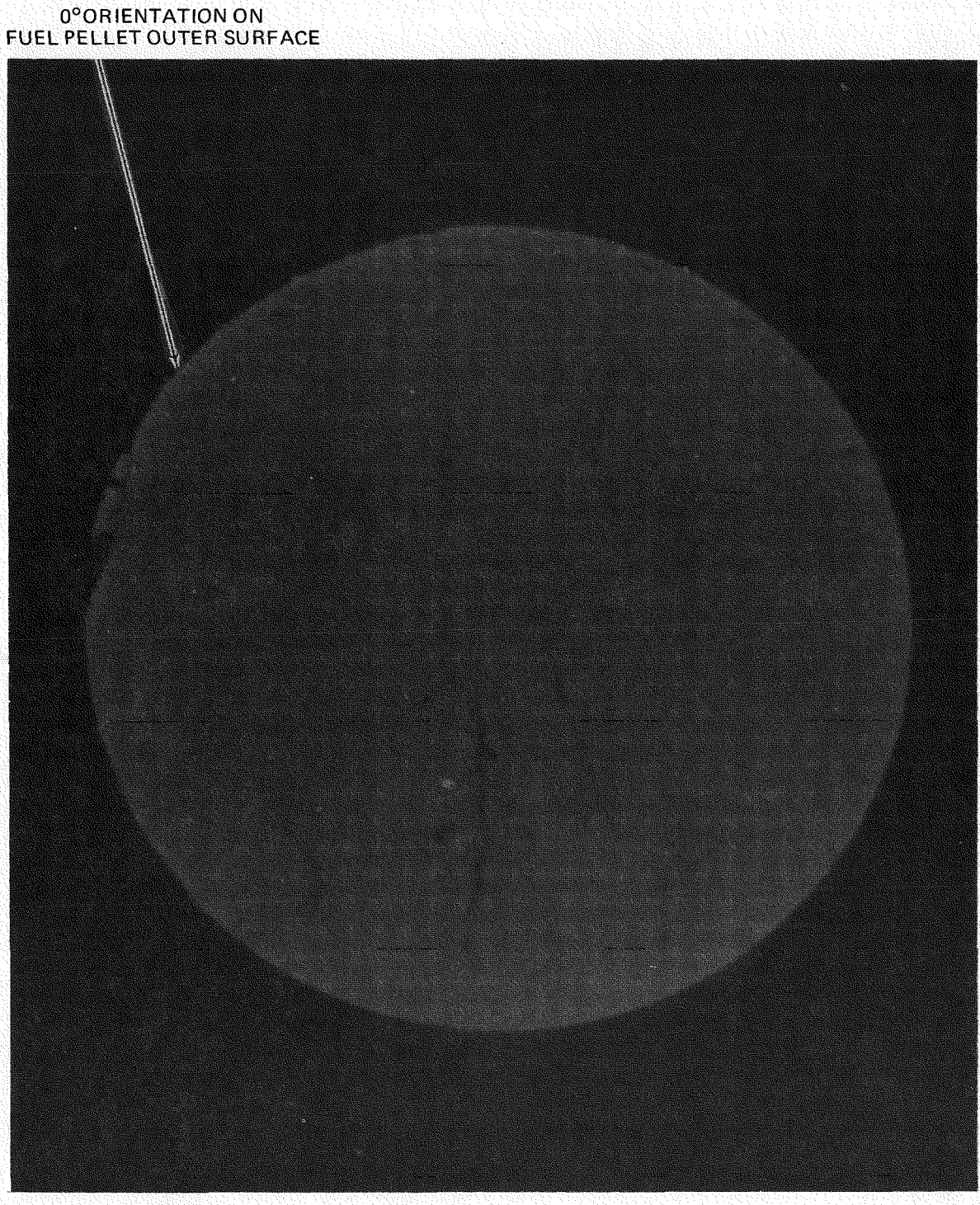

FIGURE 29. Alpha Autoradiograph of Sample G9-22 (91.0 in.).

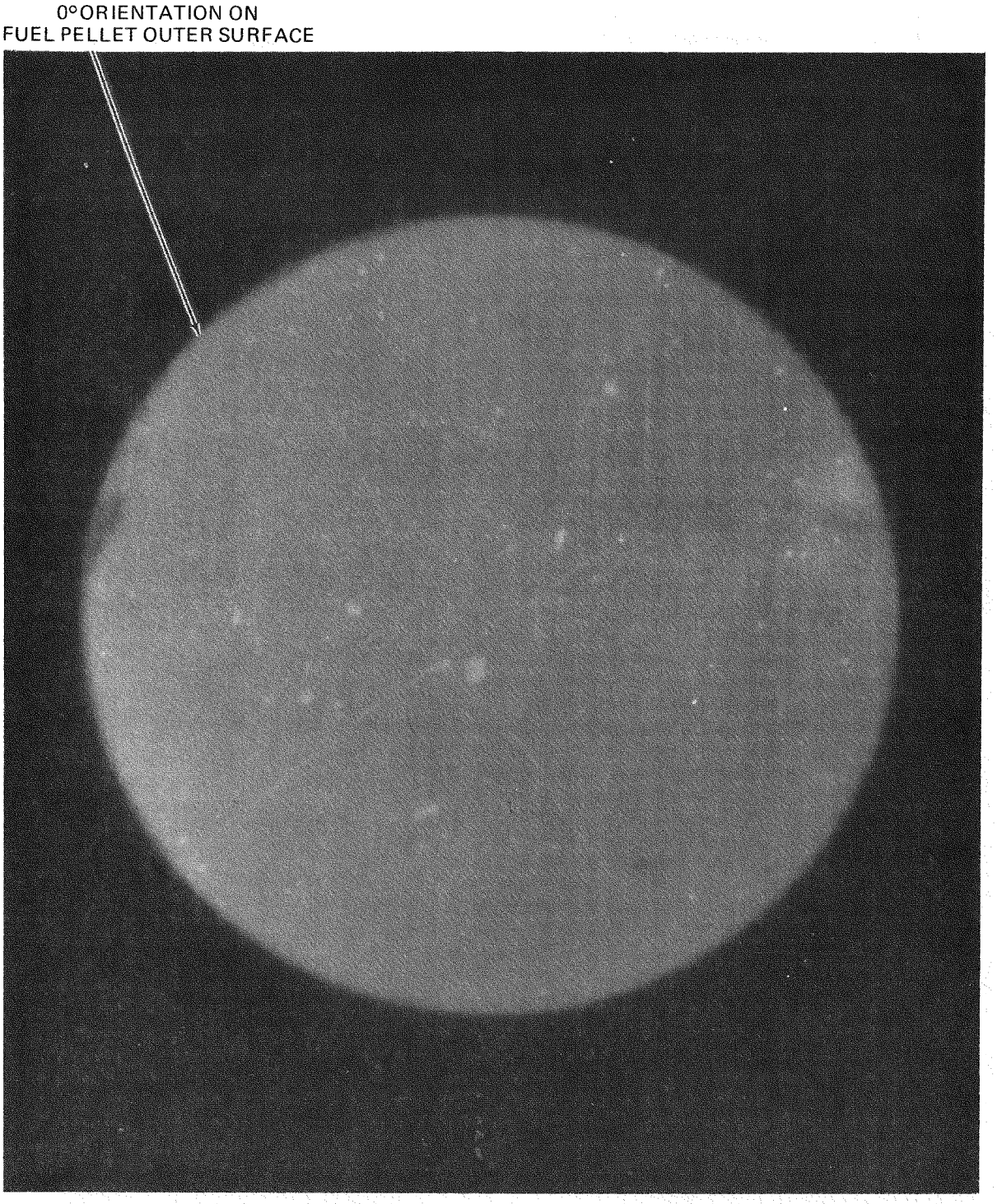

FIGURE 30. Beta-Gamma Autoradiograph of Sample G9-22 (91.0 in.).

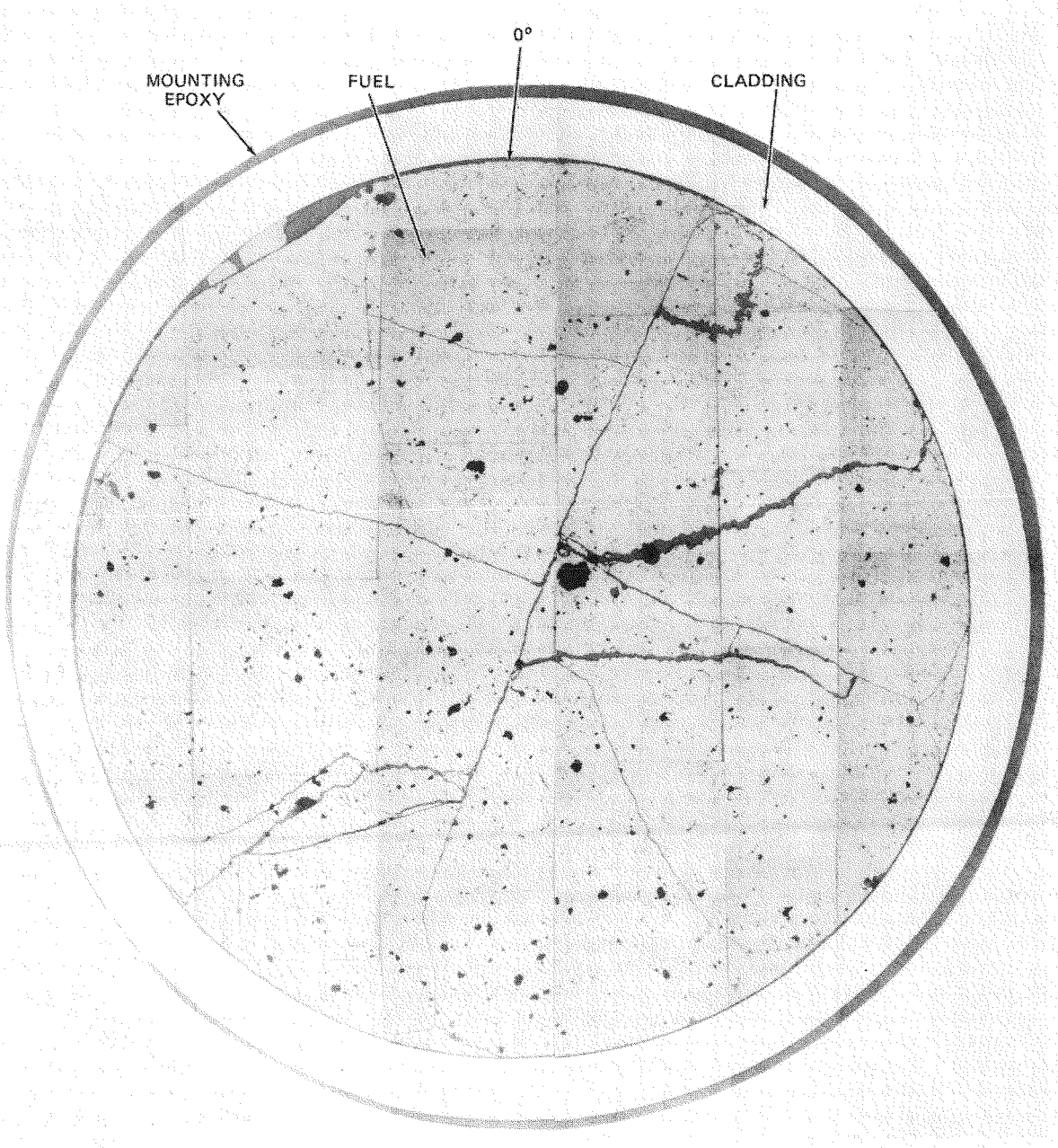

FIGURE 31. Mosaic of Sample G9-22 (91.0 in.). Neg 7908542-2

shows an even distribution of alpha emitters in the fuel within the sensitivity of detection. The beta-gamma autoradiograph of the same sample shows several areas that indicate higher concentrations of beta or gamma emitters. A comparison of the optical photomicrograph (see Figure 31) to the autoradiograph shows coincidence between cracks and some pores in the fuel. Volatile fission products are known to coincide on the free surfaces of cracks and pores.

G. FUEL BURNUP DETERMINATION

Eight fuel rod sections* were prepared for burnup analysis. Four sections were prepared from rod G7 and one each from the other four rods. Five of the samples were taken at the same distance from the fuel rod bottom; the other three were selected adjacent to metallographic samples. Table 8 shows the results of the burnup determination.

Burnup values ranged from 19,890 MWd/MTU at the top of the rod to 27,700 MWd/MTU at the middle of the fuel column. Samples taken from all five rods at identical locations varied from 27,700 to 26,600 MWd/MTU.

Burnup was determined according to ASTM E-267 and ASTM E-321. Apparatus for burnup determination consisted of a semi-microanalytical balance, Erlenmeyer flask, hot plate, reflux condenser, and a mass spectrometer.

The sections used for burnup measurements were cut in 1/2-inch lengths by the cutting methods described previously. The rod section was immediately placed into a clean vial and accurately weighed. The fuel sample was then separated from the cladding by placing it into a flask of 12 N HNO_3 and heating it. Once the cladding came free of the fuel, it was rinsed

*G9-13 (70.0 in.), G7-6 (16.5 in.), G7-15 (70.0 in.), G7-35 (134.5 in.), G7-30 (116.5 in.), J8-13 (70.0 in.), H6-13 (70.0 in.), and I9-13 (70.0 in.).

TABLE 8

BURNUP ANALYTICAL RESULTS AND CALCULATIONS

Sample	Location	Atom Percent U-Isotope/U-Total ^{234}U	^{235}U	^{236}U	^{238}U	Pu-Isotope/Pu-Total ^{238}Pu	^{239}Pu	^{240}Pu	^{241}Pu	^{242}Pu
G9-13	70.0-70.5	0.012	0.799	0.335	98.854	1.352	57.991	24.894	10.942	4.821
G7-6	16.5-17.0	0.014	0.802	0.318	98.866	1.119	59.606	24.402	10.644	4.229
G7-15	70.0-70.5	0.013	0.737	0.330	98.920	1.327	57.894	24.972	11.005	4.802
G7-35	134.5-135.0	0.014	1.058	0.283	98.645	0.804	65.334	21.506	9.579	2.777
G7-30	116.5-117.0	0.013	0.755	0.324	98.908	1.306	58.245	24.529	11.163	4.757
J8-13	70.0-70.5	0.014	0.728	0.335	98.923	1.377	57.415	25.193	11.055	4.960
H6-13	70.0-70.5	0.014	0.723	0.334	98.929	1.359	57.348	25.289	11.031	4.973
I9-13	70.0-70.5	0.013	0.718	0.330	98.939	1.685	57.389	25.041	10.988	4.897

with HNO_3, dried, and returned to the vial. The vial was again weighed; the difference between the weights was the weight of the fuel. The fuel and acid were allowed to react until there was complete dissolution of the fuel, which usually took several hours. Afterward the solution was diluted to obtain a concentration of 1 mg/ml. The diluted samples were mass spectrometrically analyzed for neodymium-148 and heavy element concentrations.

Extreme care was taken in cutting, handling, and preparing the aliquot samples to prevent contamination from environmental uranium and atmospheric dust. All glassware was new and boiled for several hours in HNO_3. Clean forceps, oven-dried glassware, and redistilled water were used to prevent contamination.

Burnup calculations were based on the formula

$$F_T = \frac{F' \times 100}{U' + P' + F'}$$

TABLE 8 (Cont'd)

Atom Ratios						
$^{148}Nd/^{238}U$ ($\times 10^{-4}$)	$^{239}Pu/^{238}U$ ($\times 10^{-3}$)	F' (Fissions / Atom ^{238}U)	U' (Atoms U / Atom ^{238}U)	P' (Atoms Pu / Atom ^{238}U)	F_t' (Atom Percent / Burnup)	Burnup (MWd/MTU)
4.95	5.02	0.029464	1.011593	0.008657	2.806	26,940
4.69	4.88	0.027917	1.011470	0.008187	2.665	25,580
5.06	5.10	0.030119	1.010918	0.008809	2.869	27,540
3.63	4.89	0.021607	1.013736	0.007485	2.072	19,890
4.99	5.13	0.029702	1.011041	0.008808	2.830	27,170
5.09	5.06	0.030298	1.010887	0.008813	2.886	27,700
5.09	5.08	0.030298	1.010826	0.008858	2.886	27,700
4.89	4.84	0.029107	1.010724	0.008434	2.777	26,660

where: F_T = Total heavy element atom percent burnup,

F' = Fissions per atom ^{238}U,

U' = Number of uranium atoms per atom ^{238}U, and

P' = Number of plutomium atoms per atom ^{238}U.

The number of fissions was determined by the quantitative analysis of ^{148}Nd divided by the ^{148}Nd fission yield; 0.0168 for a ^{235}U fission.

H. HYDROGEN ANALYSIS

Zirconium hydrides are known to have adverse effects on the mechanical properties of the cladding. Quantitative analysis was made for the hydrogen content of the cladding.

Eight cladding samples* were prepared for hydrogen analysis, Samples were cut in 1/4-inch lengths and the fuel removed. The fuel that

*G7-25a (104.75 in.), G9-2a (1.0 in.), G9-17a (76.5 in.), G9-27a (109.75 in.), G9-34a (133.75 in.), H6-22a (104.75 in.), I9-22a (104.75 in.), and J8-22a (104.75 in.).

remained was removed by brushing and cleaning in a HNO solution and rinsing with alcohol (as described in Section D).

The samples were analyzed by vacuum fusion and the hydrogen content analysis is given in Table 9. Samples taken from the bottom half of the fuel rod were found to have lower hydrogen concentrations than the top half. Samples from the same axial rod location show similar hydrogen concentrations. Comparison of these analyses to the photomicrographs of etched cladding surfaces allows a qualitative interrelationship between hydride morphology and hydrogen concentration.

TABLE 9

HYDROGEN CONTENT ANALYSIS

Sample Number	Location (in.)	ppm of H_2		
		Analysis 1	Analysis 2	Average Concentration
G7-25A	104.75	66	63	65
G9-2A	1.0	38	34	36
G9-17A	76.5	27	46	36
G9-27A	109.75	56	62	59
G9-34A	133.75	75	65	70
H6-22A	104.75	67	77	72
I9-22A	104.75	71	82	77
J8-22A	104.75	52	59	56

I. SHIELDED ELECTRON MICROPROBE ANALYSIS

Four samples* were selected for microprobe examination and analysis and were examined in the as-polished condition with a carbon coating for electrical conductivity. A Materials Research Corporation Model 450 shielded electron microprobe was used.

Ten areas of interest were examined with a combination of wavelength scans, x-ray images, step scans, and line profiles. A summary of the areas and methods of analysis is provided in Table 10. The areas examined were: bonded fuel-cladding regions, layers of reaction products found on the cladding inner surface, and metallic particles in the fuel. Mosaics of the sample surface illustrating the location of the areas examined are shown for each sample in Figures 32 through 35.

In summary, three areas of fuel-clad bonding were located on the four samples. X-ray photomicrographs of the zirconium, uranium, and fission products showed matrix cladding attack by fuel and fission products penetrating 20-40 microns into the cladding. No grain boundary attack was seen. No gross migration or segregation trends of fuel or cladding materials were seen. No unexpected impurity elements were found within the cladding, and the cladding appeared to be of good integrity. The metallic particles in the fuel were analyzed as either high iron content particles or stainless-steel-type materials with unknown origins.

1. Sample G7-4 (16.5 in.)

An area of cladding inner surface reaction product at 200° circumferential orientation was qualitatively analyzed by x-ray imaging as shown in Figure 36. Zirconium and uranium x-ray images showed the relative locations of the elements. Zirconium depletion on the cladding outer surface in the reaction product layer was apparent.

*G7-4 (16.4 in.), G7-16 (91.0 in.), G9-22 (91.0 in.), and G7-28 (115.5 in.).

TABLE 10

SUMMARY OF MICROPROBE SAMPLES EXAMINED
AND TYPE OF ANALYSIS

Sample	Location	Type of Analysis
G7-4	200°	Cladding ID Oxide-2θ; EBS; U X-ray; Zr X-ray
G7-4	300°	Metallic Particle-2θ; EBS; U X-ray; Fe X-ray; Ni X-ray; Cr X-ray
G7-4	335°	Metallic Particle-2θ; EBS; U X-ray; Fe X-ray; Ni X-ray; Cr X-ray; Fixed Time Point Counts-Metallic Particle, Fe, Cr, Ni, Std
G7-16	185°	Metallic Particle-2θ; EBS; U X-ray; Zr X-ray
G7-16	105°	Cladding Edge with Particles-2θ; EBS; U X-ray; Zr X-ray
G7-16	340°	Cladding ID Gray Phase-2θ; EBS; U X-ray; Zr X-ray
G7-28	260°	Bonded Fuel-2θ; EBS(2); U Mα X-ray; U Mβ X-ray; Zr Lα X-ray; Cs Lα X-ray; Pu M X-ray; Ce Lα X-ray; Sn Lα X-ray; Ru Lα X-ray; Mo Lα X-ray; U Mβ Ratemetered Line Profile-Vertical and Horizontal; Zr Lα Ratemetered Line Profile-Vertical and Horizontal
G9-22	45°	Bonded Fuel-2θ; EBS; U X-ray; Zr X-ray; Sn X-ray; Pu X-ray; Cs X-ray; 2 Micron Scan in 308 Steps; EBS (end of run)
G9-22	285°	Cladding ID Oxide-2θ; EBS; U X-ray; Zr X-ray

The metallic particle at 300° showed a high concentration of iron with lesser amounts of nickel and chromium. A relative indication of the amounts is shown in Table 11 and by the x-ray images in Figure 37.

A large, oblong metallic particle 80 μm (0.003 in.) in length at 335° is shown in Figure 38 with the corresponding x-ray images for iron, chromium, nickel, and uranium. Wavelength scan results are shown in Table 11. The particle was semiquantitatively analyzed to consist of 59% iron, 8.6% chromium, and 13% nickel as outlined by fixed time counting results in Table 12.

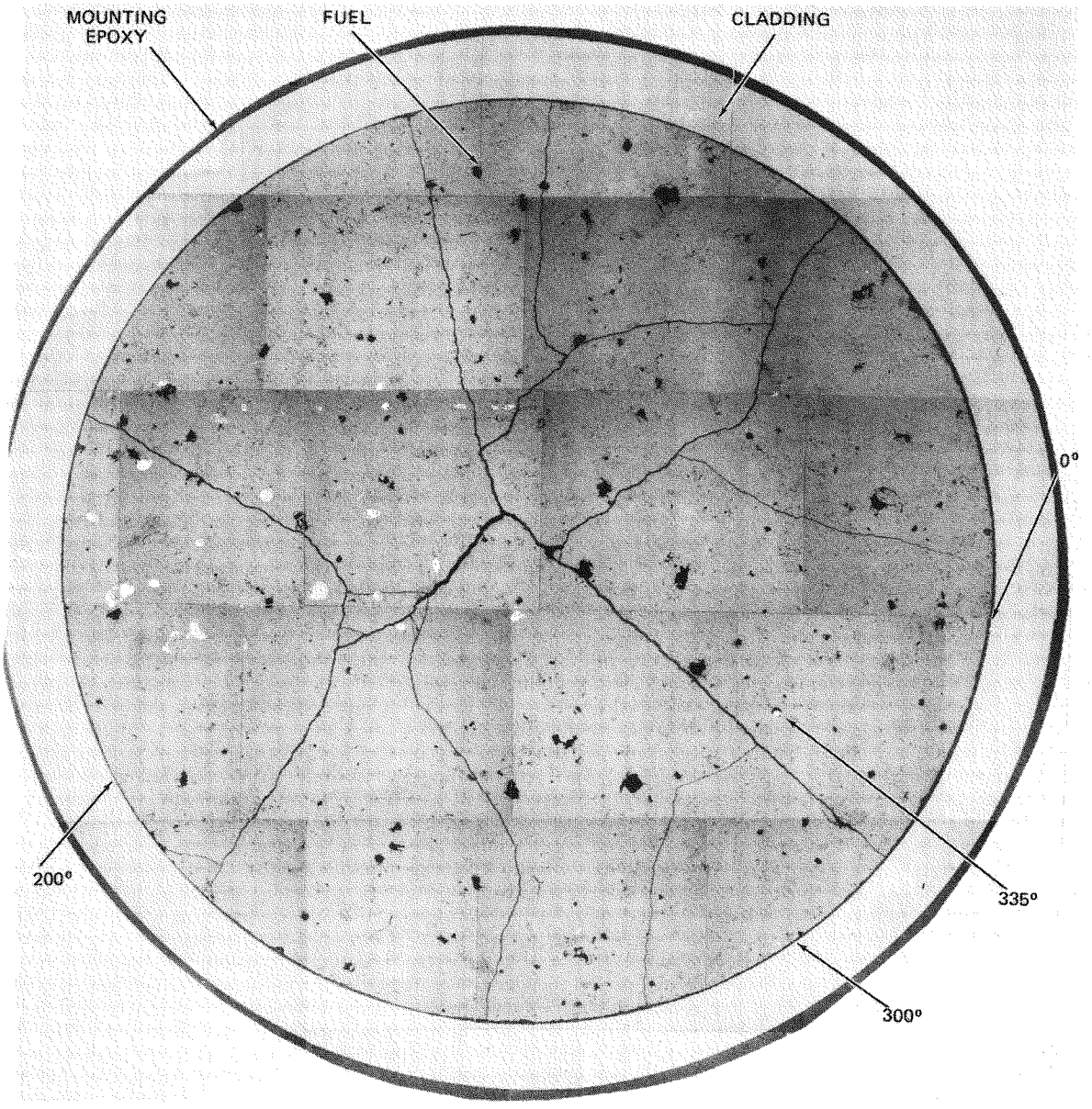

FIGURE 32. Mosaic of Sample G7-4 (16.5 in.) and Areas Examined by the Shielded Electron Microprobe. Neg 7908542-1

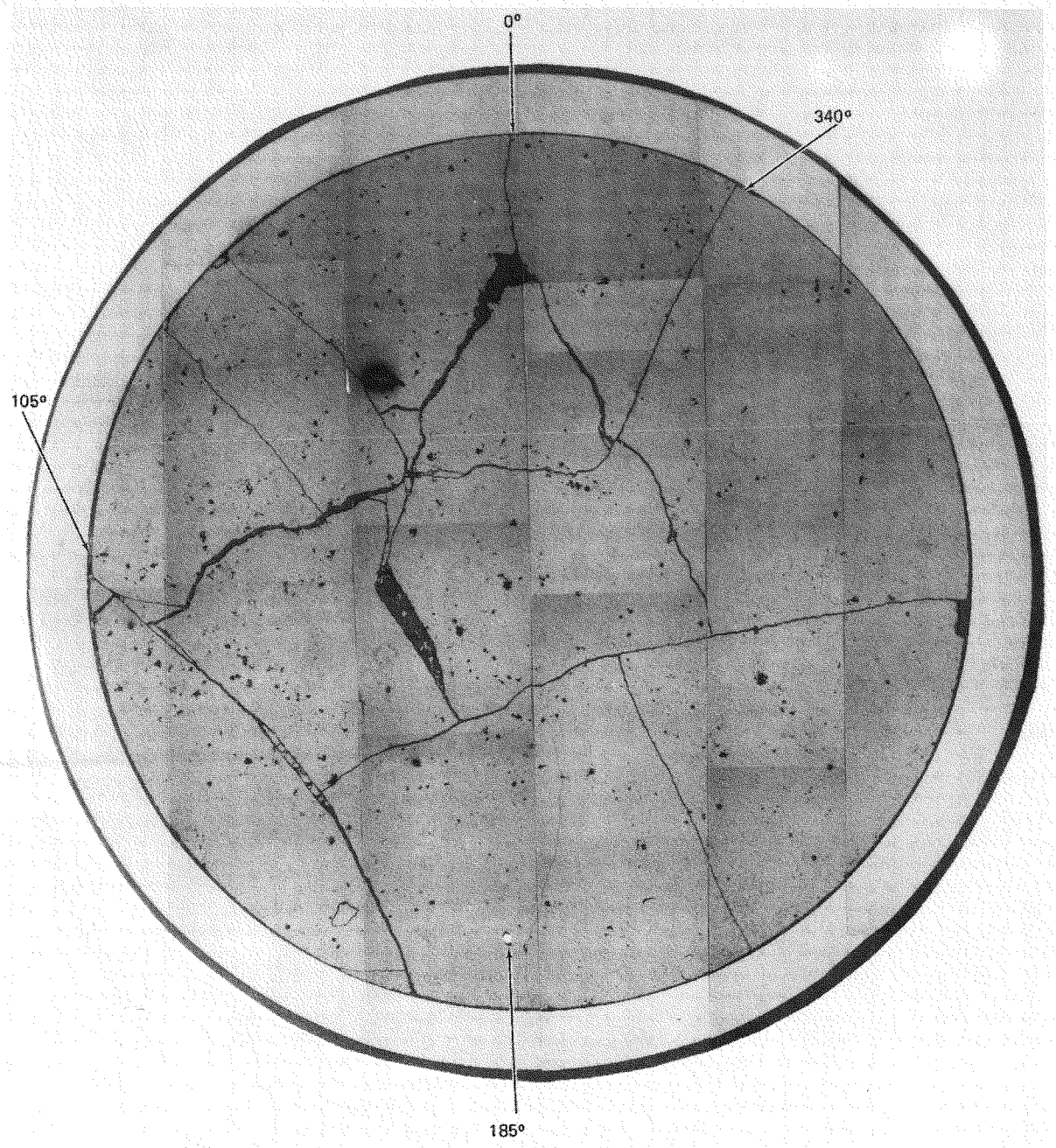

FIGURE 33. Mosaic of Sample G7-16 (91.0 in.) and Areas Examined by the Shielded Electron Microprobe.

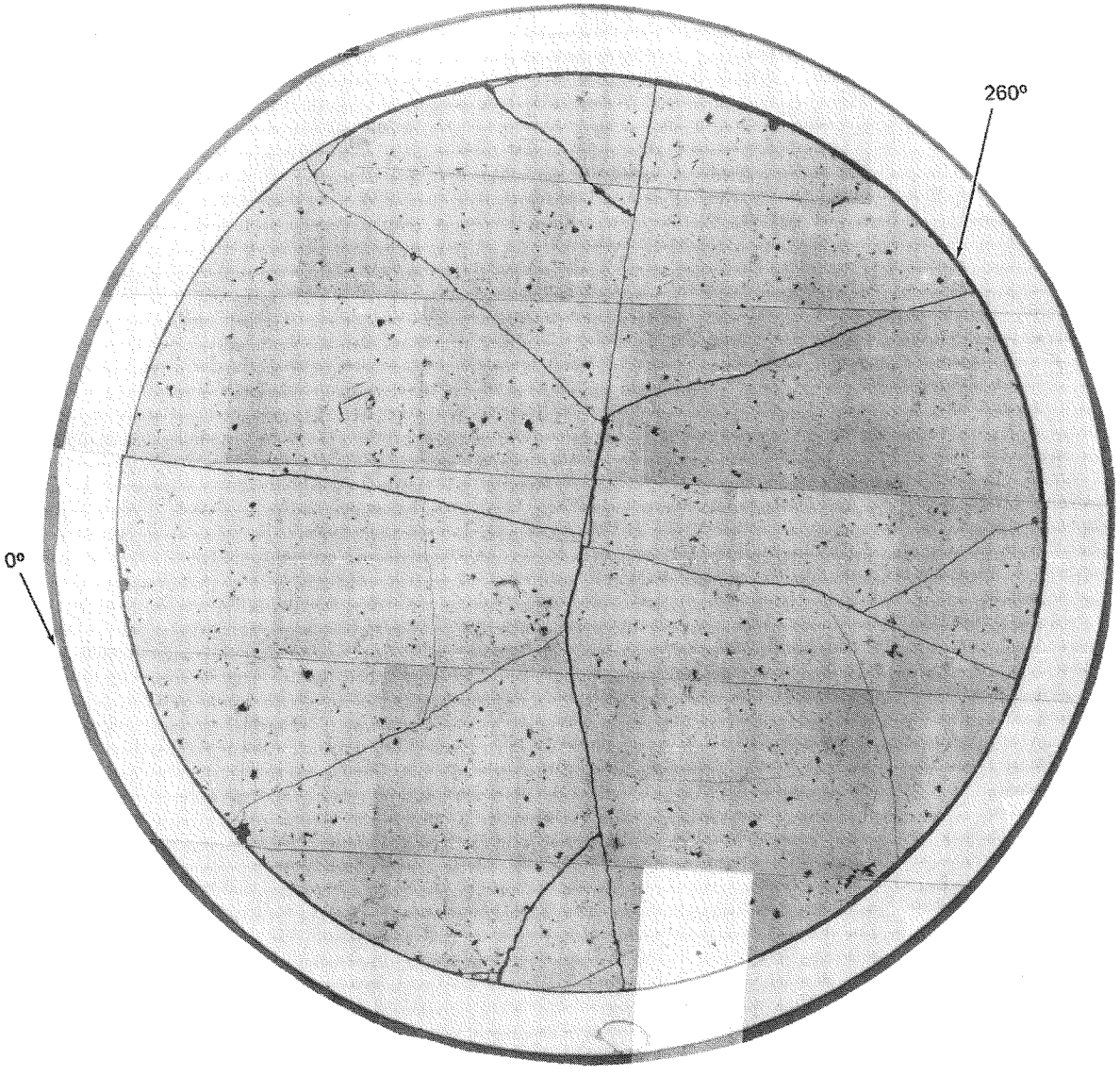

FIGURE 34. Mosaic of Sample G7-28 (115.5 in.) and Areas Examined by the Shielded Electron Microprobe.

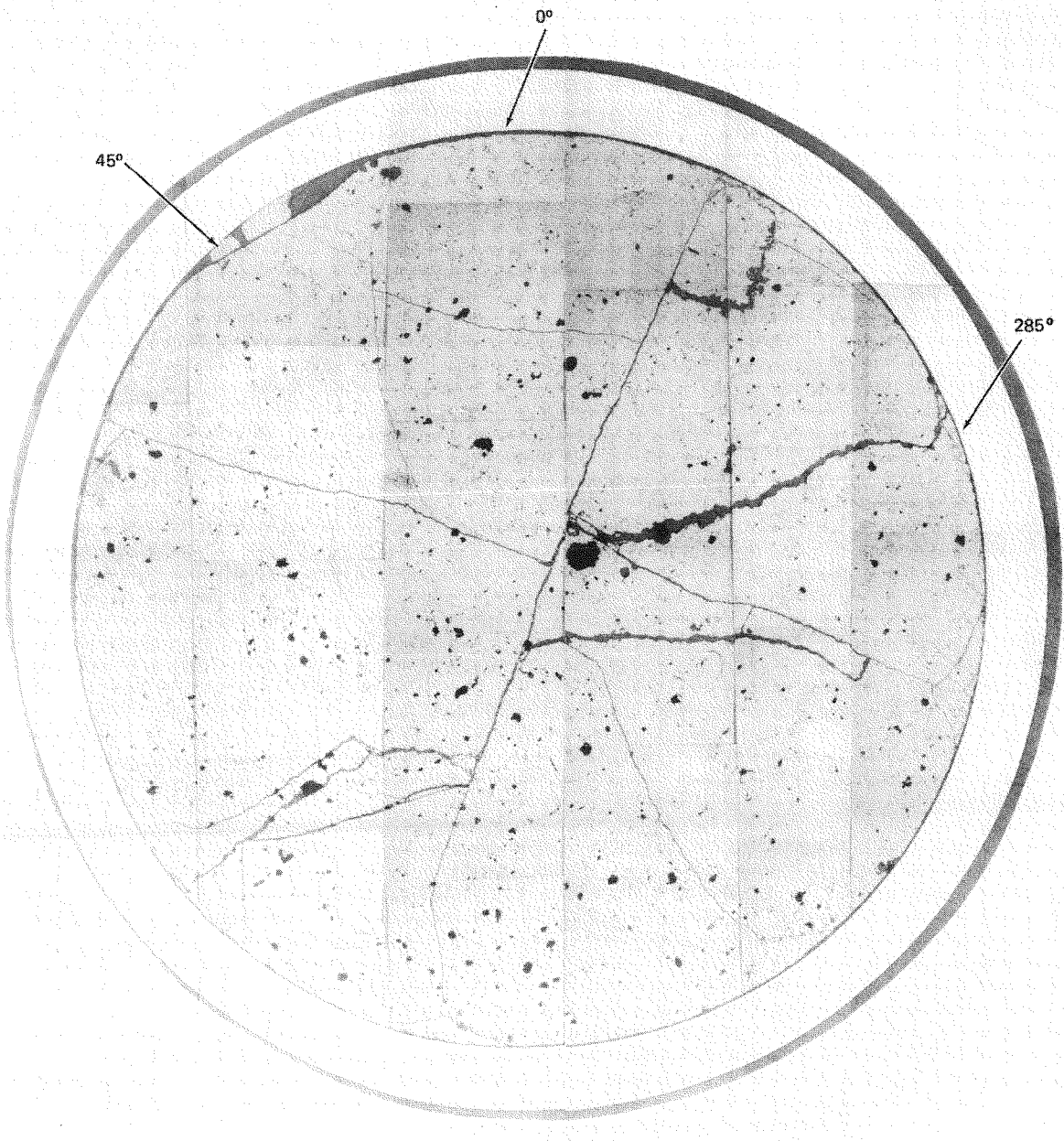

FIGURE 35. Mosaic of Sample G9-22 (91.0 in.) and Areas Examined by the Shielded Electron Microprobe.

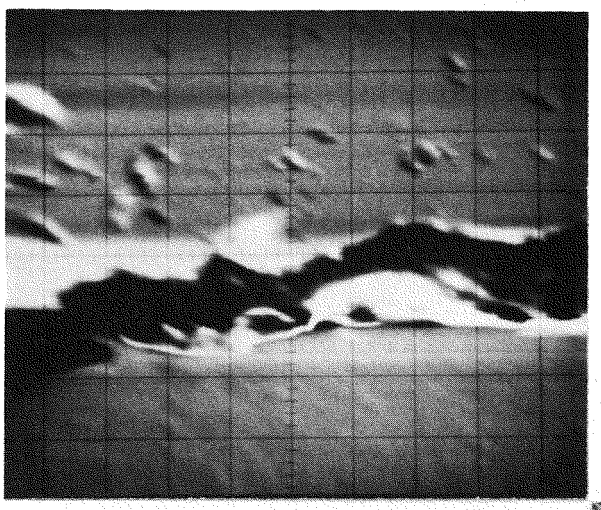

FUEL

GAP

CLADDING

EBS IMAGE

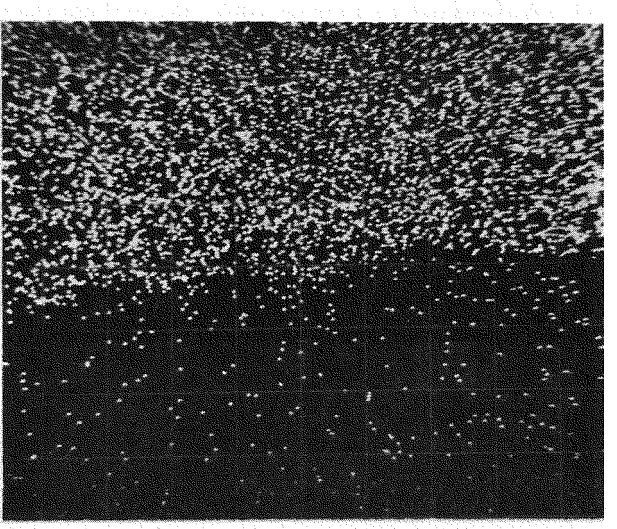

U X-RAY IMAGE 1618

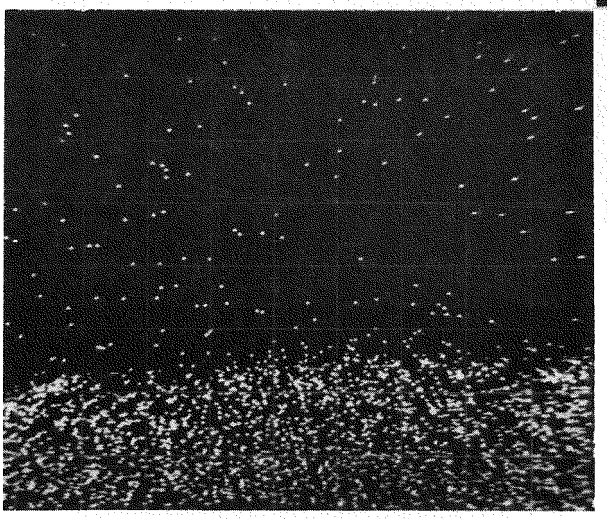

Zr X-RAY IMAGE 1617

FIGURE 36. X-ray Photomicrographs of Sample G7-4 (16.5 in.) 200X EBS, Uranium, and Zirconium Images Taken at 200° Orientation.

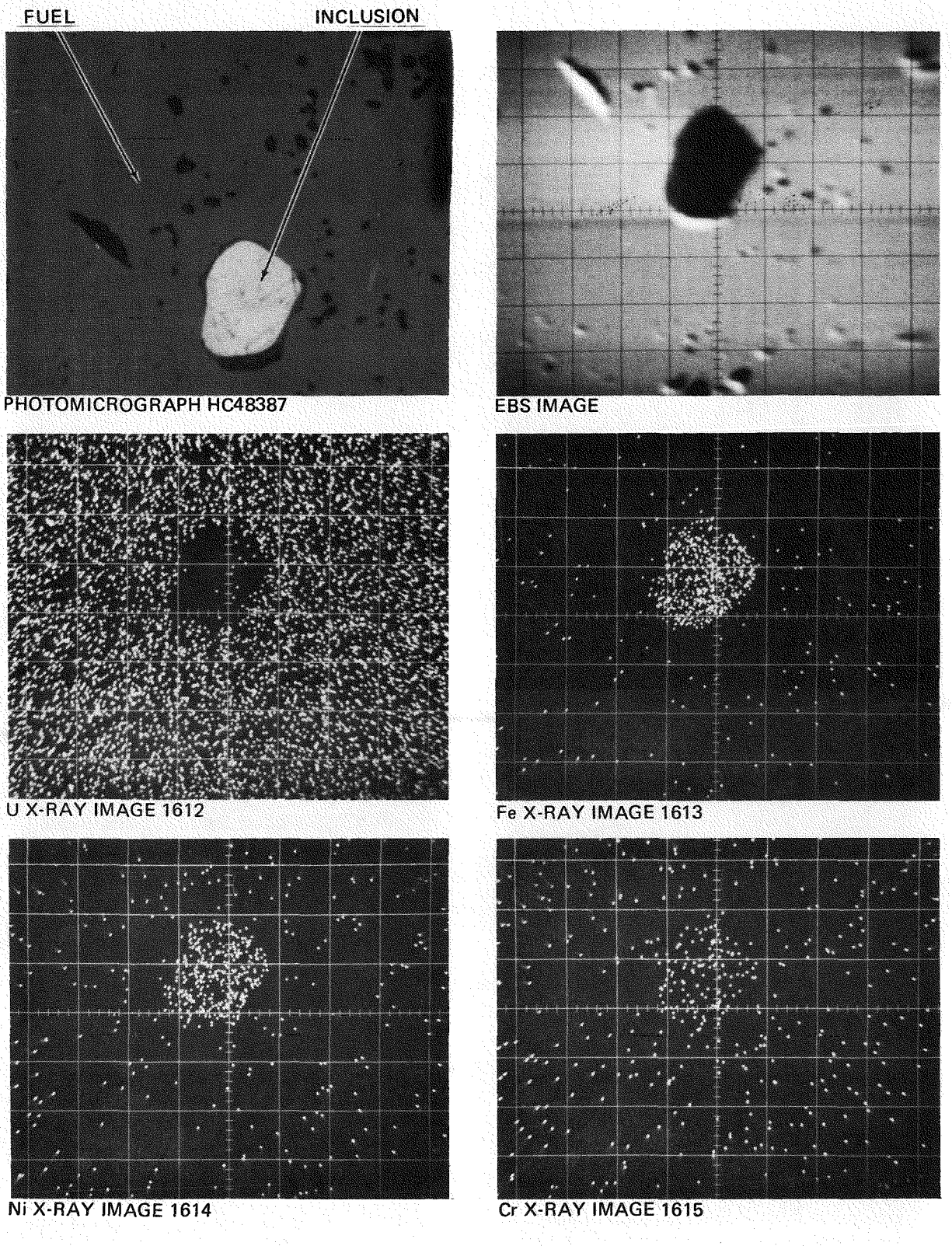

FIGURE 37. X-ray Photomicrographs of Sample G7-4 (16.5 in.) 750X Optical, EBS, Uranium, Iron, Nickel, and Chromium Images Taken at 300° Orientation.

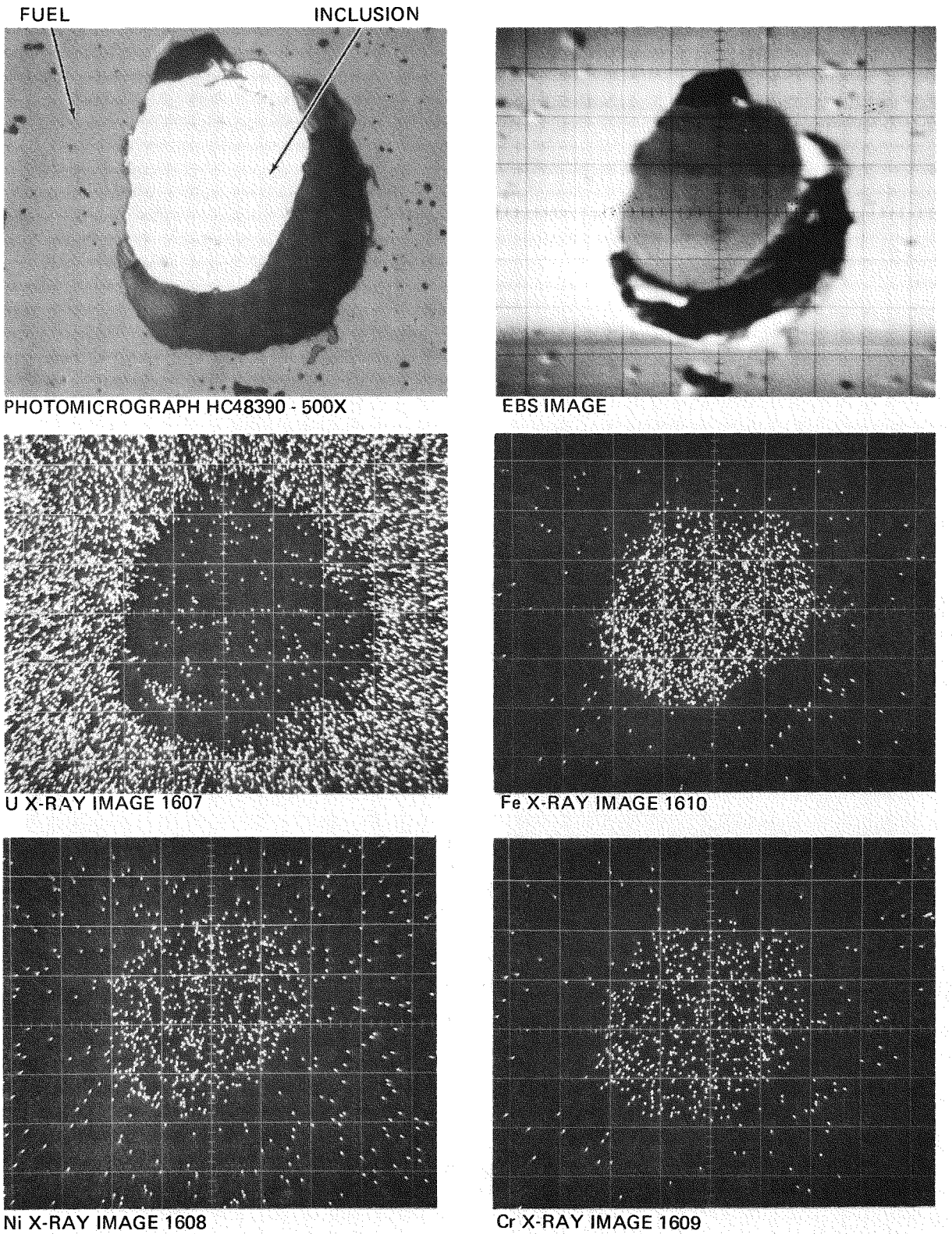

FIGURE 38. X-ray Photomicrographs of Sample G7-4 (16.5 in.) 400X Optical, EBS, Uranium, Iron, Nickel, and Chromium Images Taken at 335° Orientation.

TABLE 11

MICROPROBE WAVELENGTH SCAN RESULTS

Sample Amount	G7-4 Metallic Particle[a] (300°)	G7-4 Metallic Particle[a] (335°)	G7-16 Fuel-Clad Gap[a] (105°)	G7-16 Metallic Particle[a] (185°)	G7-16 Clad ID[a] (340°)	G9-22 Bonded Fuel[a] (45°)	G9-22 Clad ID[a] (285°)
Major (>10%)	Fe Ni Cr	Fe Cr Ni	U Zr	Fe	Zr	U Zr	Zr
Minor (2-10%)	--	U	Cr[b]	Cr[b]	--	--	U
Trace (<2%)	Si	Si	Pu Si Ce Ru	Si	Cr[b] Sn	Sn Pu Cs	Sn Cr[b]

[a] Elements listed in order of decreasing intensity.

[b] Probable contamination from CrO_3 polish.

TABLE 12

SEMIQUANTITATIVE ANALYSIS[a] OF
SAMPLE G7-4 (16.5 in.) METALLIC PARTICLE AT 335° ORIENTATION

	Counts Per 10 Seconds						
	Sample			Standard			
Element	Gross	Bkg	Net	Gross	Bkg	Net	wt%
Fe	24,421	241	24,180	41,213	213	41,000	59.0
Cr	3,869	63	3,807	44,312	164	44,149	8.6[b]
Ni	3,530	132	3,398	27,273	133	27,140	12.5
						Total	80.1
						O_2 (Difference)	19.9[c]

[a] First approximation basis with no absorption, atomic number, or fluorescence corrections.

[b] Possibility of slight contamination with CrO_3 polishing compound.

[c] For comparison, Fe_2O_3 = 30.0% O_2 and UO_2 = 11.9% O_2.

2. Sample G7-16 (91.0 in.)

Three areas were examined: a metallic particle at 185°, the fuel-cladding gap region containing fuel particles, and cladding inner surface oxide layer as outlined in Table 10 and shown in Figure 33. Results of wavelength scans are shown in Table 11.

The metallic particle was essentially all iron in contrast to the stainless-steel-type impurities found in G7-4 (16.5 in.). Minor amounts of chromium and silicon, believed to be introduced during sample preparation with SiC and CrO_3, were detected. Figure 39 shows the optical, electron backscatter (EBS), uranium, and iron images.

The fuel-cladding gap area at 105° showed fuel particles in the 50-μm gap, In addition to uranium and zirconium, trace amounts of plutonium, cerium, and ruthenium were detected in the gap. Wavelength results and x-ray images are shown in Table 11 and Figure 40, respectively.

A reaction product layer on the cladding inner surface opposite a pellet crack at 340° was analyzed. A wavelength scan revealed zirconium and tin with some chromium contamination from the CrO_3 used during polishing. X-ray images and the corresponding backscatter image and photomicrograph are shown in Figure 41.

3. Sample G7-28 (115.5 in.)

Extensive x-ray imaging was performed in the bonded fuel area at 260° shown in Figures 42 and 43, which show the uranium, zirconium, cerium, tin, cesium, ruthenium, molybdenum, and plutonium x-ray images. High-beam currents (0.4 μa) were utilized in an attempt to locate fission products. Trace amounts of cerium, cesium, ruthenium, and molybdenum (believed to be in the 0.1-0.2% concentration range) are shown in the fuel region. Plutonium in the fuel and tin in the Zircaloy cladding are also shown. Horizontal and vertical uranium and zirconium line profiles superimposed on the EBS image are shown in Figure 44. The peaks are representative of the uranium and zirconium concentrations in the bonded region.

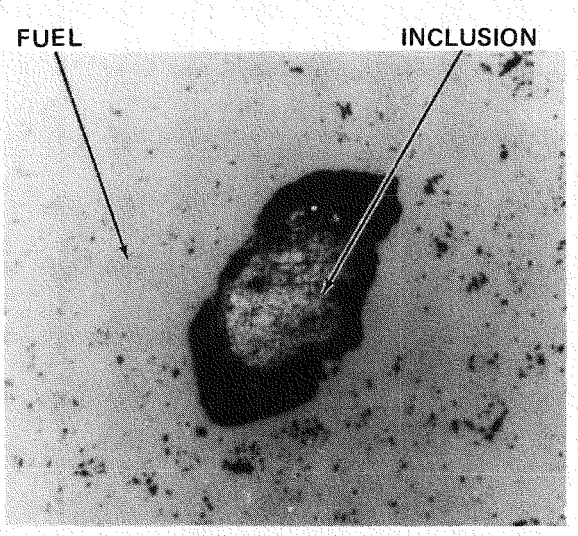

PHOTOMICROGRAPH HC48329

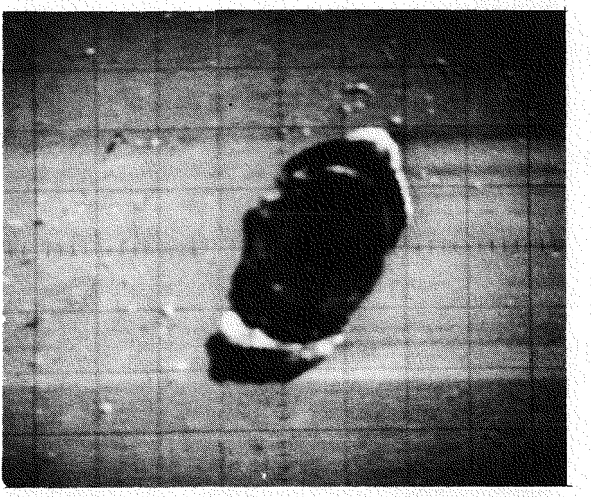

EBS IMAGE

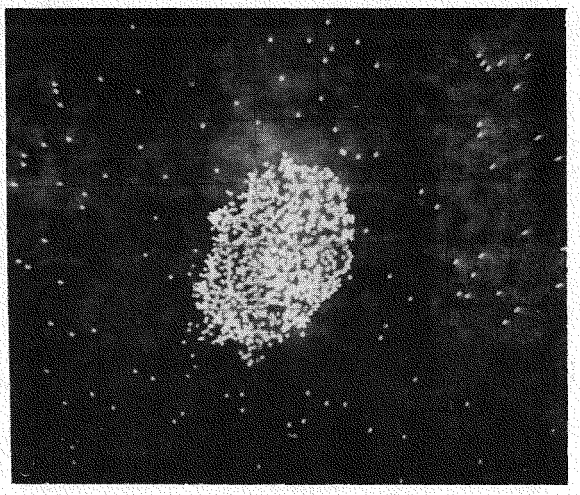

U X-RAY IMAGE 1596

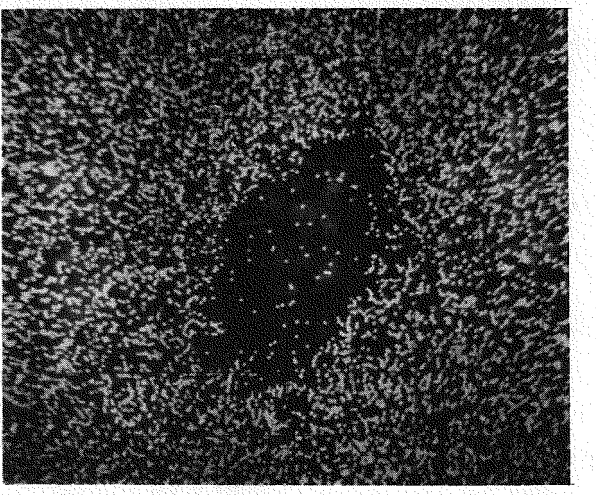

Fe X-RAY IMAGE 1595

FIGURE 39. X-ray Photomicrographs of Sample G7-16 (91.0 in.) 200X Optical, EBS, Uranium, and Iron Images Taken at 185° Orientation.

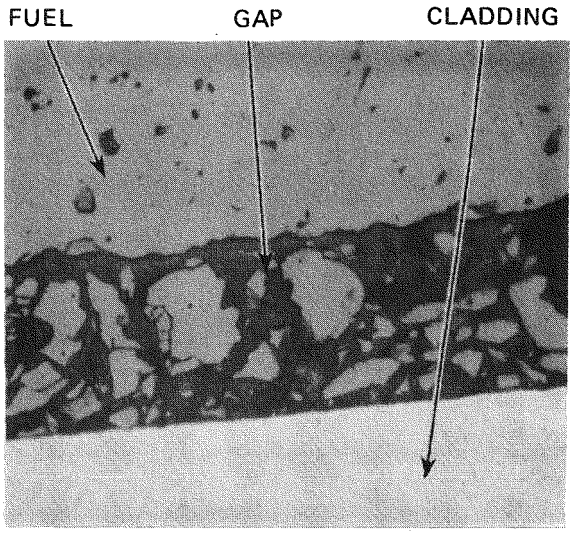

PHOTOMICROGRAPH HC48344

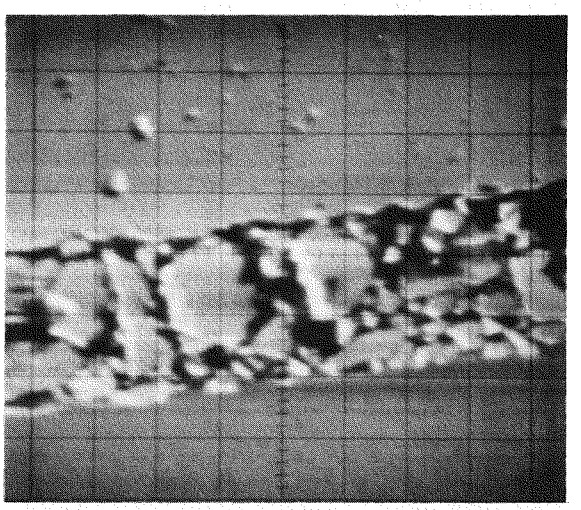

EBS IMAGE

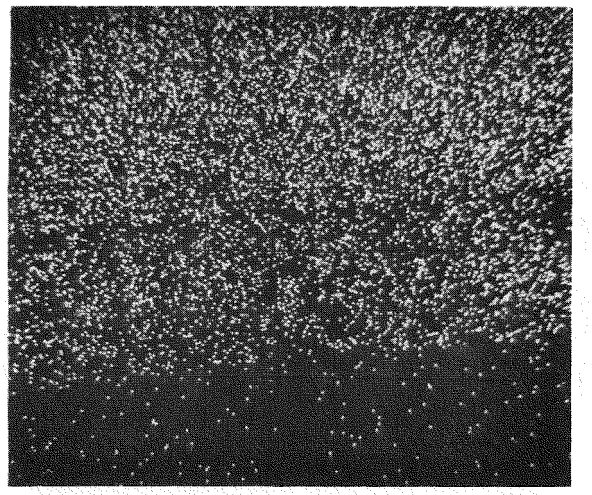

U X-RAY IMAGE 1601

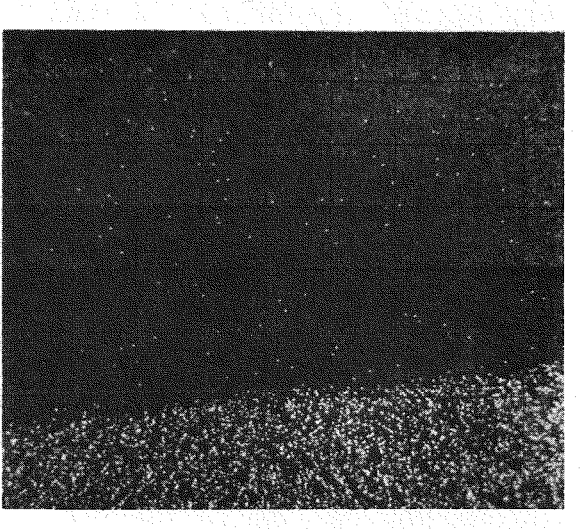

Zr X-RAY IMAGE 1600

FIGURE 40. X-ray Photomicrographs of Sample G7-16 (91.0 in.) 500X Optical, EBS, Uranium, and Zirconium Images Taken at 105° Orientation.

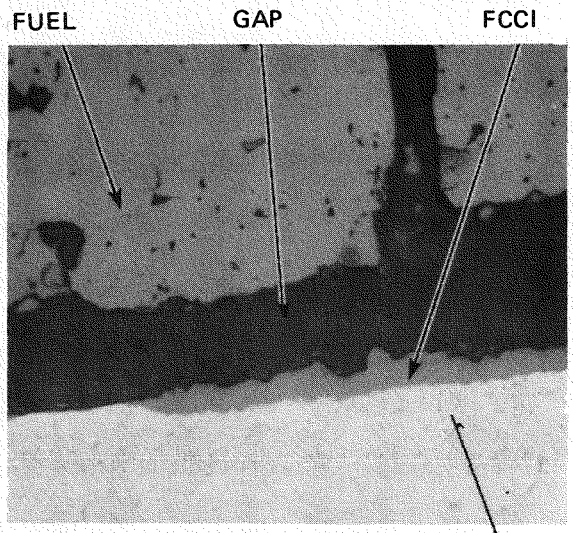

PHOTOMICROGRAPH HC48342

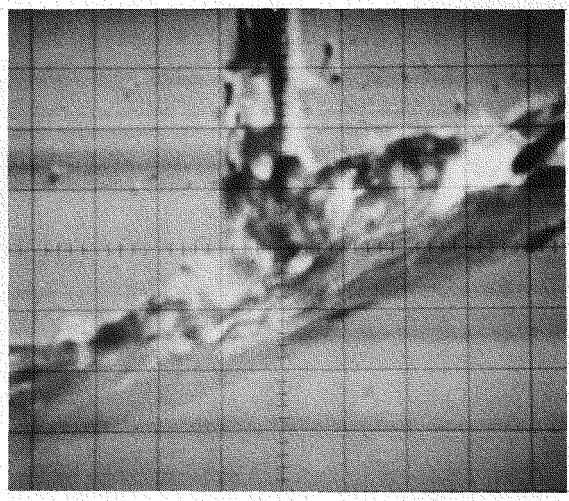

EBS IMAGE

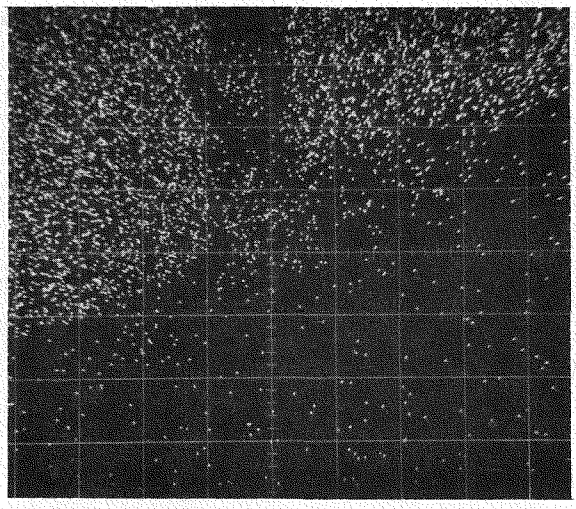

U X-RAY IMAGE 1605

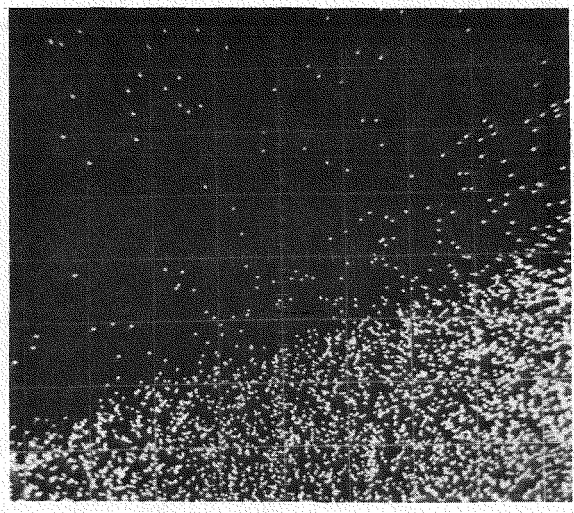

Zr X-RAY IMAGE 1604

FIGURE 41. X-ray Photomicrographs of Sample G7-16 (91.0 in.) 500X Optical, EBS, Uranium, and Zirconium Images Taken at 340° Orientation.

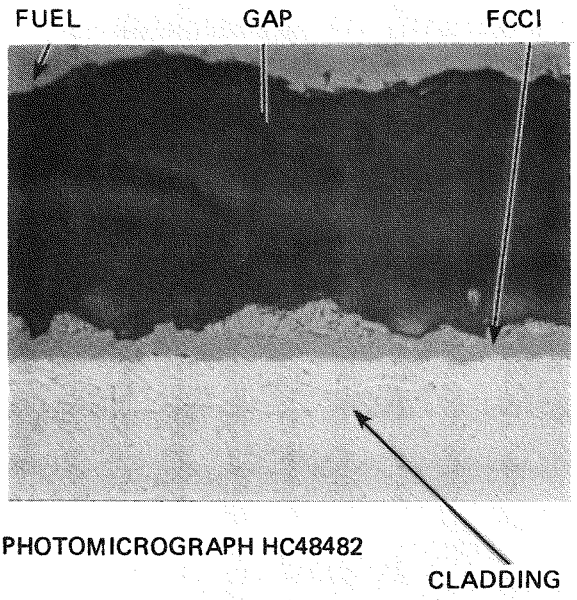

PHOTOMICROGRAPH HC48482

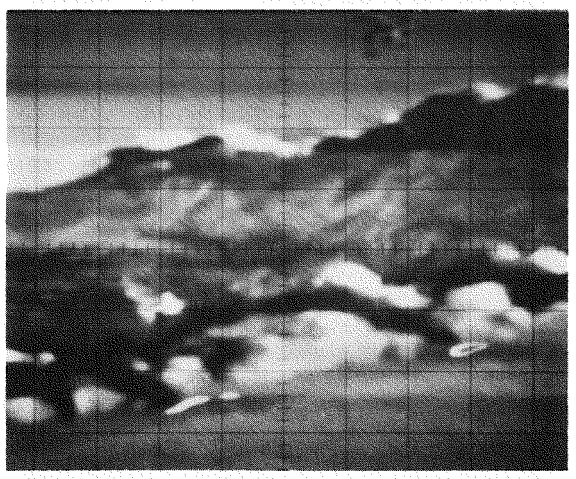

EBS IMAGE

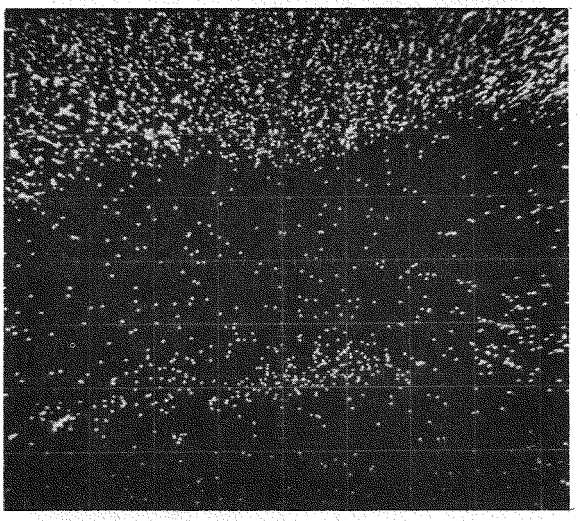

U X-RAY IMAGE 1633

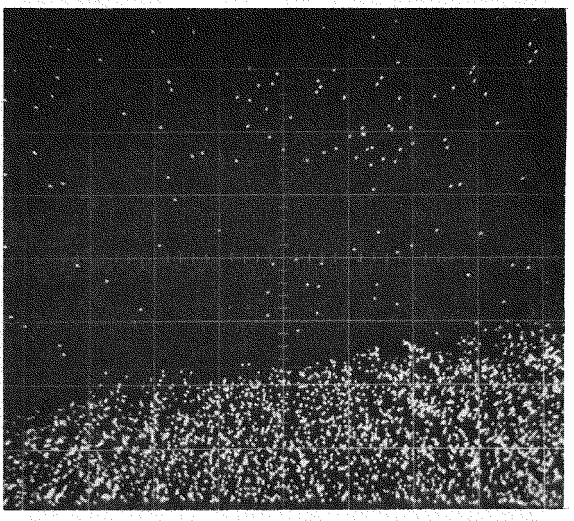

Zr X-RAY IMAGE 1634

FIGURE 42. X-ray Photomicrographs of Sample G7-28 (115.5 in.) 500X Optical, EBS, Uranium, and Zirconium Images Taken at 260° Orientation.

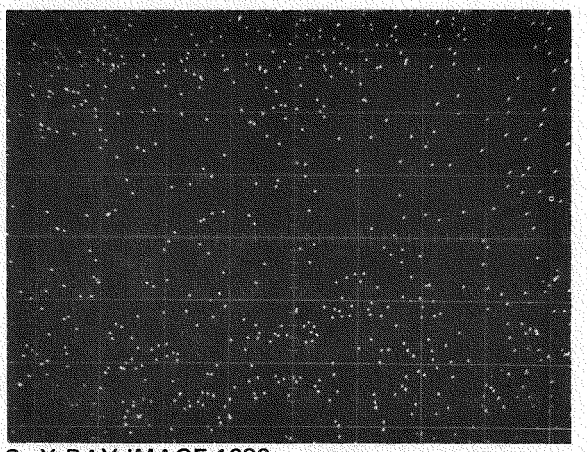

Ce X-RAY IMAGE 1636

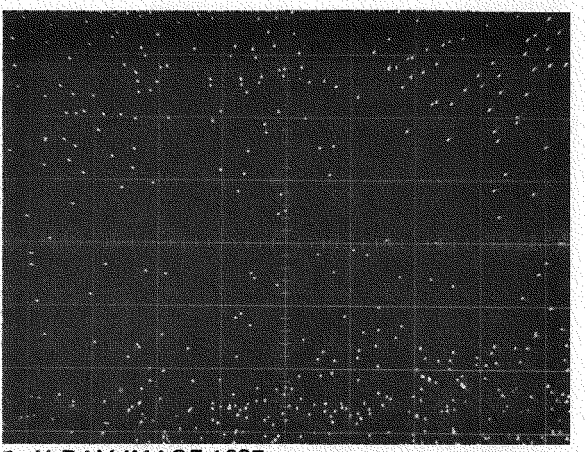

Sn X-RAY IMAGE 1637

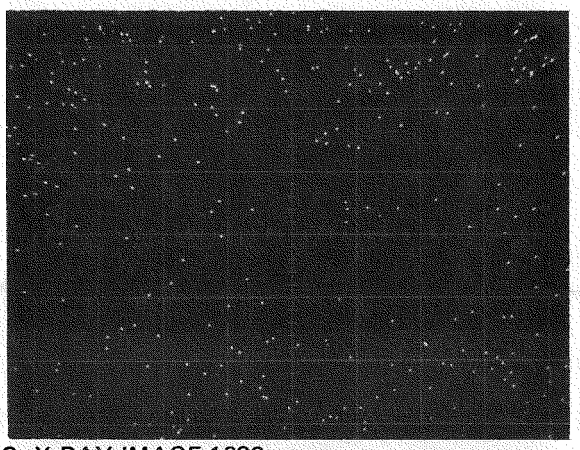

Cs X-RAY IMAGE 1638

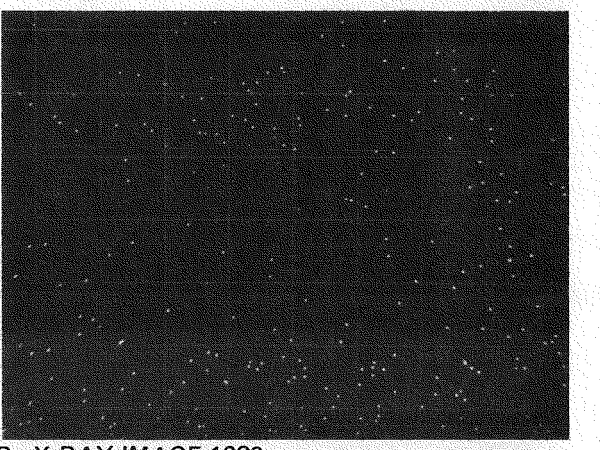

Ru X-RAY IMAGE 1639

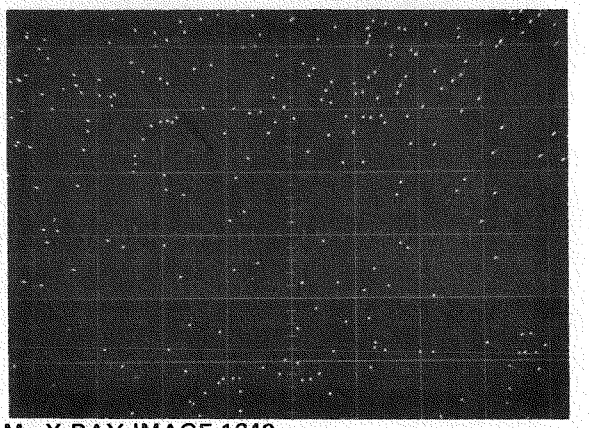

Mo X-RAY IMAGE 1640

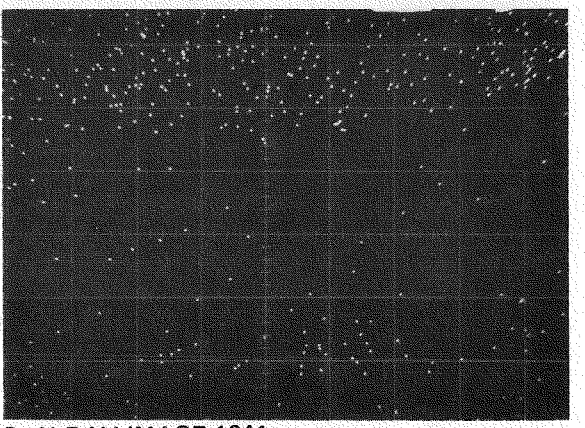

Pu X-RAY IMAGE 1641

FIGURE 43. X-ray Photomicrographs of Sample G7-28 (115.5 in.) 500X Cerium, Tin, Cesium, Ruthenium, Molydenum, and Plutonium Images Taken at 260° Orientation.

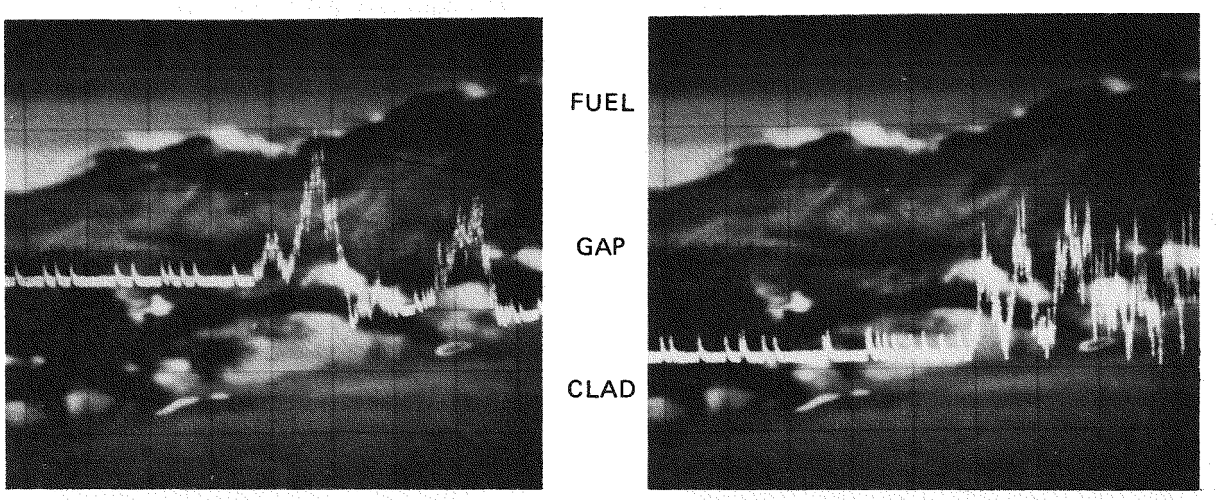

U LINE PROFILE 1643

Zr LINE PROFILE 1642

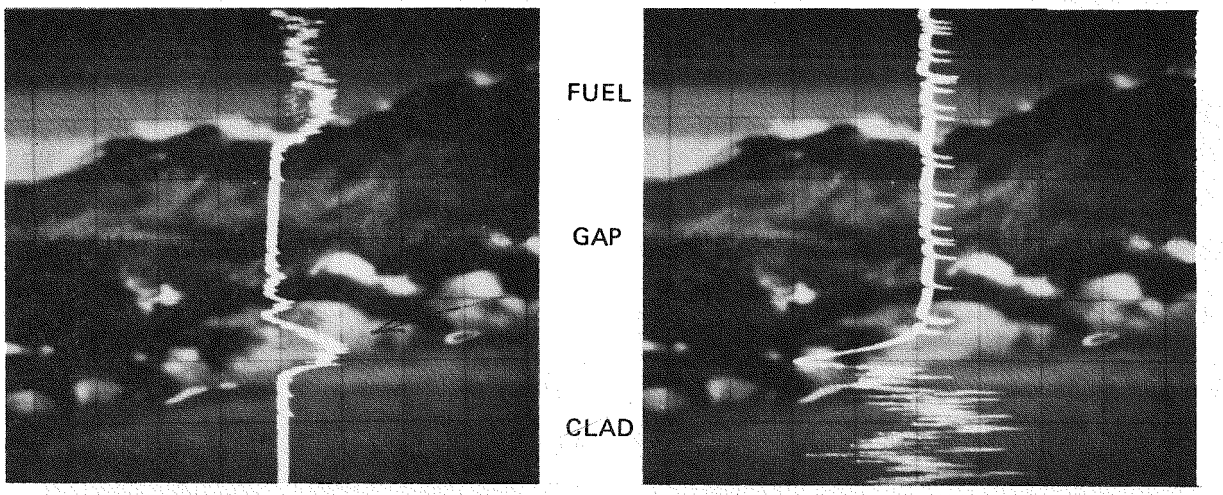

U LINE PROFILE 1644

Zr LINE PROFILE 1645

FIGURE 44. Line Profile Photomicrographs of Sample G7-28 (115.5 in.) 500X Concentration Profiles of Uranium and Zirconium Taken at 260° Orientation.

4. Sample G9-22 (91.0 in.)

The bonded fuel region at 45° was analyzed by wavelength scans, x-ray imaging, and automated step counting at 2-μm intervals. As shown in Table 11, uranium, zirconium and trace tin, plutonium, and cesium were detected. X-ray images of these elements are shown in Figures 45 and 46. Tin is present in Zircaloy at approximately 1.5% and is shown to follow the zirconium image. The cesium concentration intensity is about twice the background level.

Results of the cladding oxide analysis at 285° by wavelength and x-ray imaging are presented in Table 11 and Figure 47, respectively. Typical zirconium and uranium amounts with trace tin and cerium were observed.

Uranium, zirconium, and cesium were analyzed in 308 steps by a 10-second point count at each step. The relative intensities of the three elements are plotted in Figure 48. The plot shows a zirconium concentration increase approximately 8 μm into the reaction product with corresponding cesium and uranium concentrations decreasing. The plot shows a layer of cesium adjacent to the cladding inner surface.

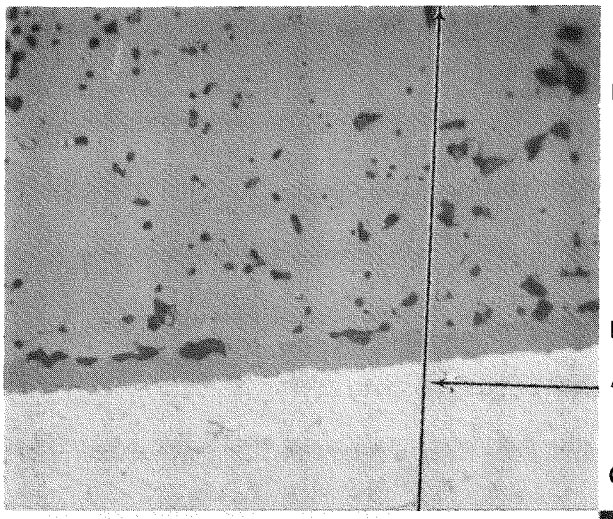

PHOTOMICROGRAPH HC48393

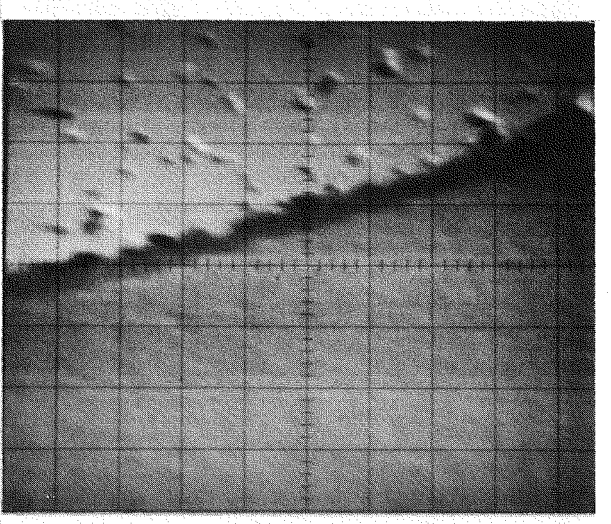

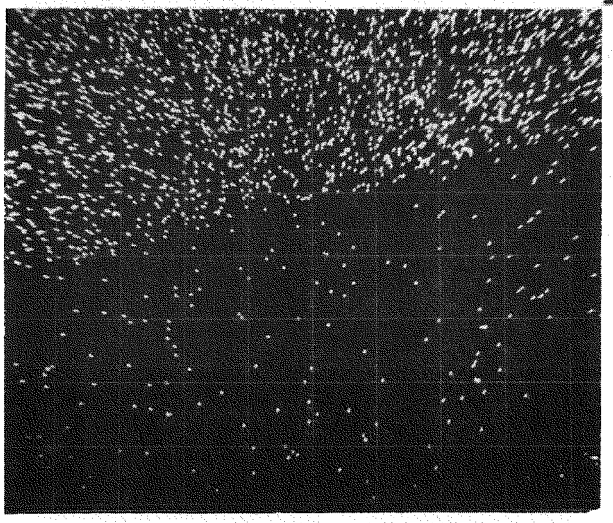

U X-RAY IMAGE 1622

FIGURE 45. Photomicrographs of Sample G9-22 (91.0 in.) 500X Optical, EBS, and Uranium Images Taken at 45° Orientation.

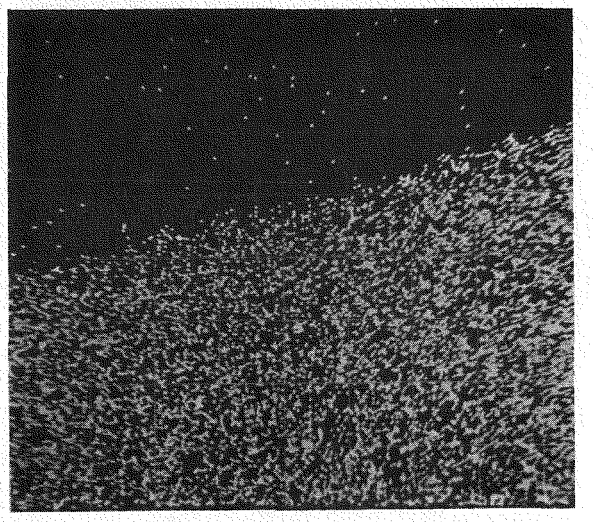

Zr X-RAY IMAGE 1620

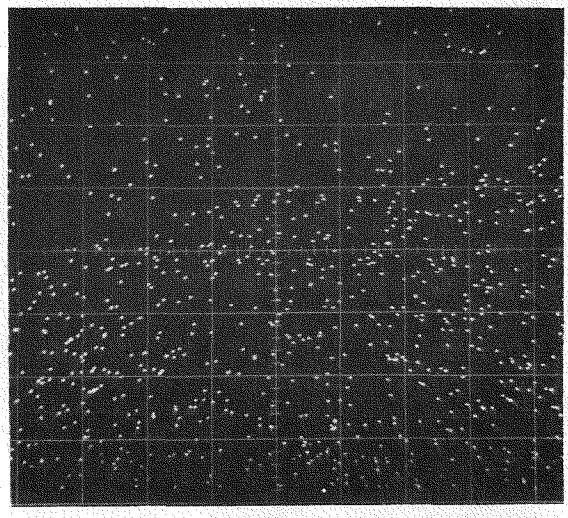

Sn X-RAY IMAGE 1625

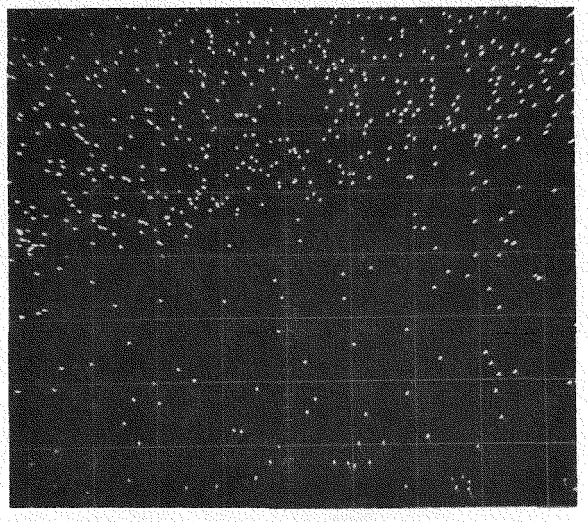

Pu X-RAY IMAGE 1624

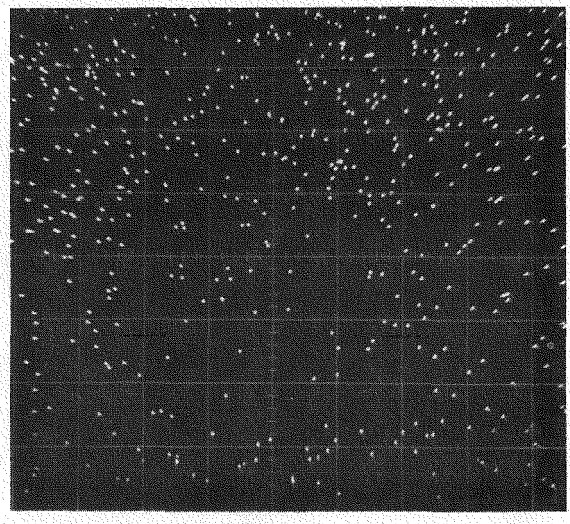

Cs X-RAY IMAGE 1625

FIGURE 46. X-ray Photomicrographs of Sample G9-22 (91.0 in.) 500X Zirconium, Tin, Plutonium, and Cesium Images Taken at 45° Orientation.

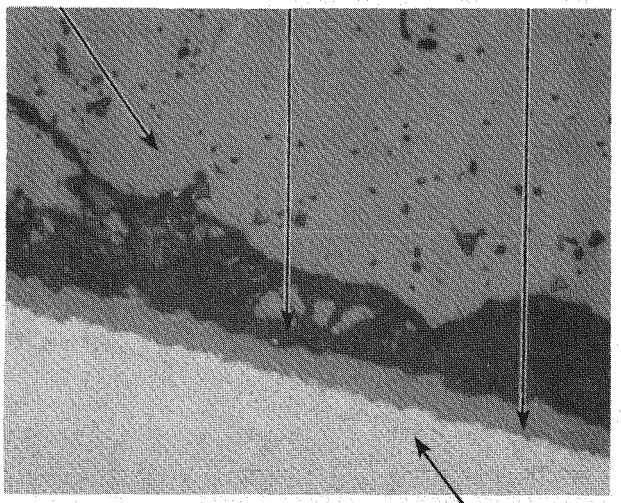

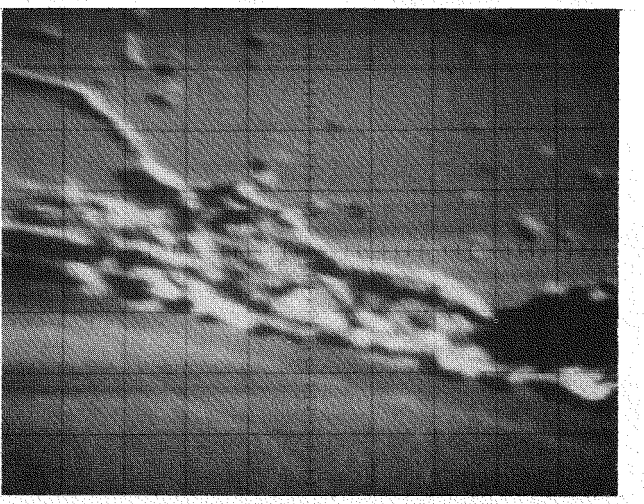

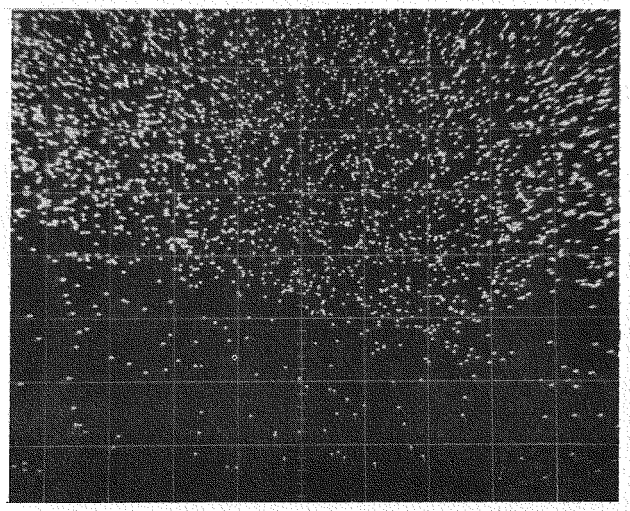

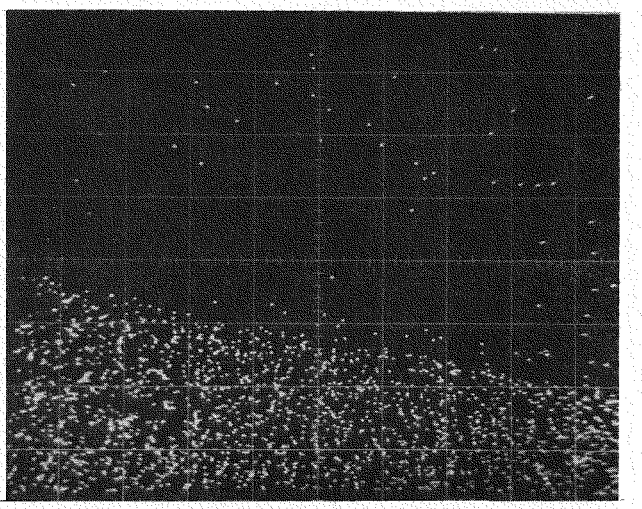

FIGURE 47. X-ray Photomicrographs of Sample G9-22 (91.0 in.) 500X Optical, EBS, Uranium, and Zirconium Images Taken at 285° Orientation.

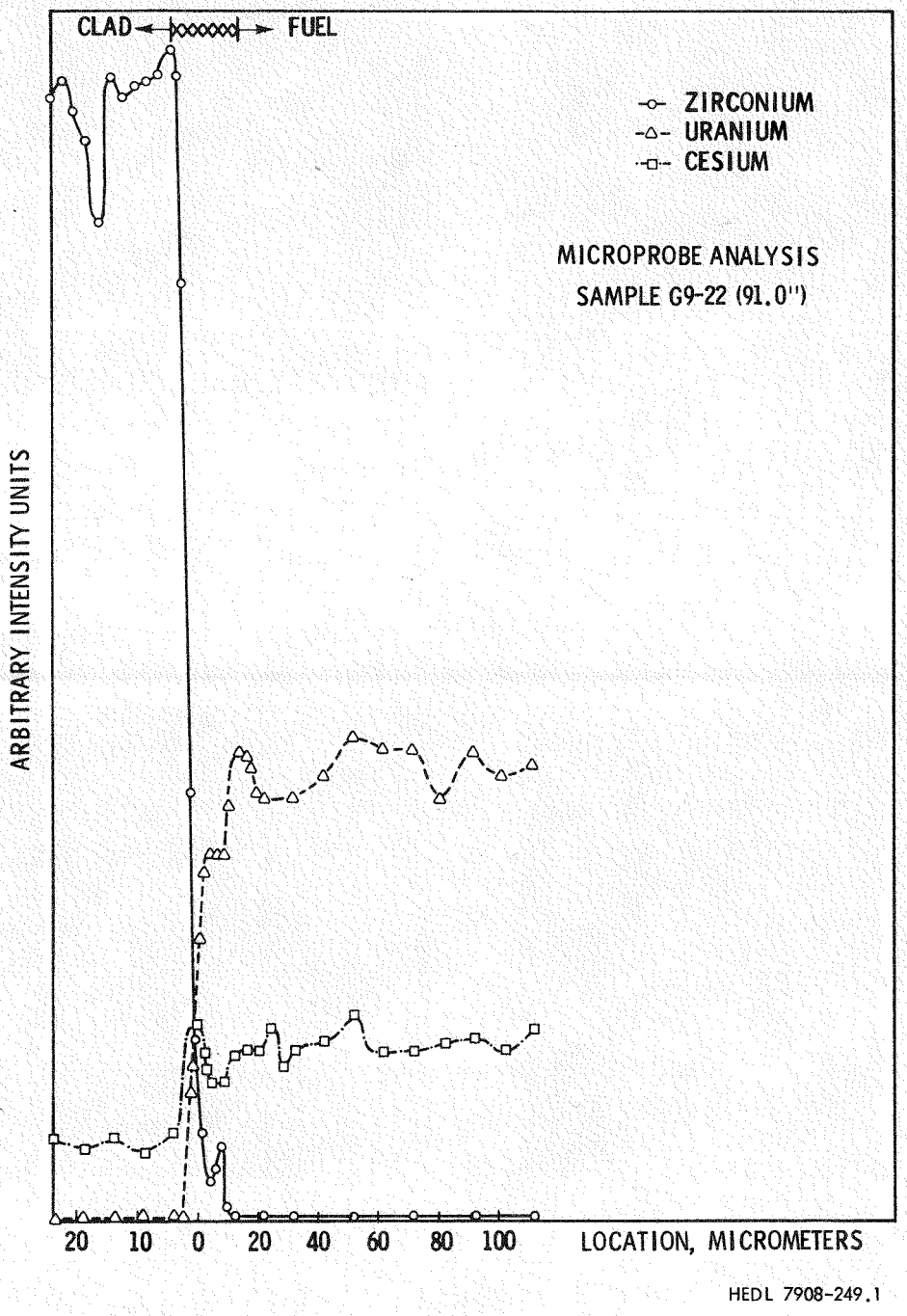

FIGURE 48. Plot of Uranium, Zirconium, and Cesium Concentrations Across Bonded Fuel Area of Sample G9-22 (91.0 in.) at 285° Orientation.

VI. REFERENCES

1. R. L. Fish, et al., Spent Fuel Characterization for the Commercial Waste and Spent Fuel Packaging Program, HEDL-TC-1384, Rev. 1, Hanford Engineering Development Laboratory, Richland, WA, March 1980.

2. R. B. Davis, Data Report for the Nondestructive Examination of Turkey Point Spent Fuel Assemblies B02, B03, B17, B41, and B43, HEDL-TME 79-68, Hanford Engineering Development Laboratory, Richland, WA, March 1978.

3. V. Pasupathi, et al., Determination and Microscopic Study of Incipient Defects in Irradiated Power Reactor Fuel Rods, EPRI NP-812, Electric Power Research Institute, Palo Alto, CA, July 1978.

A P P E N D I X A

35X MOSAICS OF FUEL ROD CROSS SECTIONS REDUCED TO 14X

FIGURES

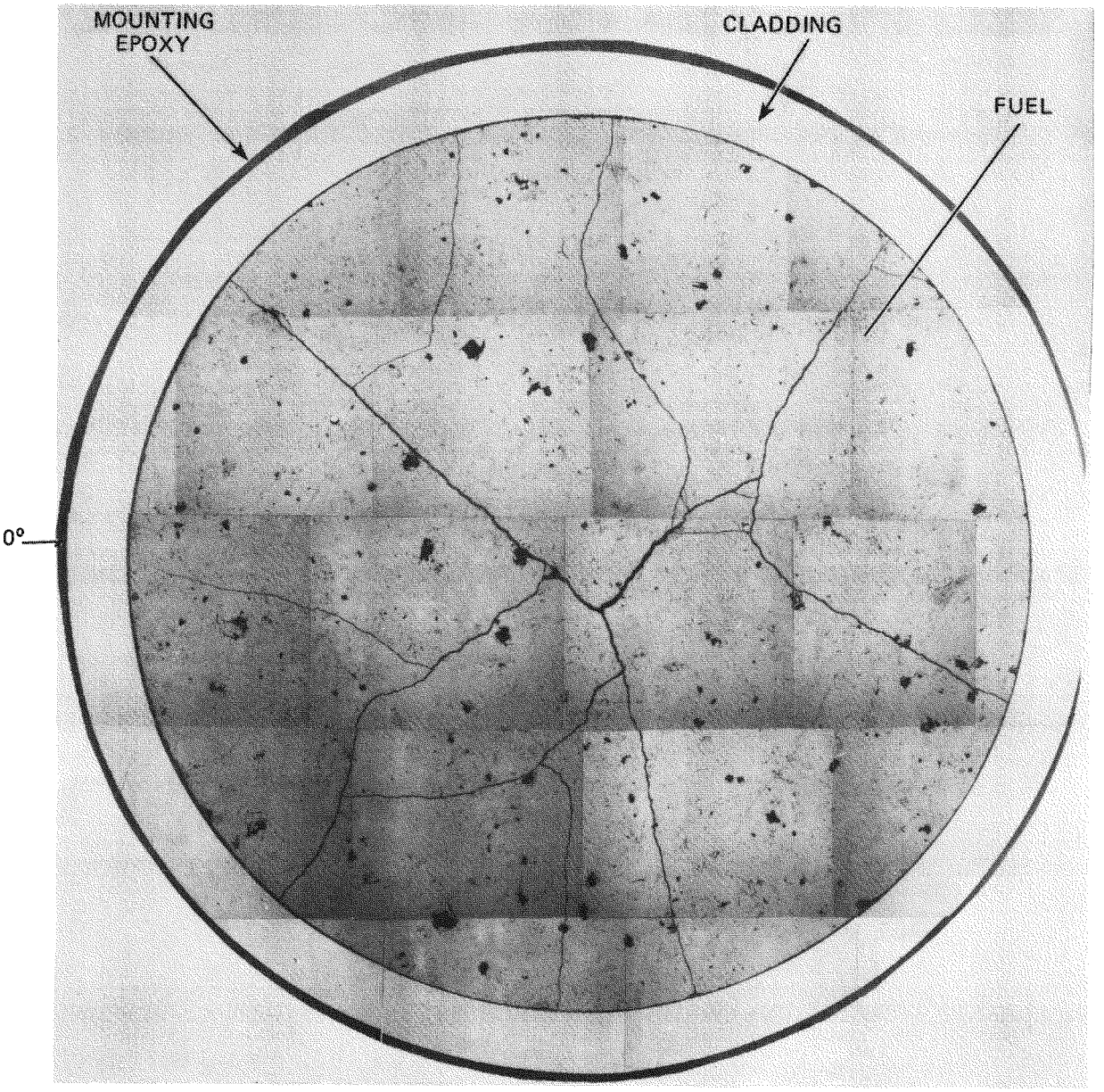

FIGURE A-1. Mosaic of Sample G7-4 (16.5 in.).

Neg 7908542-1

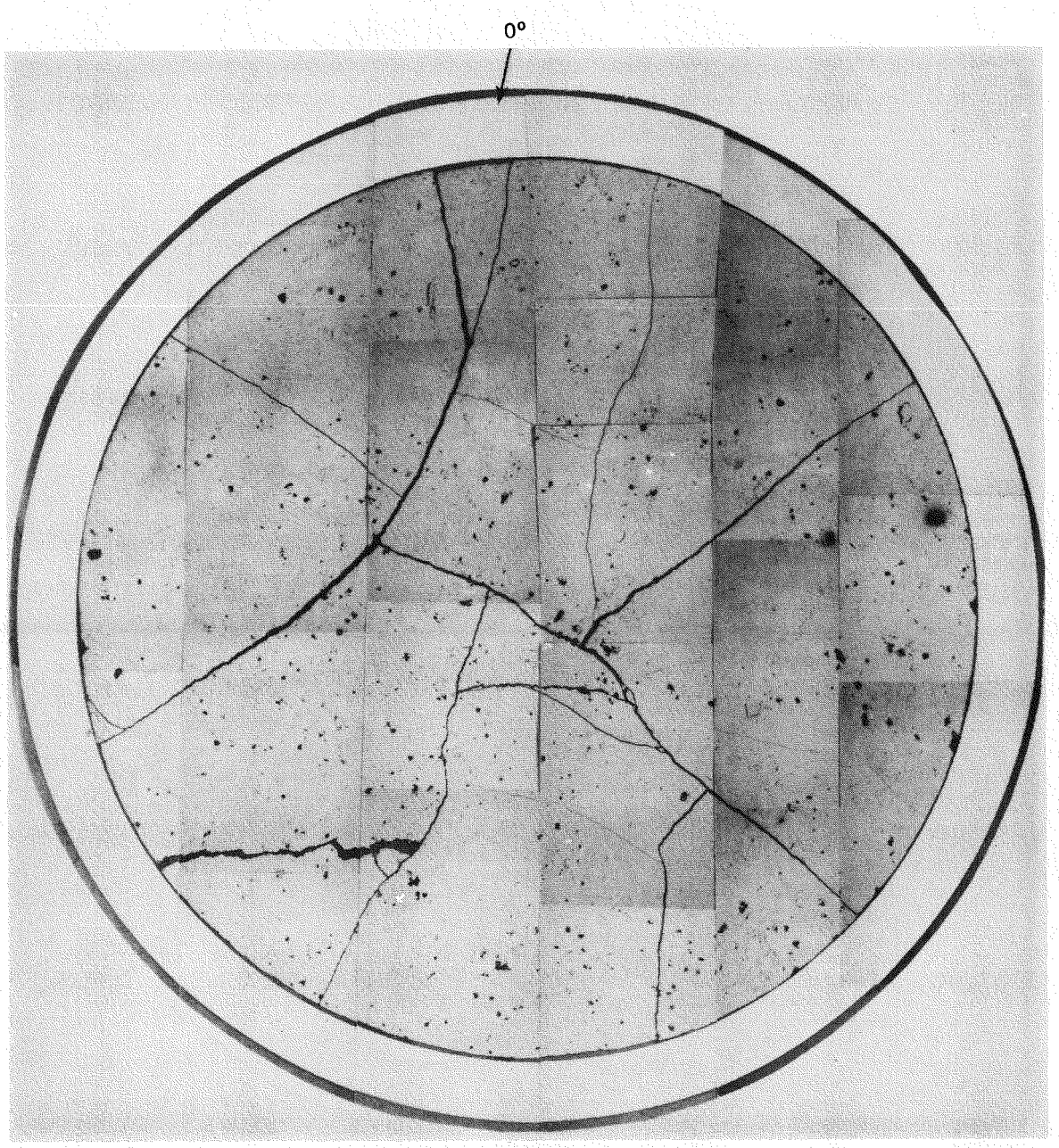

FIGURE A-2. Mosaic of Sample G7-10 (45.5 in.).

Neg 7908542-10

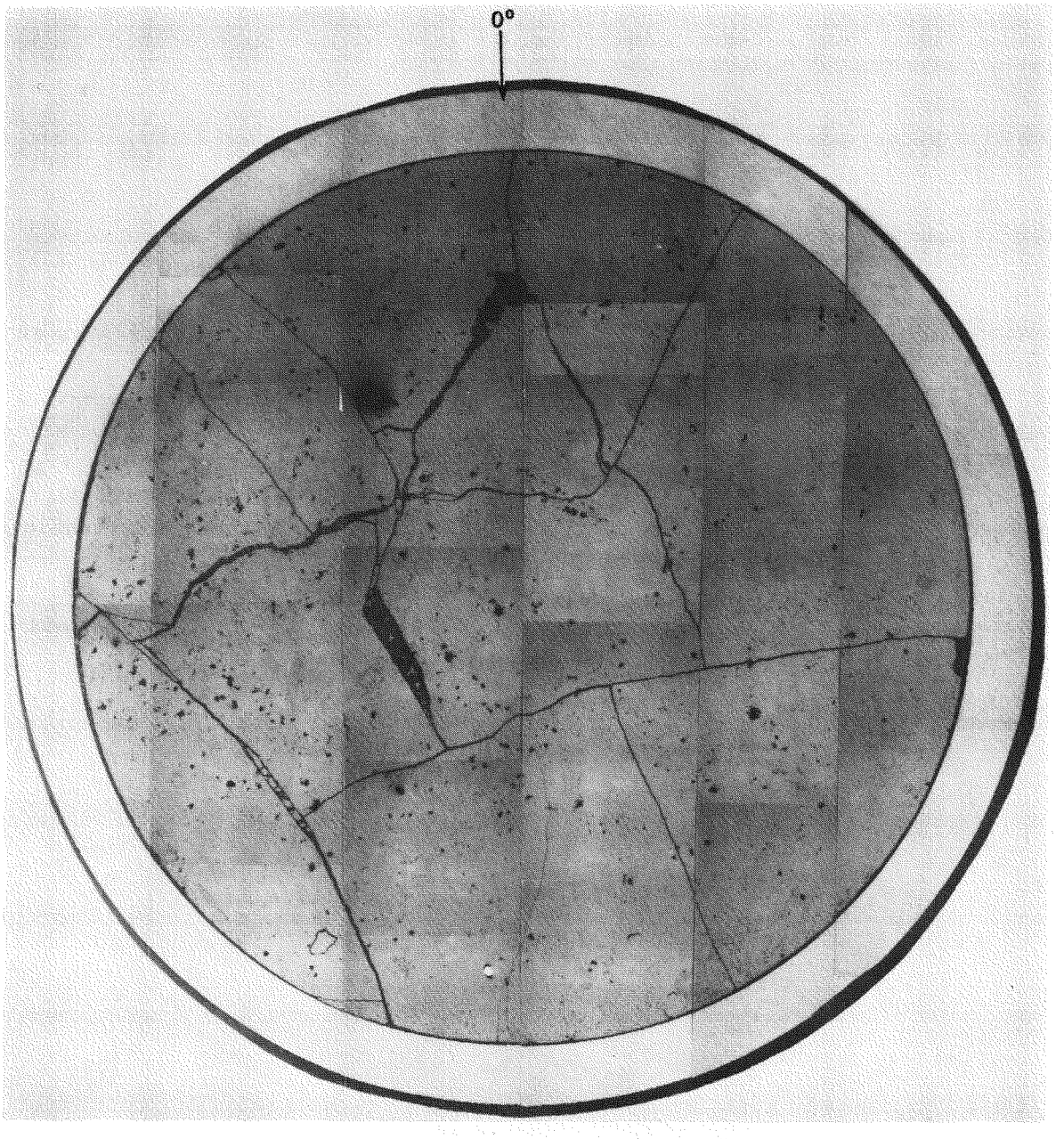

FIGURE A-3. Mosaic of Sample G7-16 (71.0 in.).

Neg 7908542-6

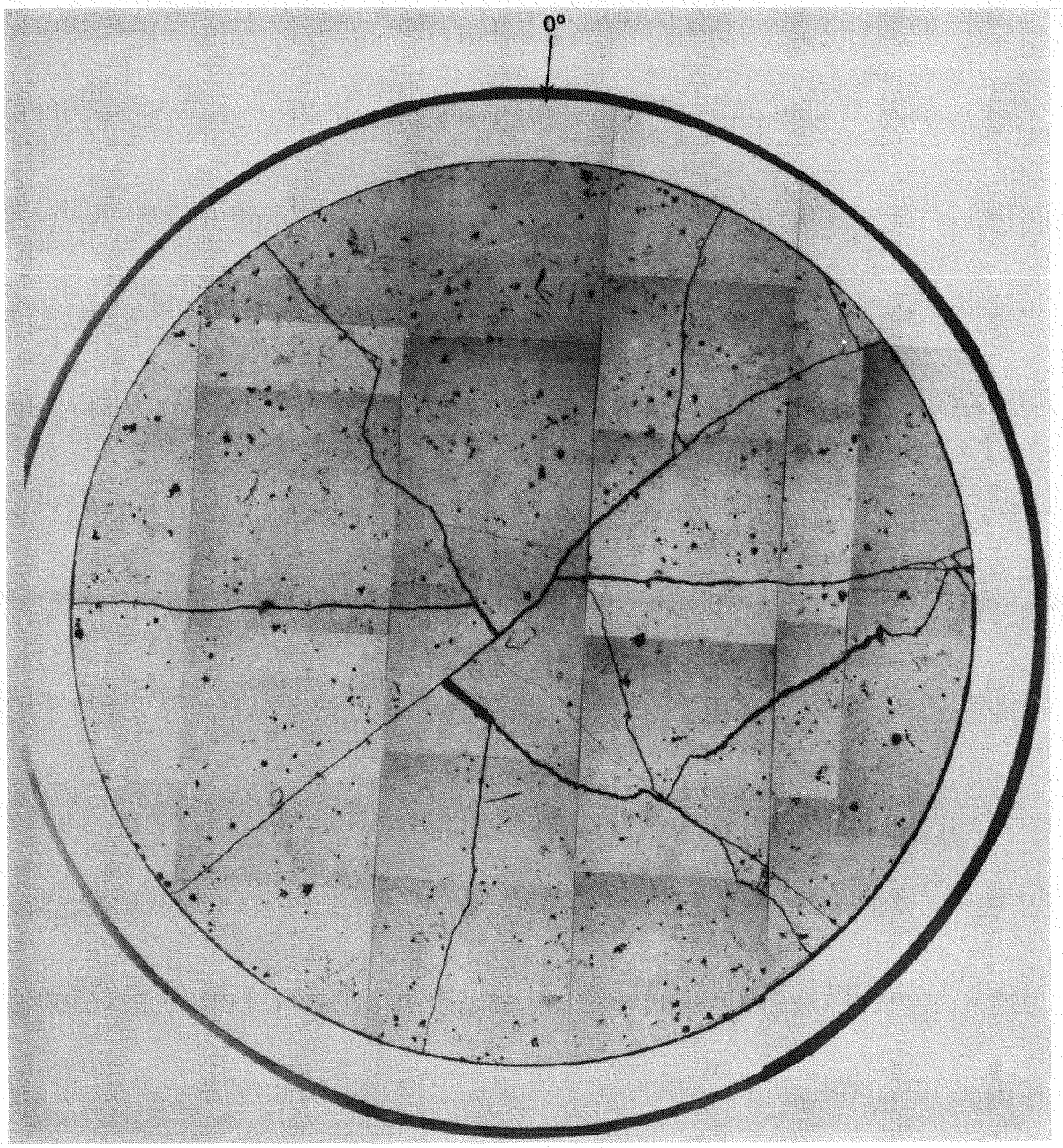

FIGURE A-4. Mosaic of Sample G7-22 (91.0 in.).

Neg 7908542-7

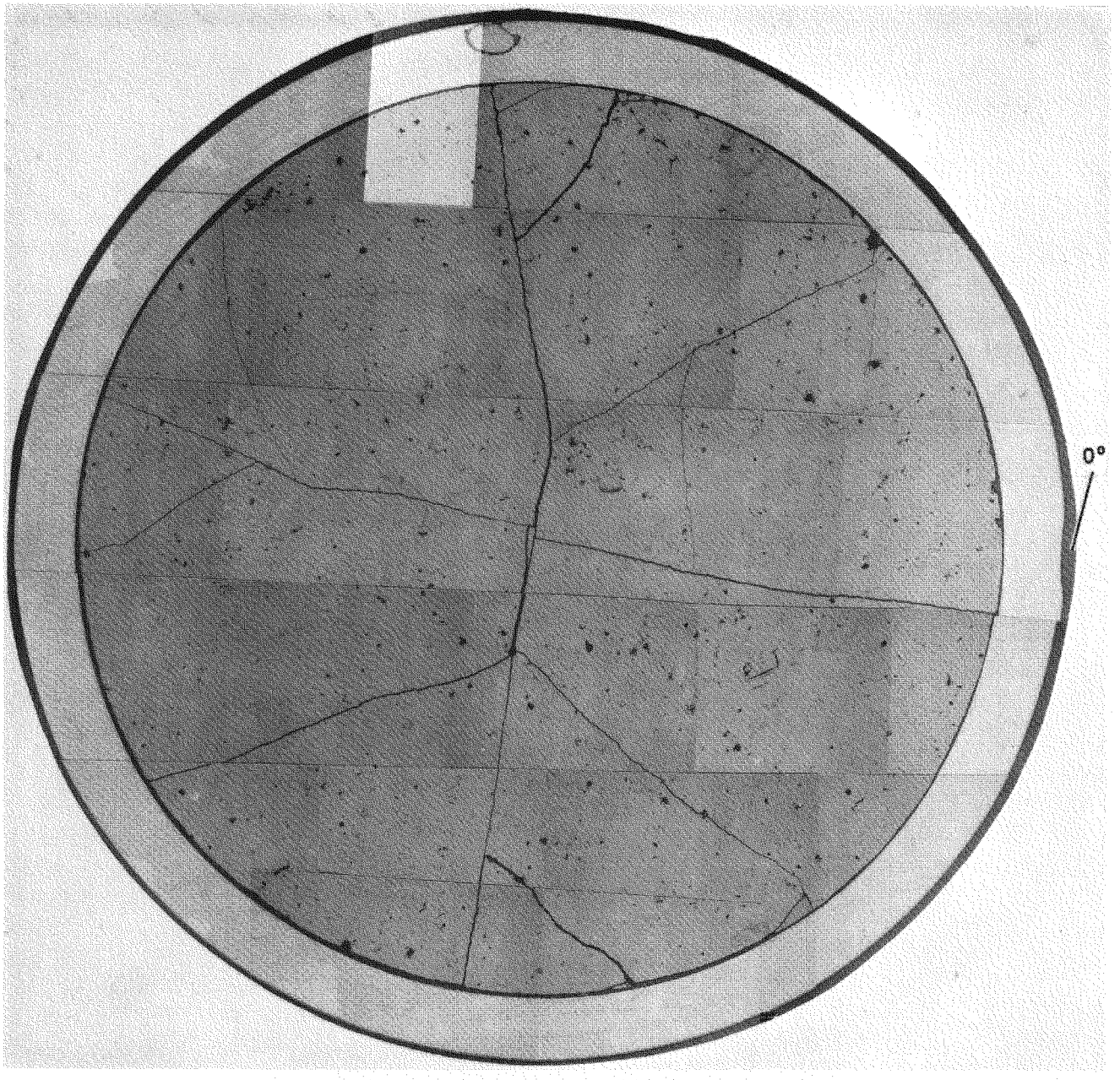

FIGURE A-5. Mosaic of Sample G7-28 (115.5 in.).

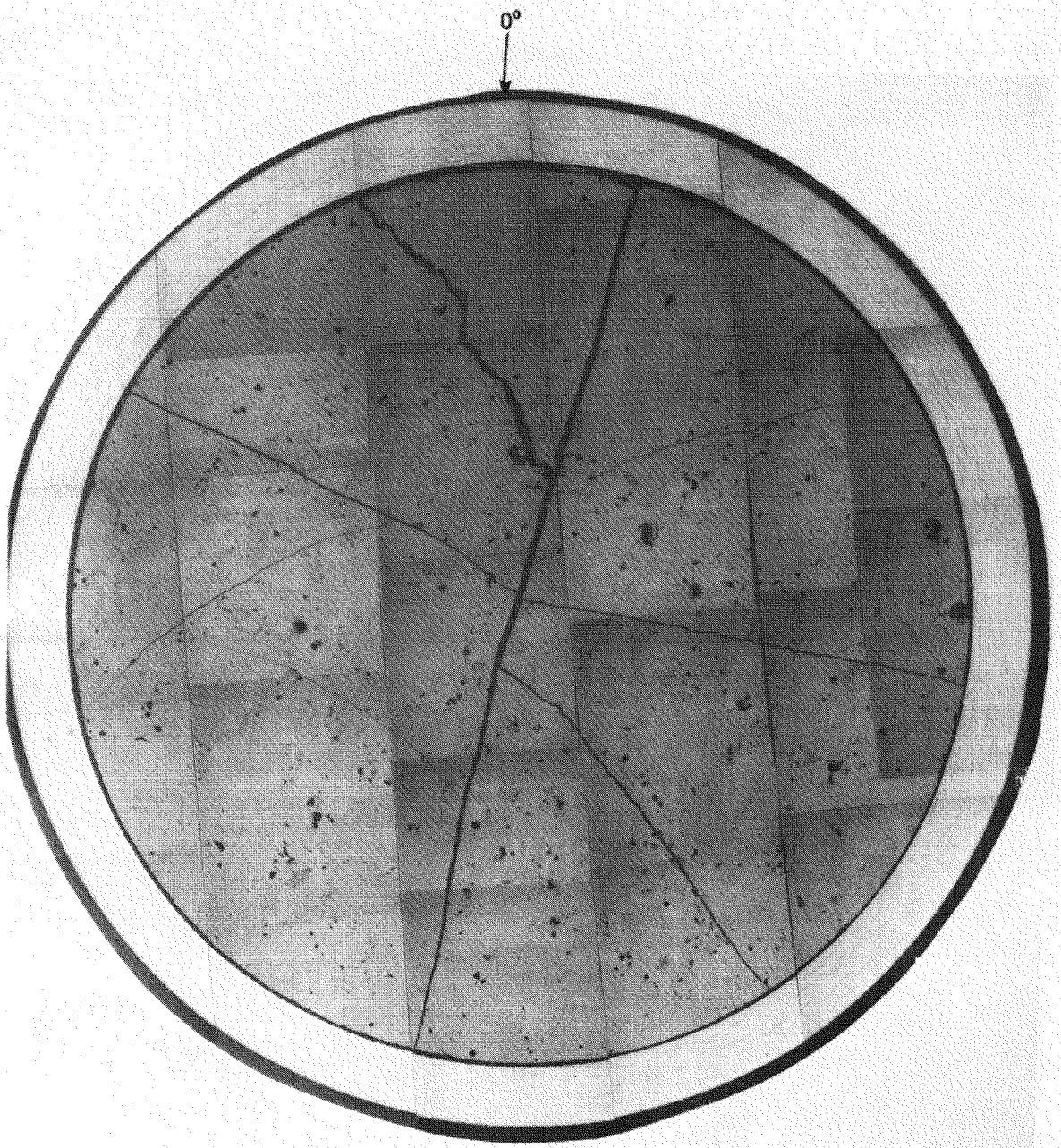

FIGURE A-6. Mosaic of Sample G7-36 (134.5 in.).

Neg 7980542-4

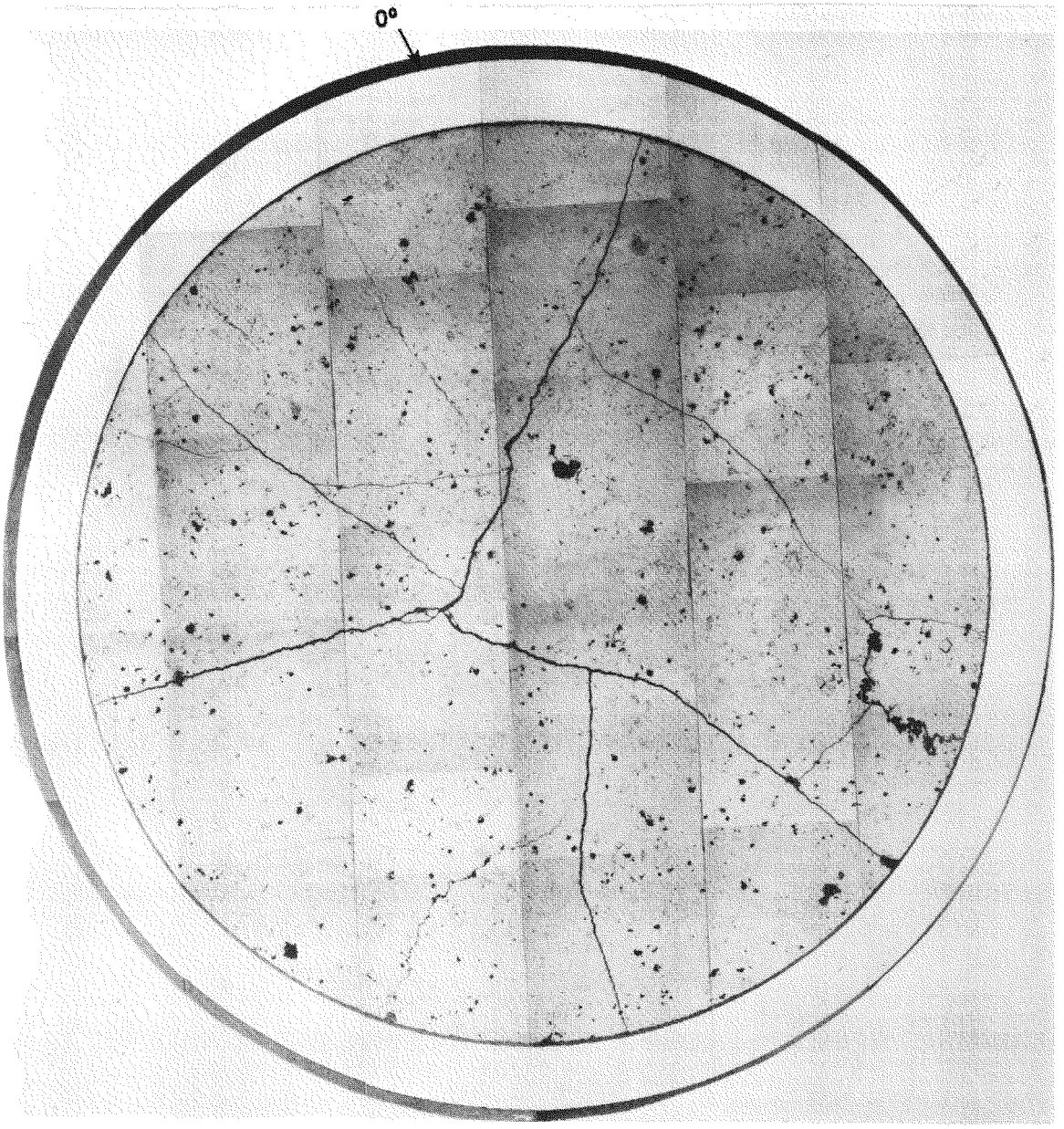

FIGURE A-7. Mosaic of Sample G9-4 (16.5 in.).

Neg 7908542-8

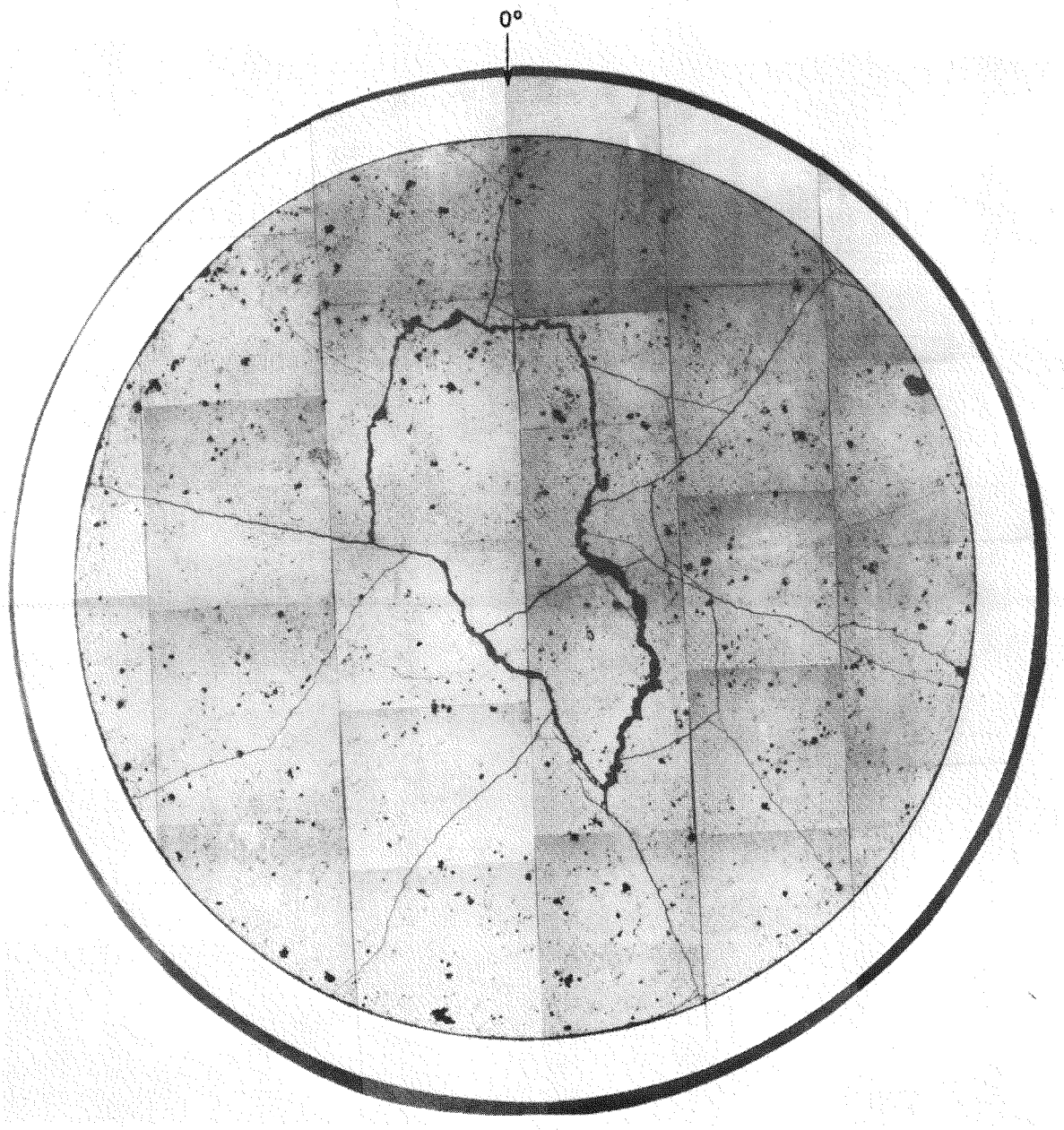

FIGURE A-8. Mosaic of Sample G9-8 (45.5 in.).

Neg 7908542-5

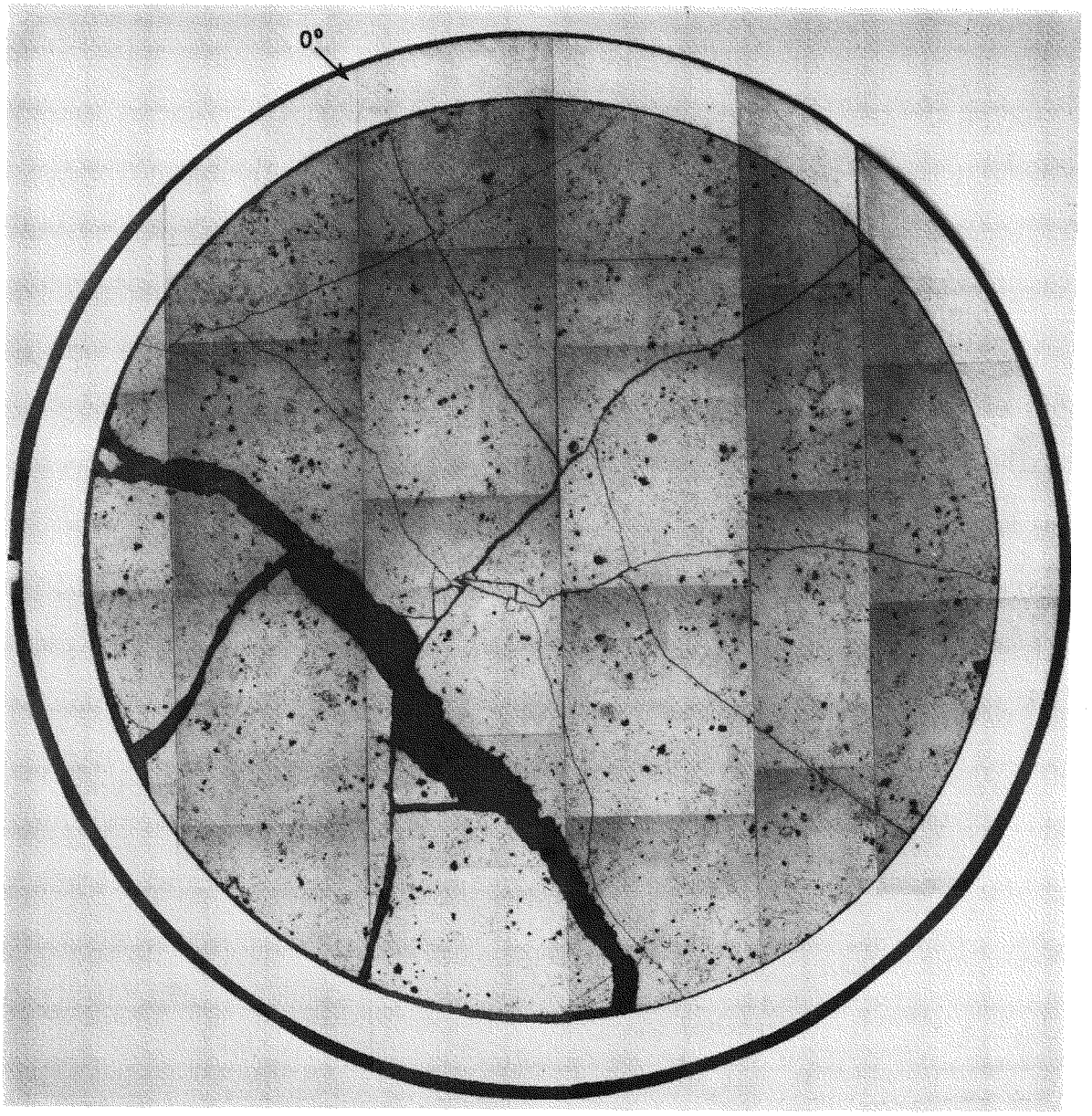

FIGURE A-9. Mosaic of Sample G9-14 (71.0 in.).

Neg 7908542-9

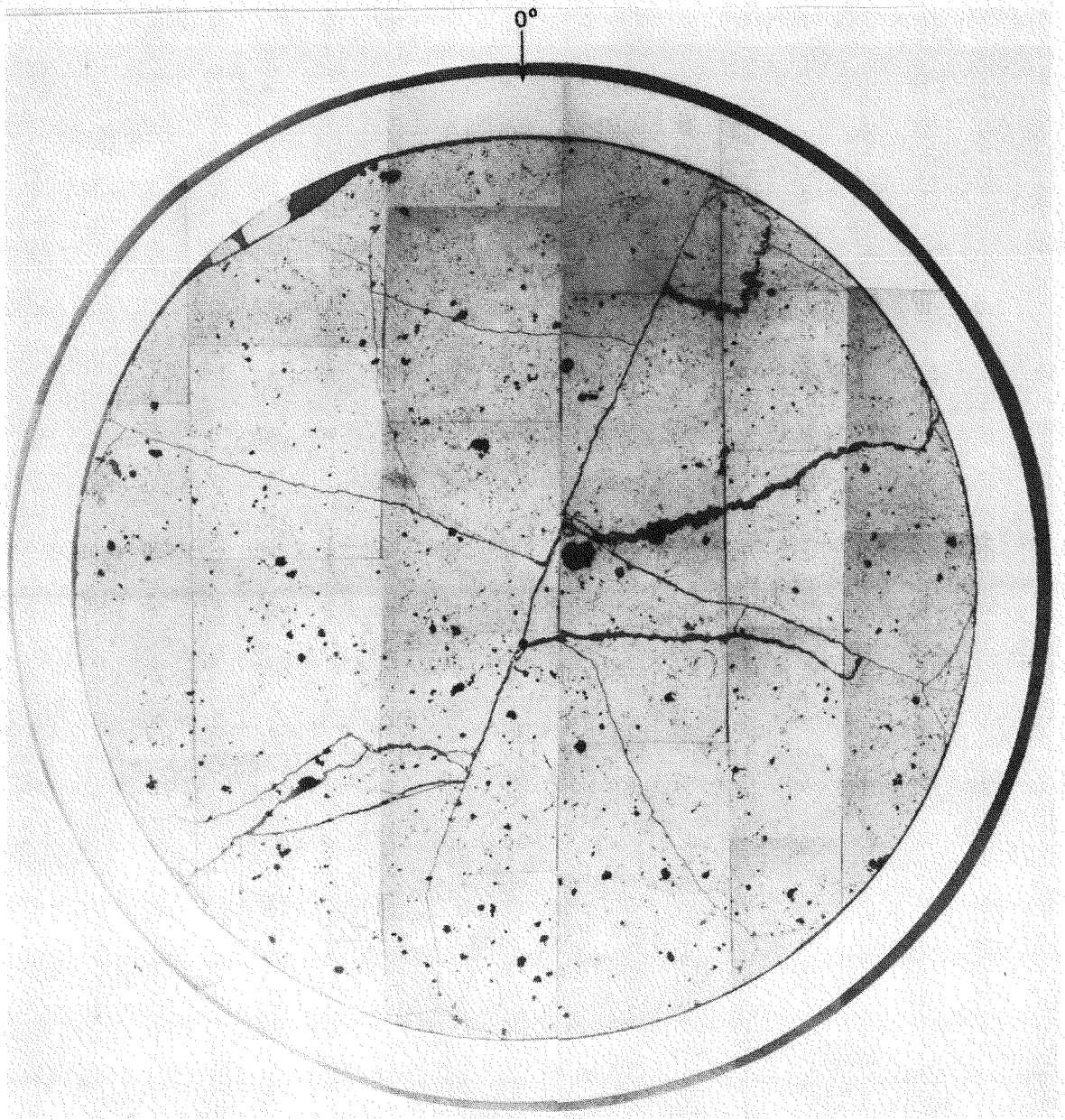

FIGURE A-10. Mosaic of Sample G9-22 (91.0 in.).

Neg 7908542-2

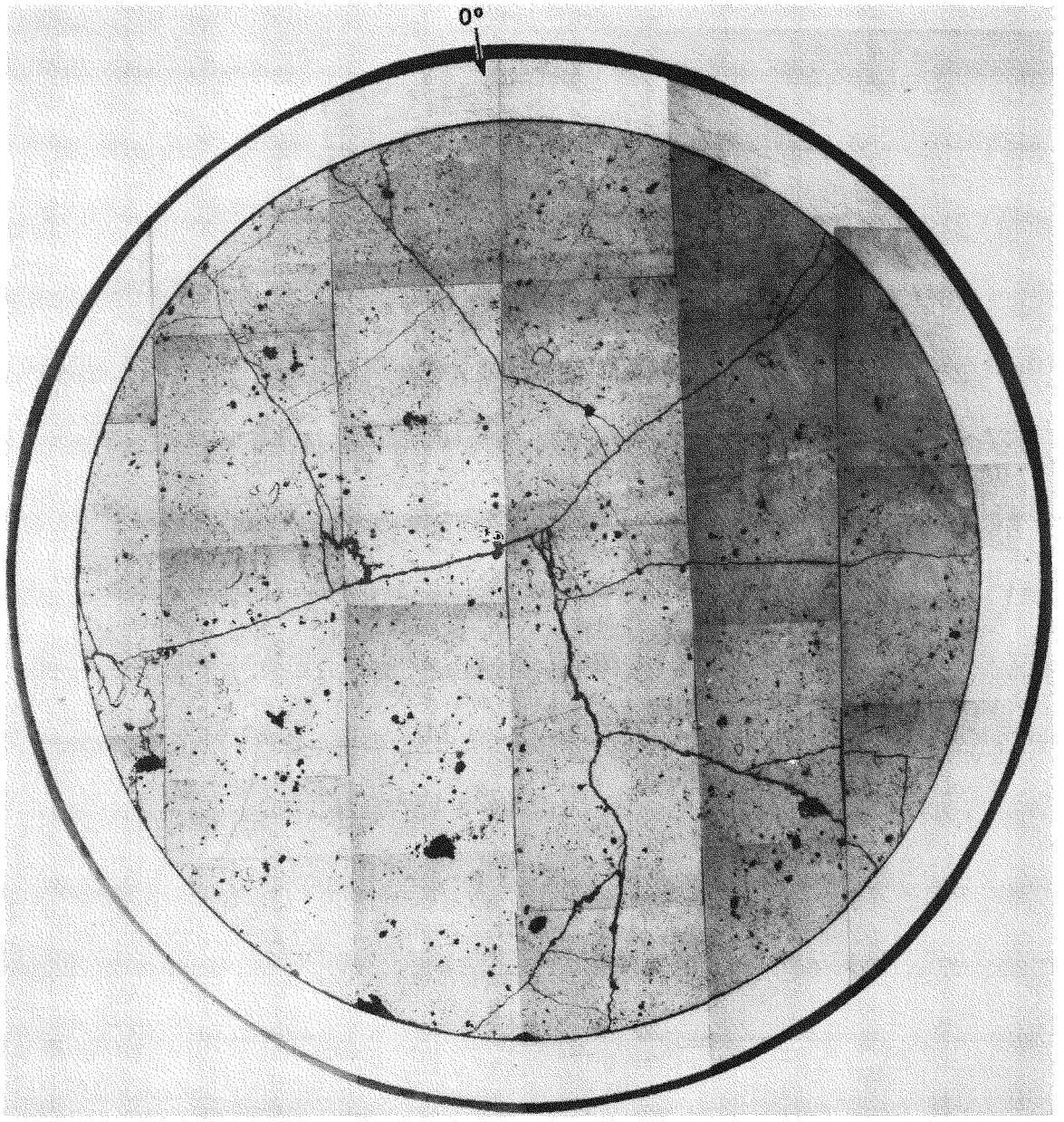

FIGURE A-11. Mosaic of Sample G9-29 (115.5 in.).

Neg 7908542-3

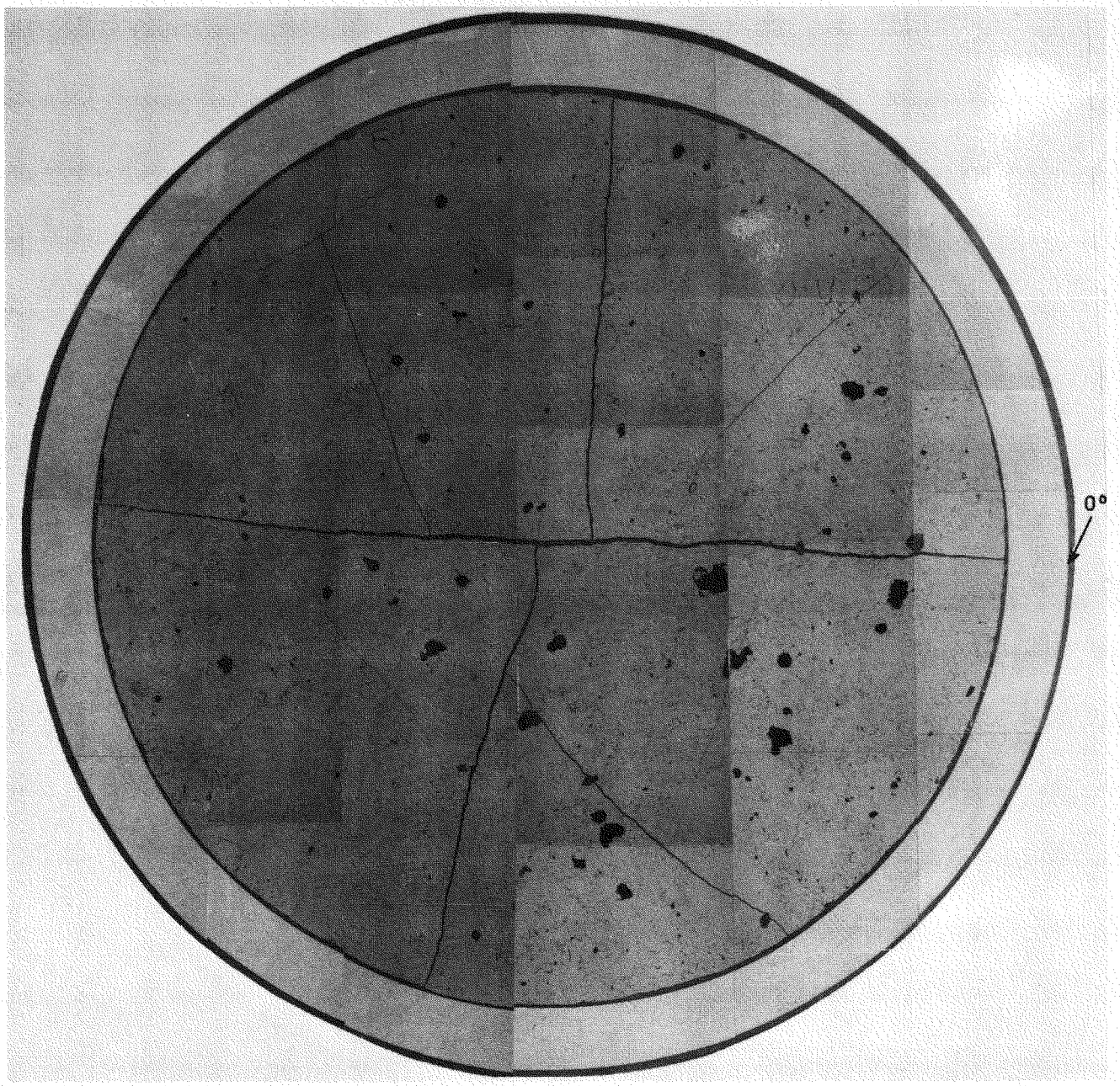

FIGURE A-12. Mosaic of Sample G9-36 (134.5 in.).

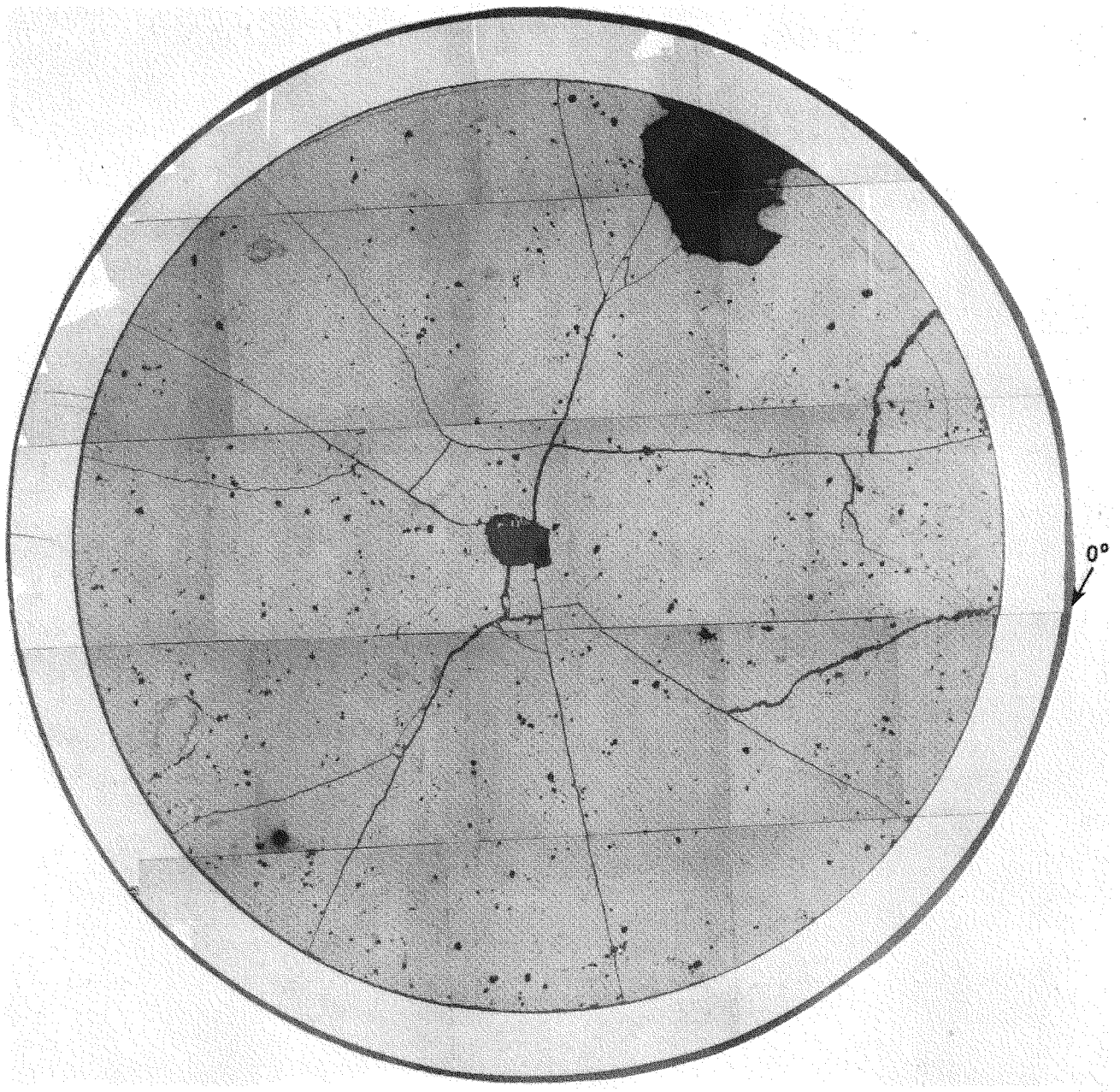

FIGURE A-13. Mosaic of Sample H6-8 (45.5 in.).

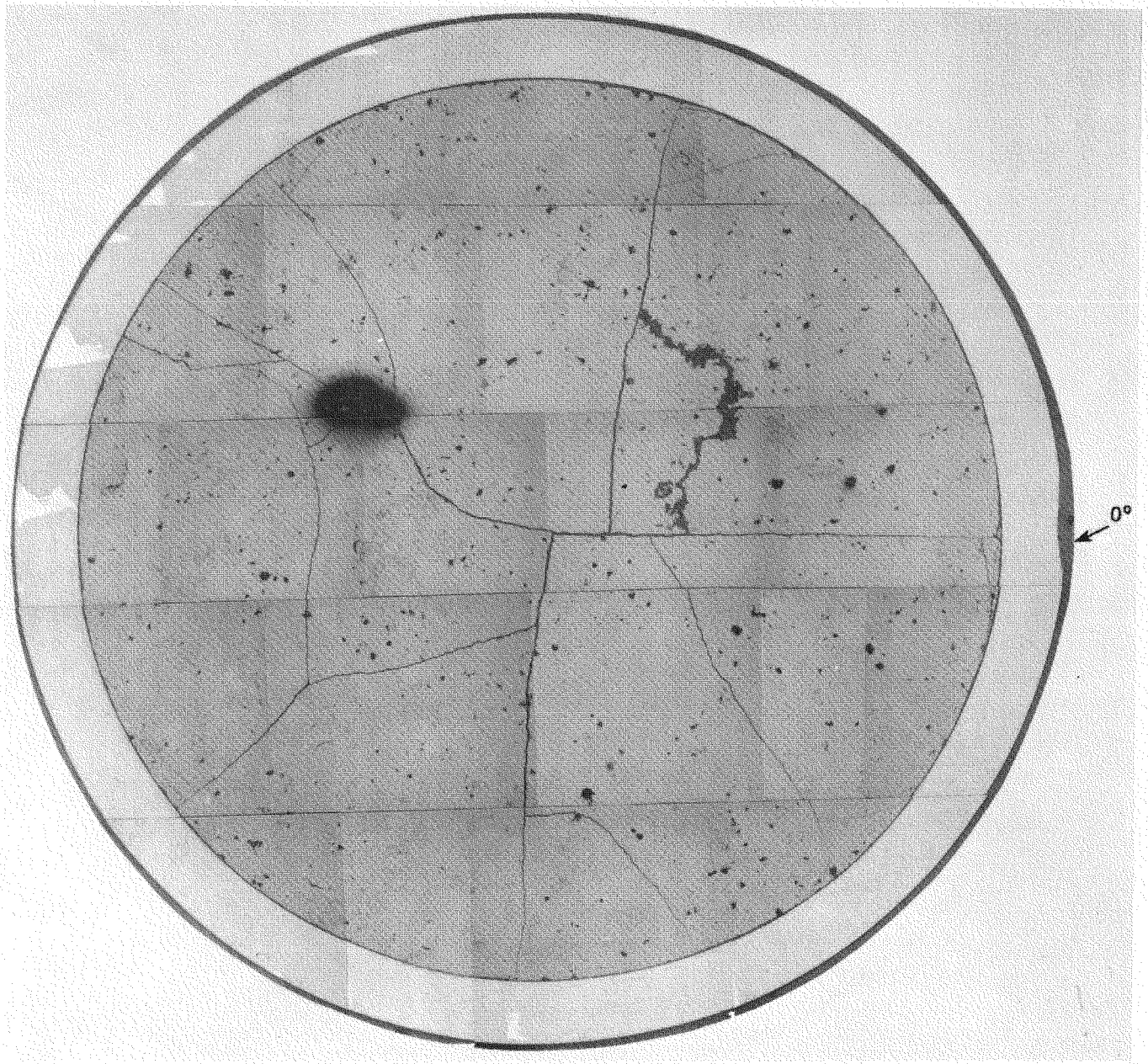

FIGURE A-14. Mosaic of Sample H6-20 (91.5 in.).

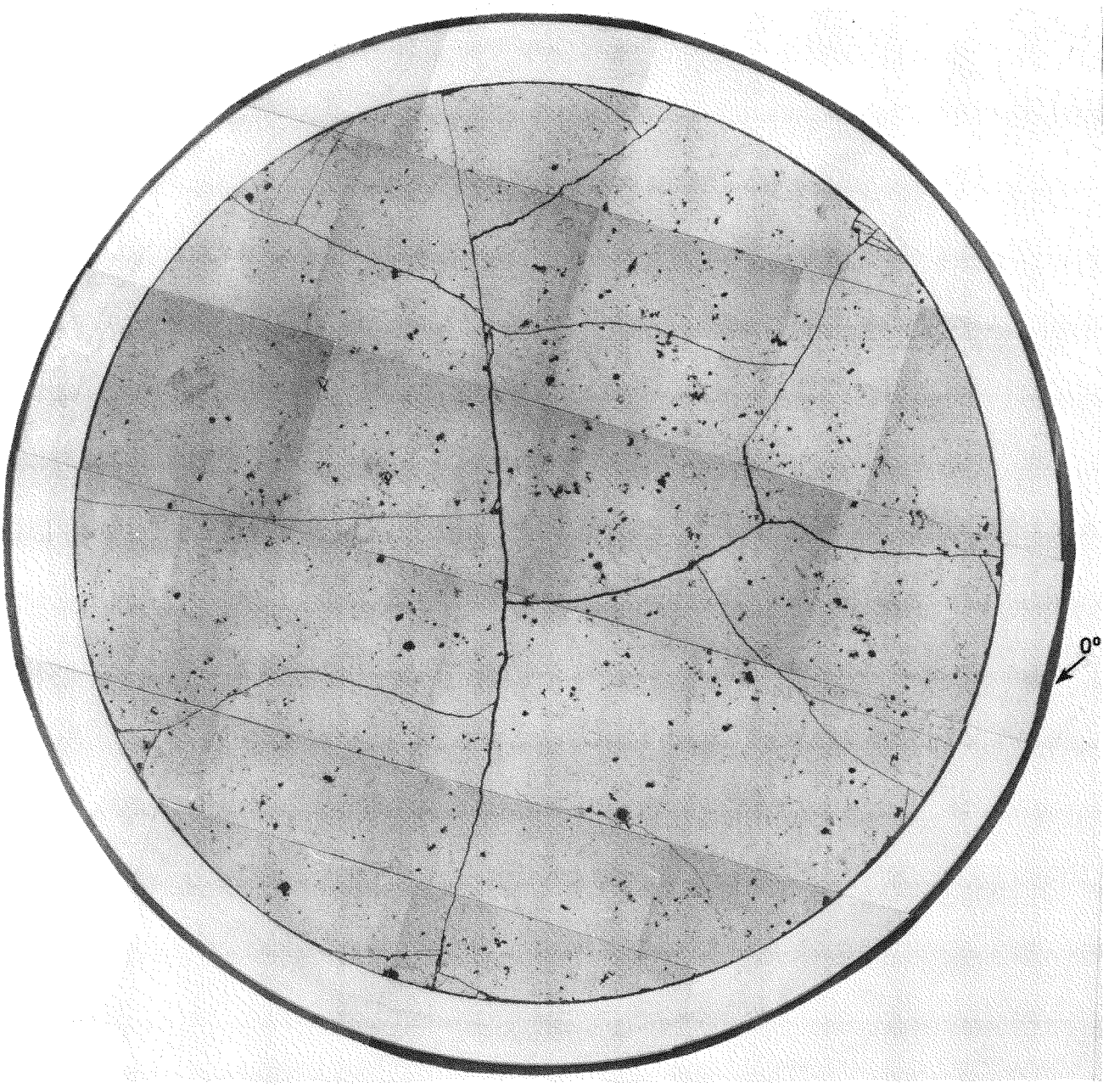

FIGURE A-15. Mosaic of Sample H6-25 (115.5 in.).

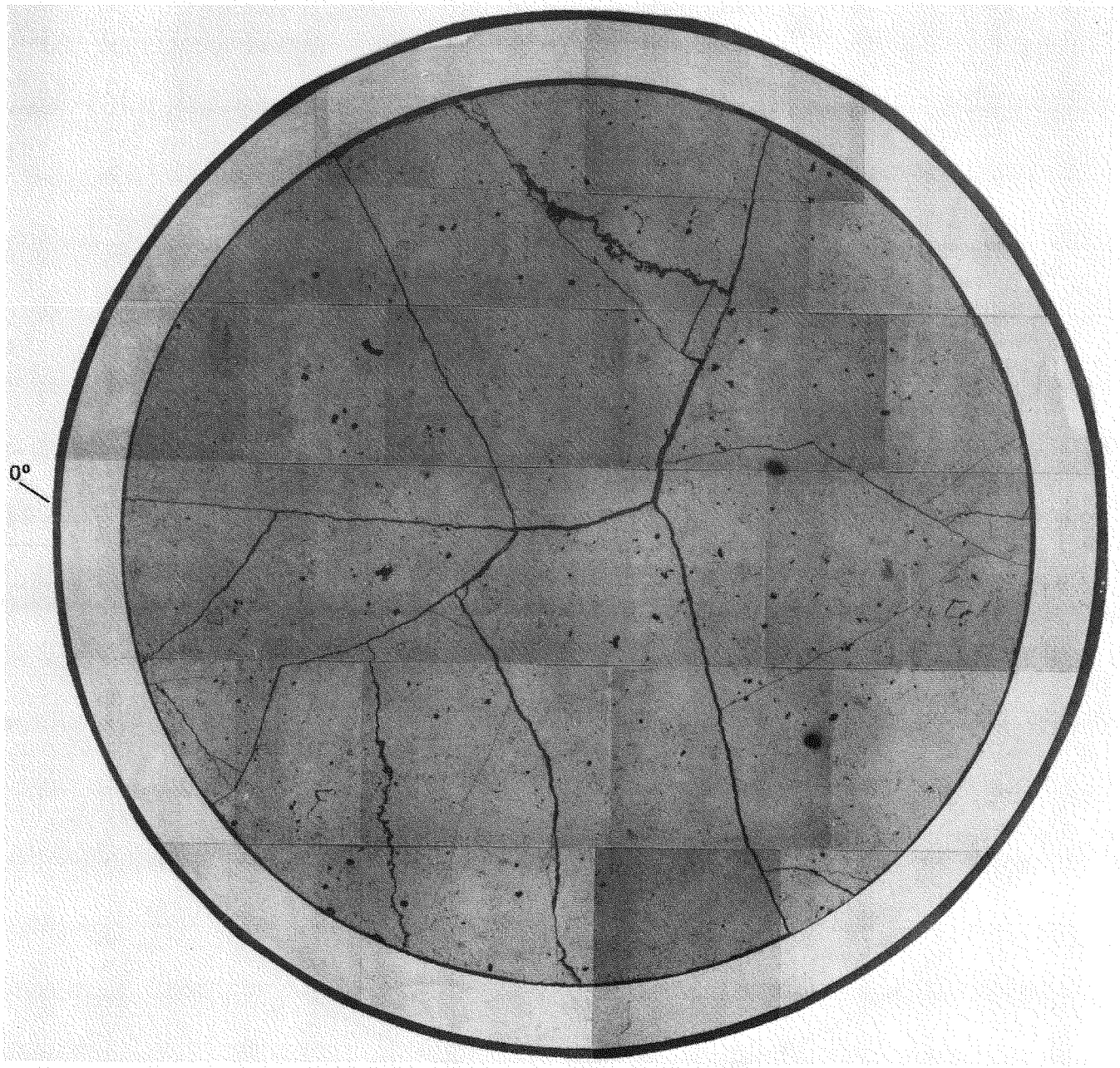

FIGURE A-16. Mosaic of Sample I9-4 (16.5 in.).

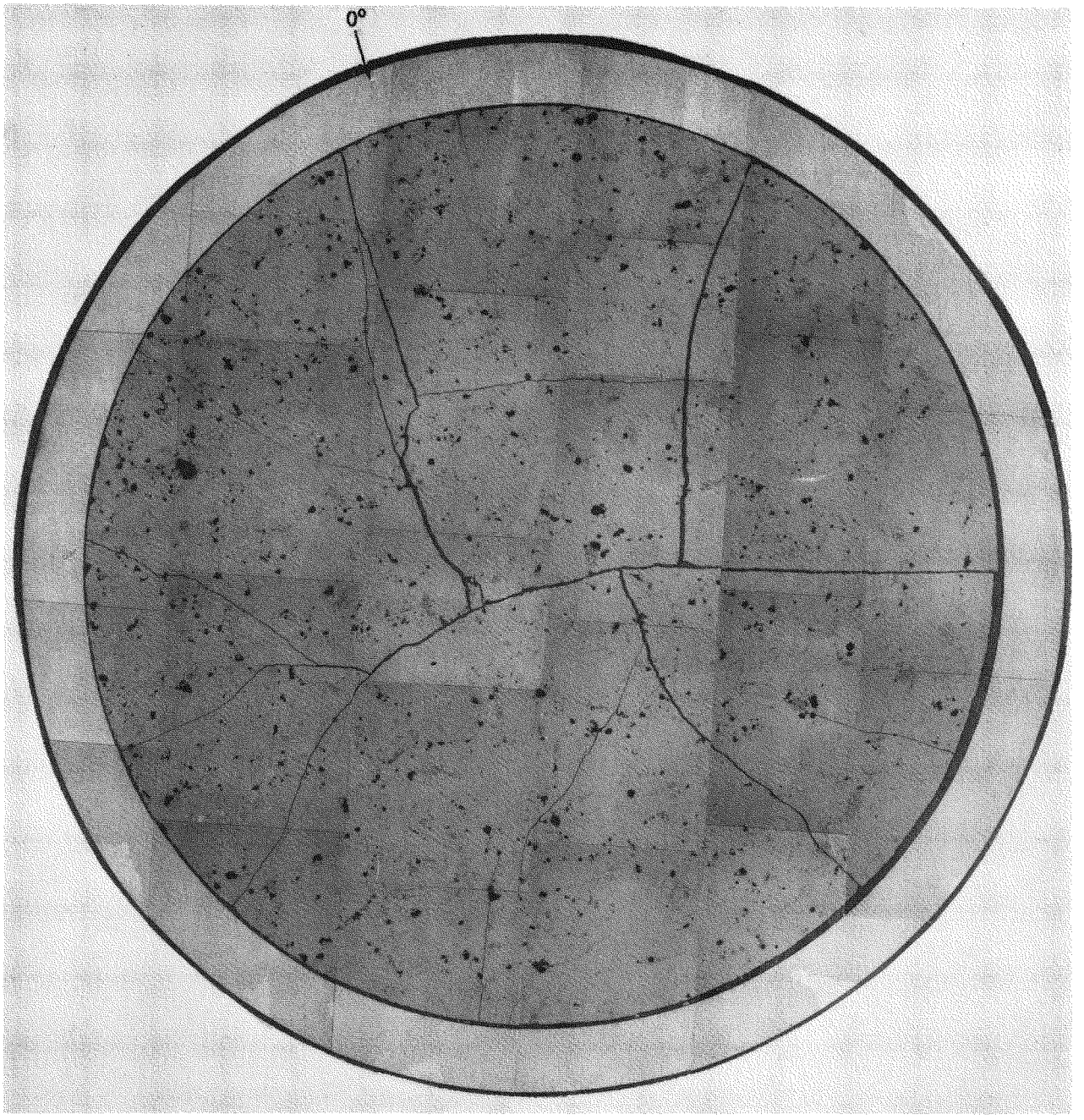

FIGURE A-17. Mosaic of Sample I9-8 (45.5 in.).

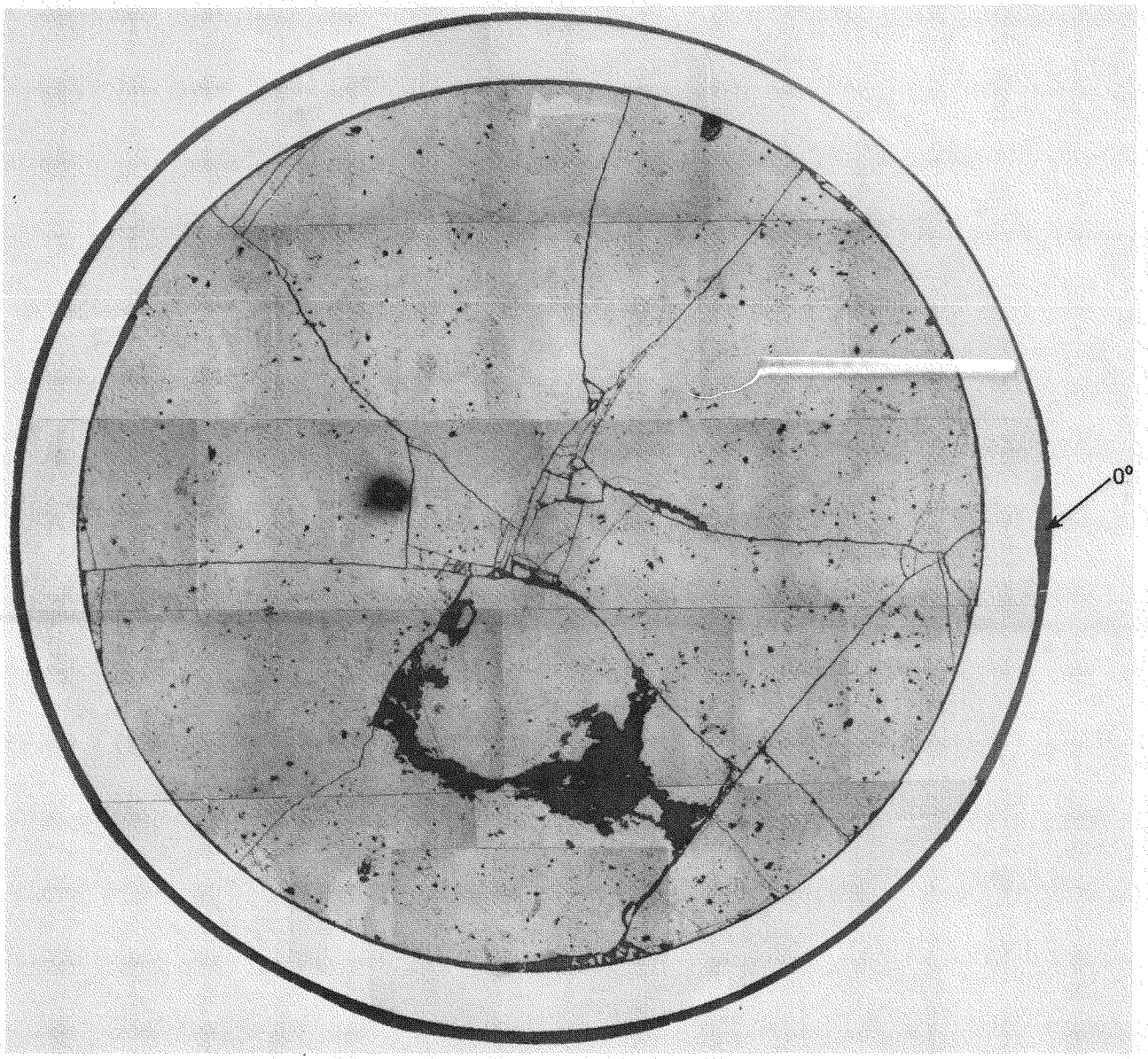

FIGURE A-18. Mosaic of Sample I9-14 (71.0 in.).

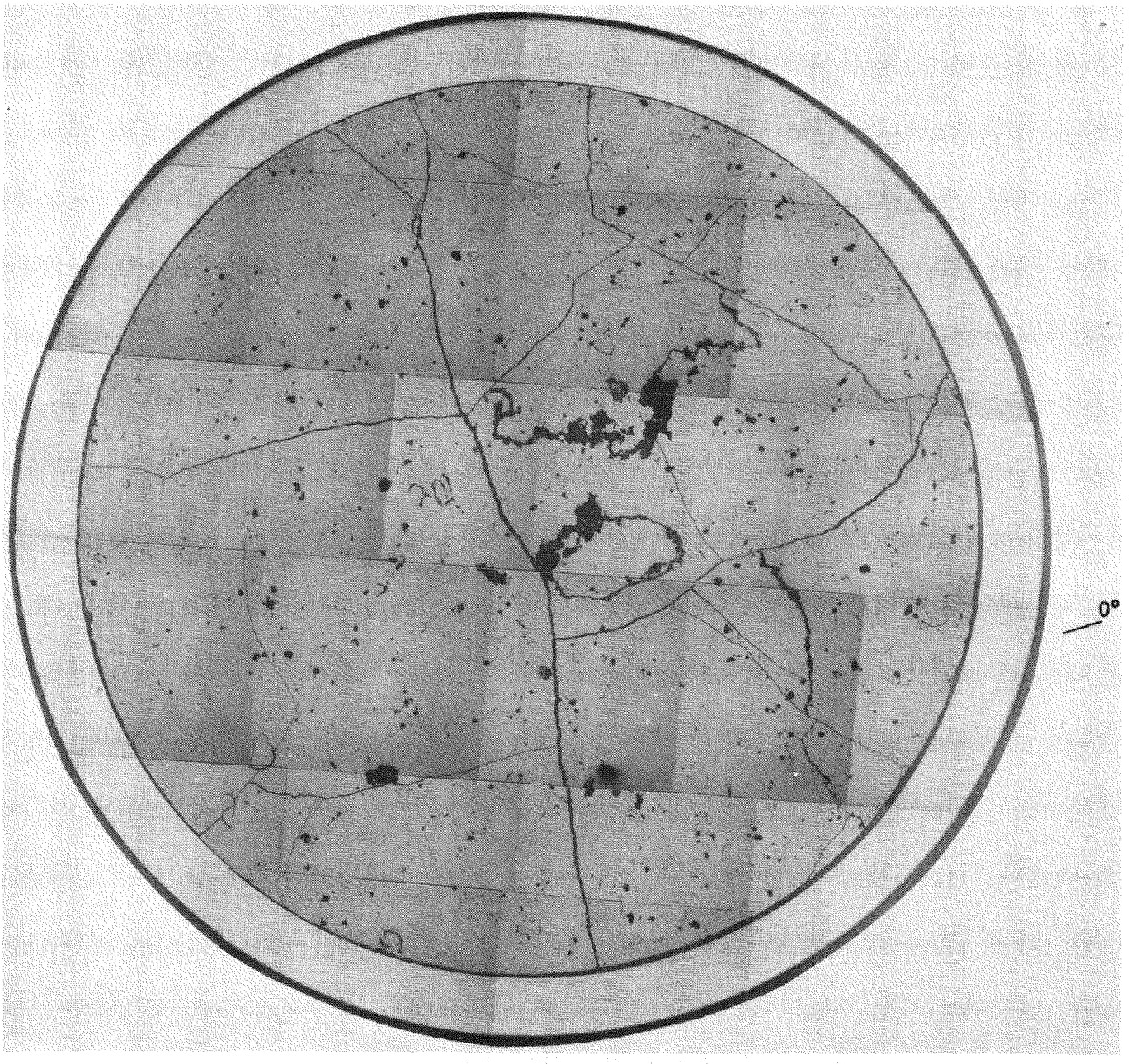

FIGURE A-19. Mosaic of Sample I9-25 (115.5 in.).

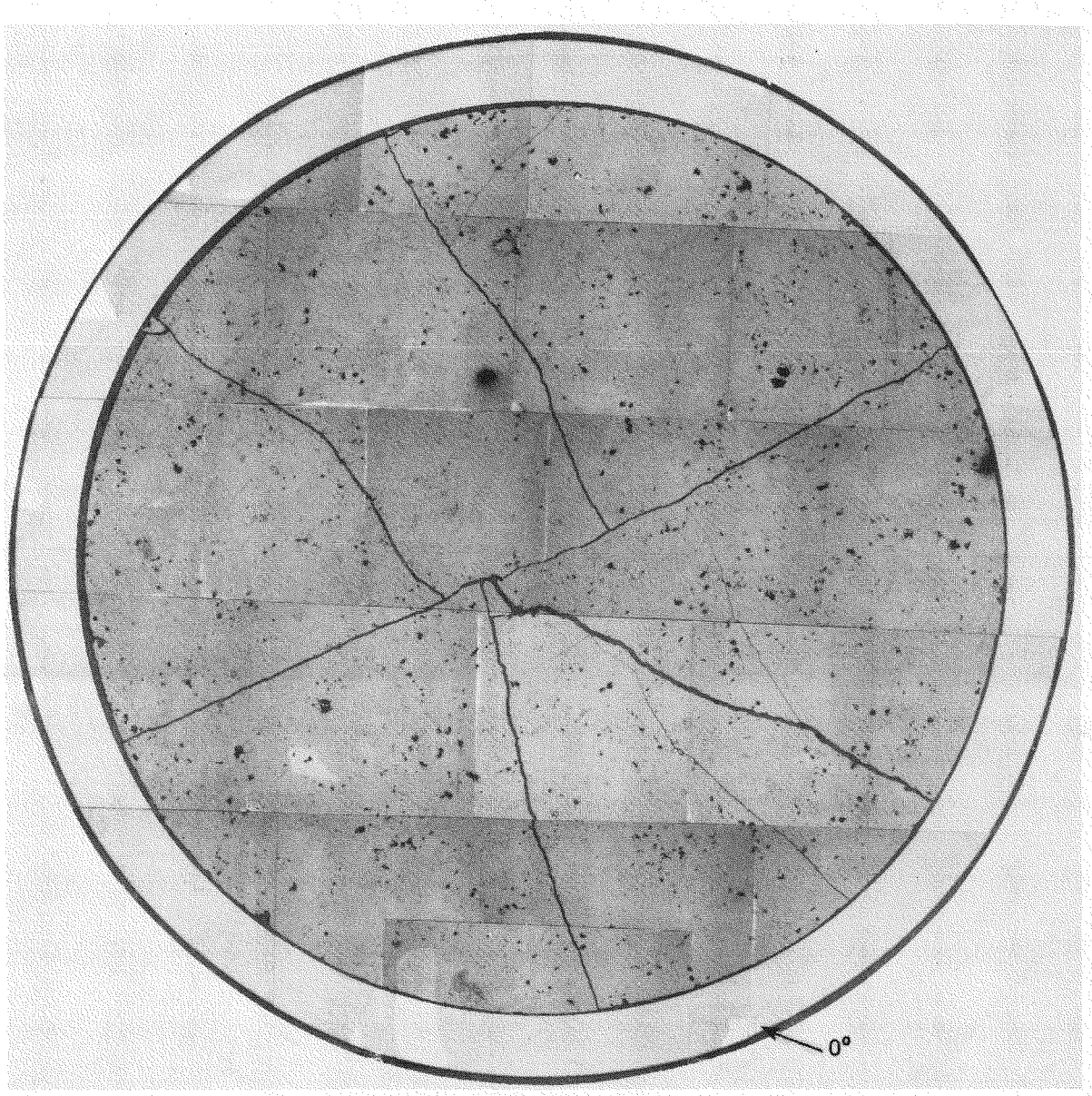

FIGURE A-20. Mosaic of Sample I9-31 (134.5 in.).

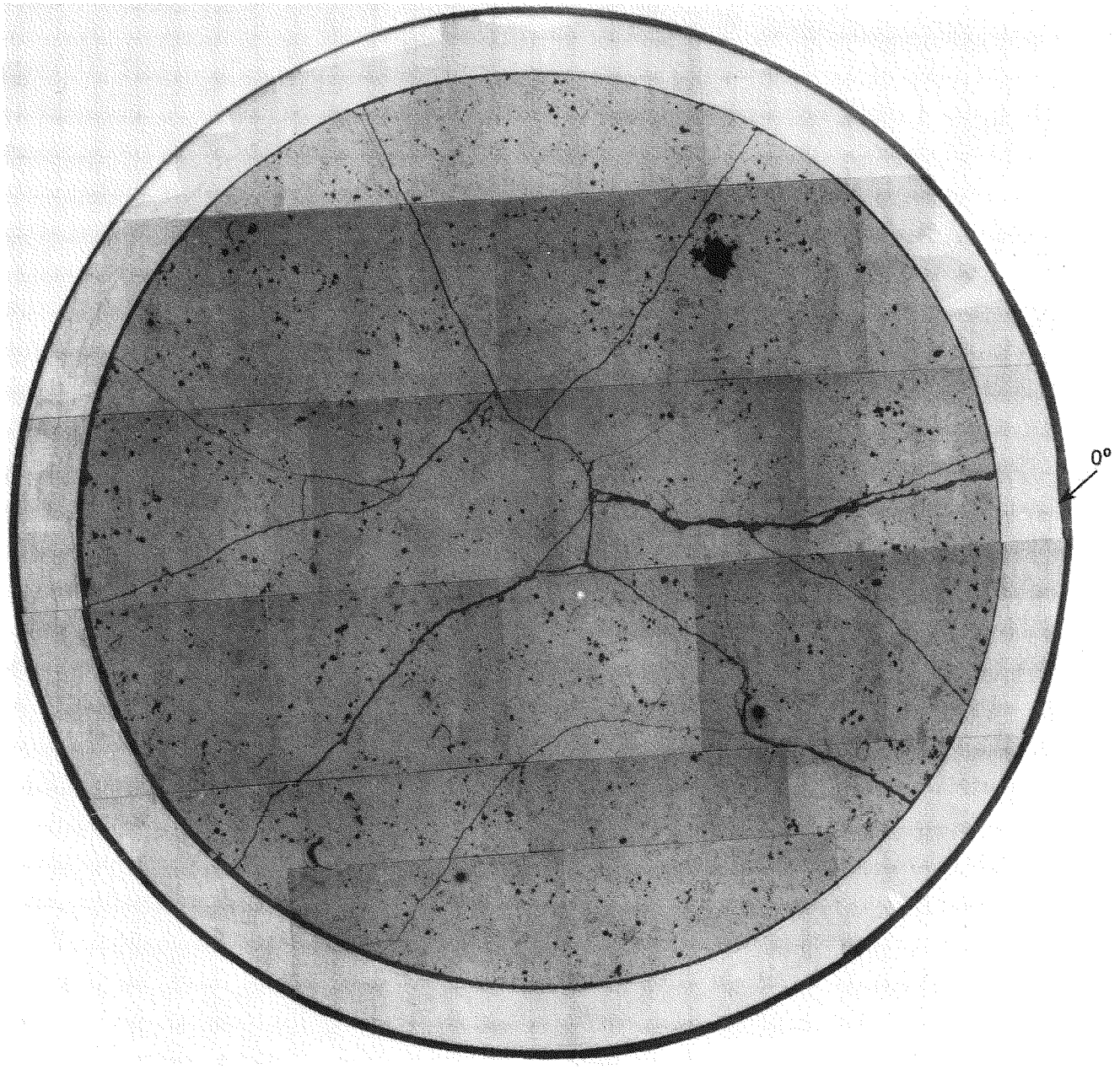

FIGURE A-21. Mosaic of Sample J8-25 (115.5 in.).

A P P E N D I X B

PLOTS OF CLADDING WIDTH MEASUREMENTS TO RADIAL ORIENTATION

FIGURES

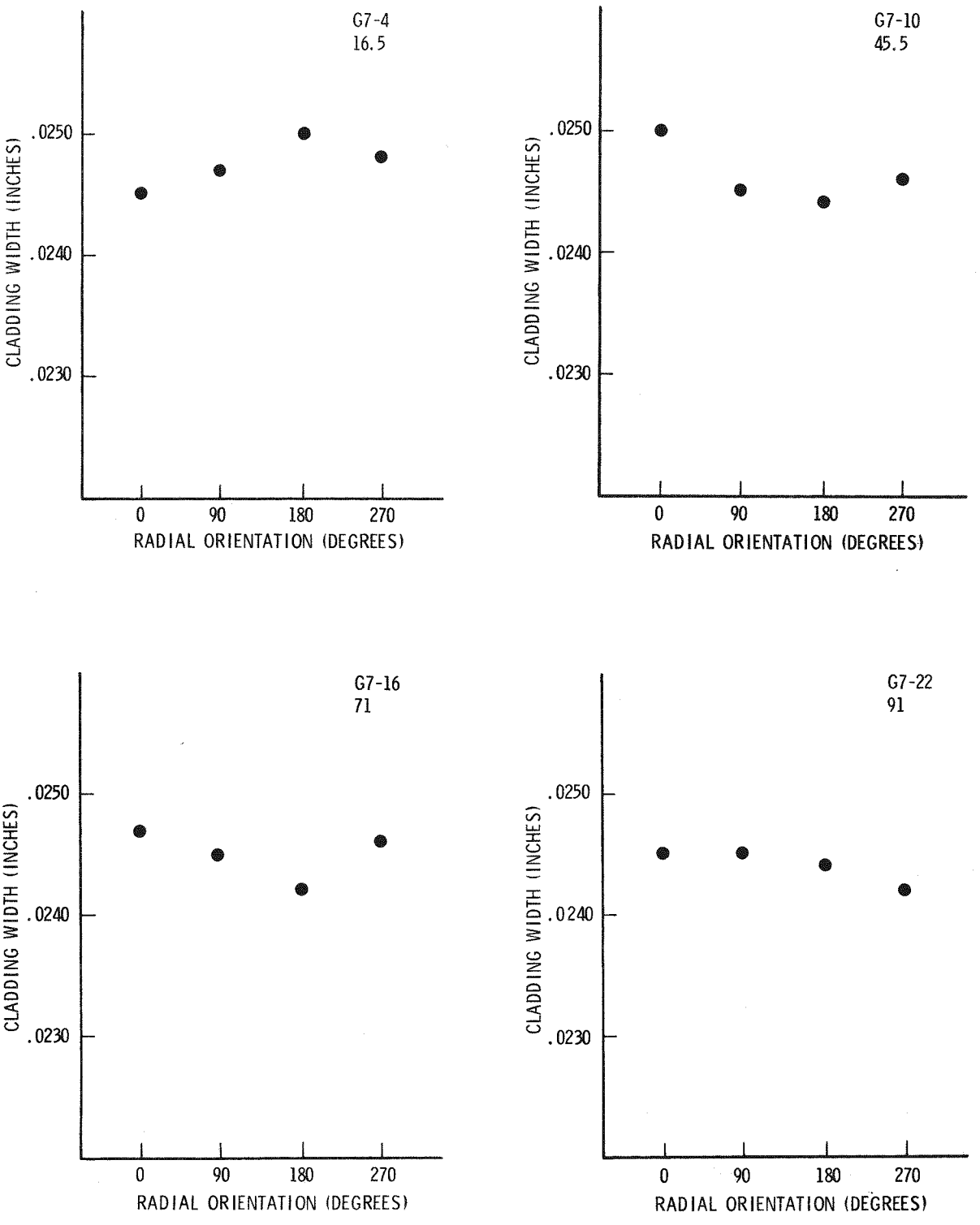

FIGURE B-1. Plots of Cladding Width Measurements to Radial Orientation for Samples G7-4, G7-10, G7-16, and G7-22.

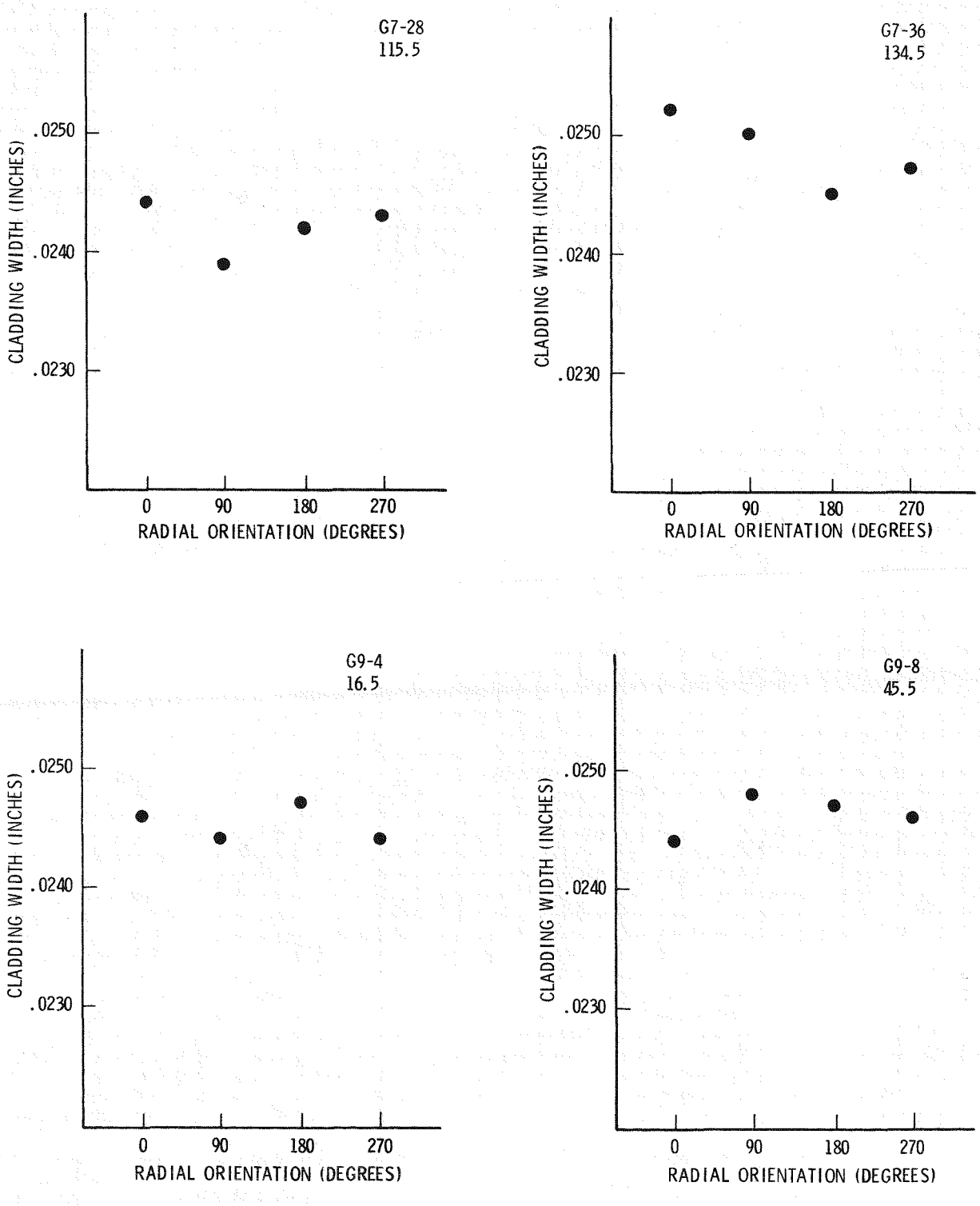

FIGURE B-2. Plots of Cladding Width Measurements to Radial Orientation for Samples G7-28, G7-36, G9-4, and G9-8.

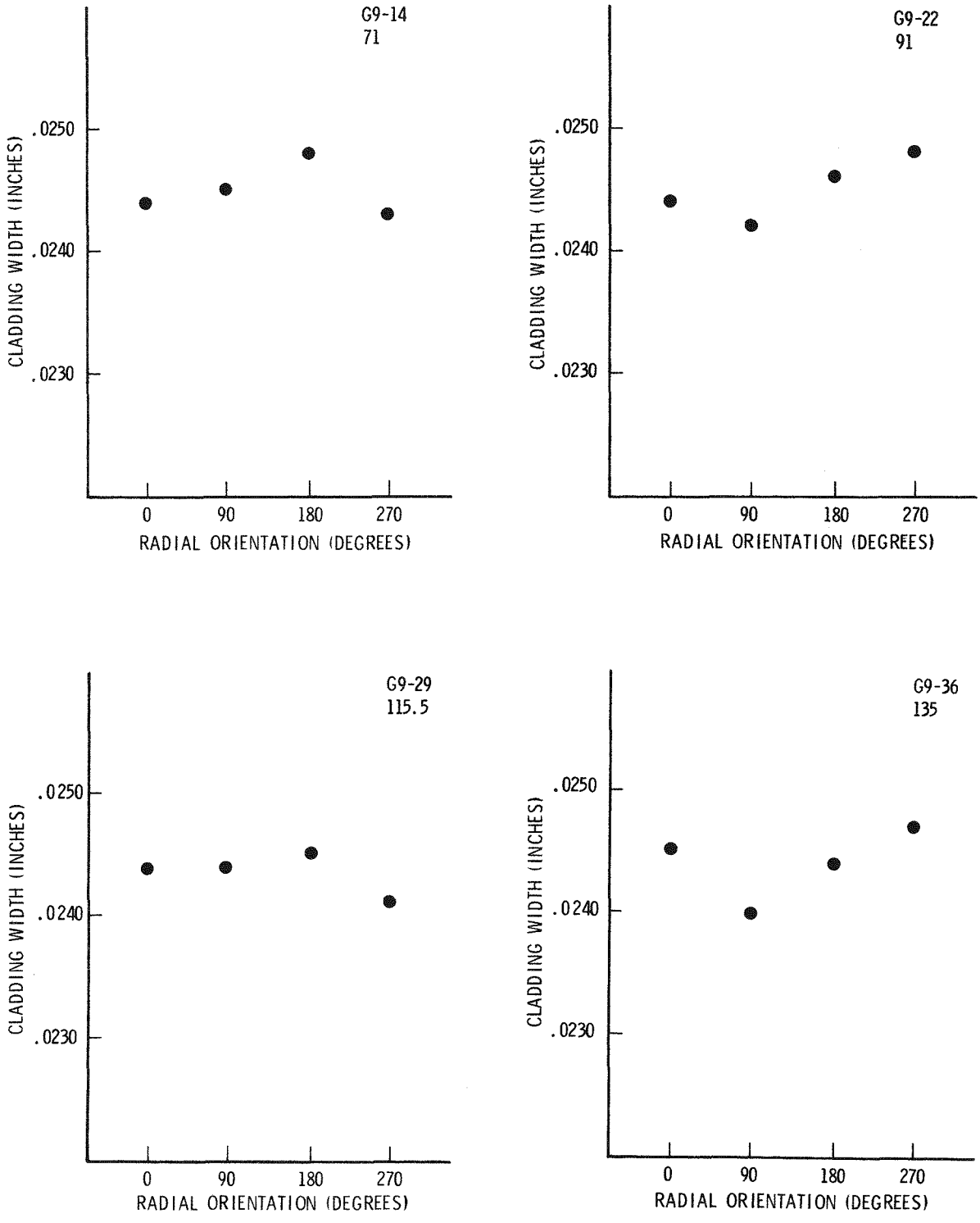

FIGURE B-3. Plots of Cladding Width Measurements to Radial Orientation for Samples G9-14, G9-22, G9-29, and G9-36.

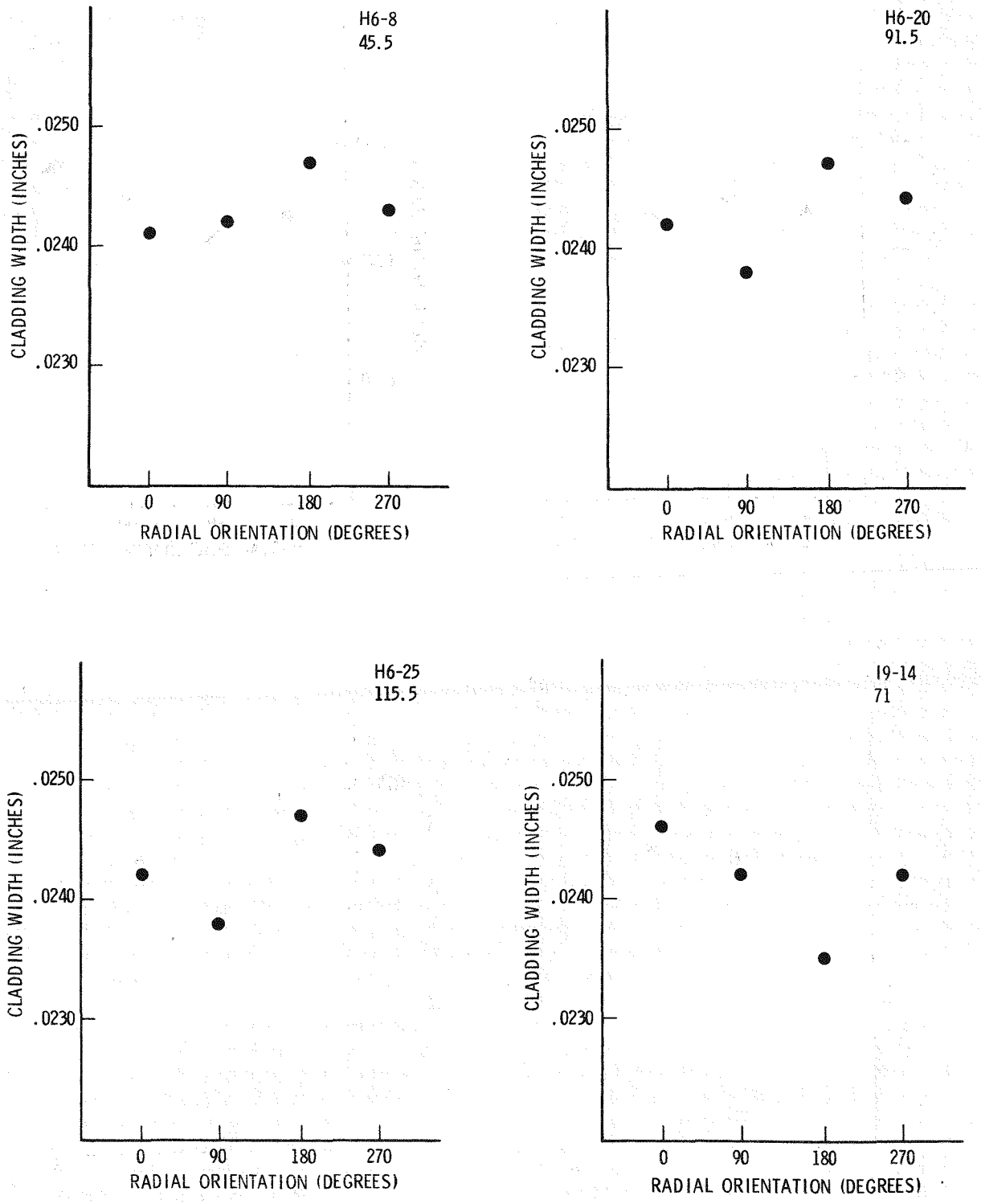

FIGURE B-4. Plots of Cladding Width Measurements to Radial Orientation for Samples H6-8, H6-20, H6-25, and I9-14.

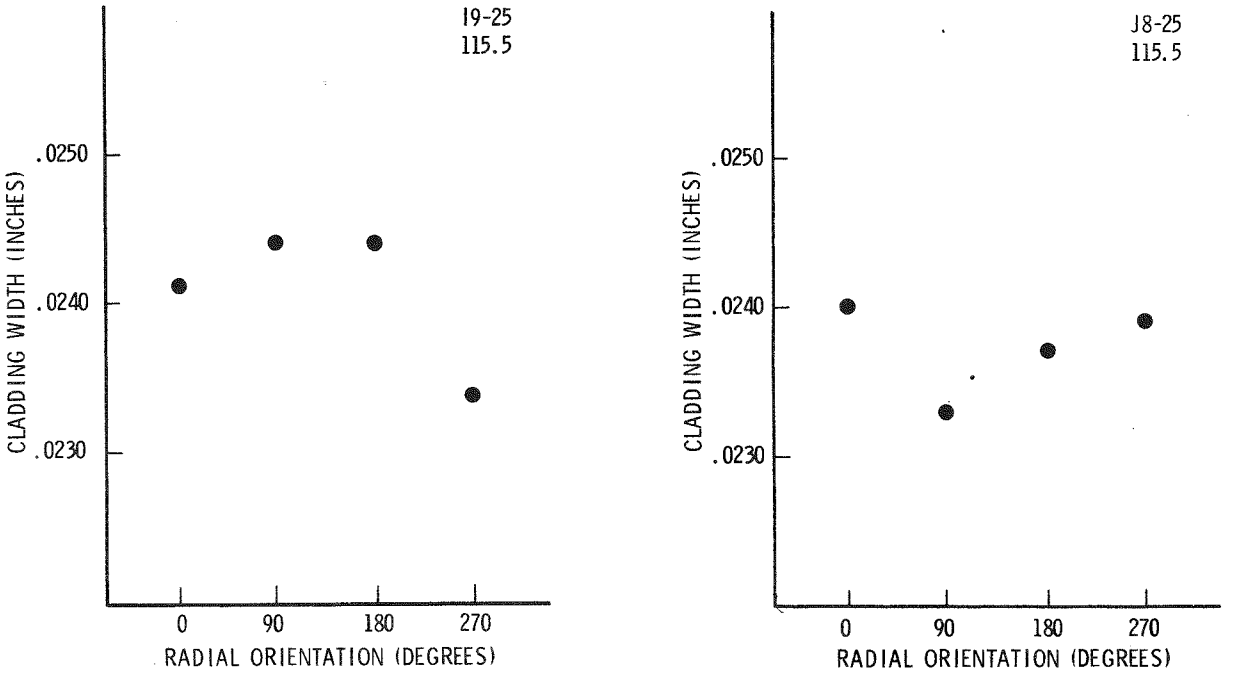

FIGURE B-5. Plots of Cladding Width Measurements to Radial Orientation for Samples I9-25 and J8-25.

A P P E N D I X C

PLOTS OF OXIDE THICKNESS TO RADIAL ORIENTATION

FIGURES

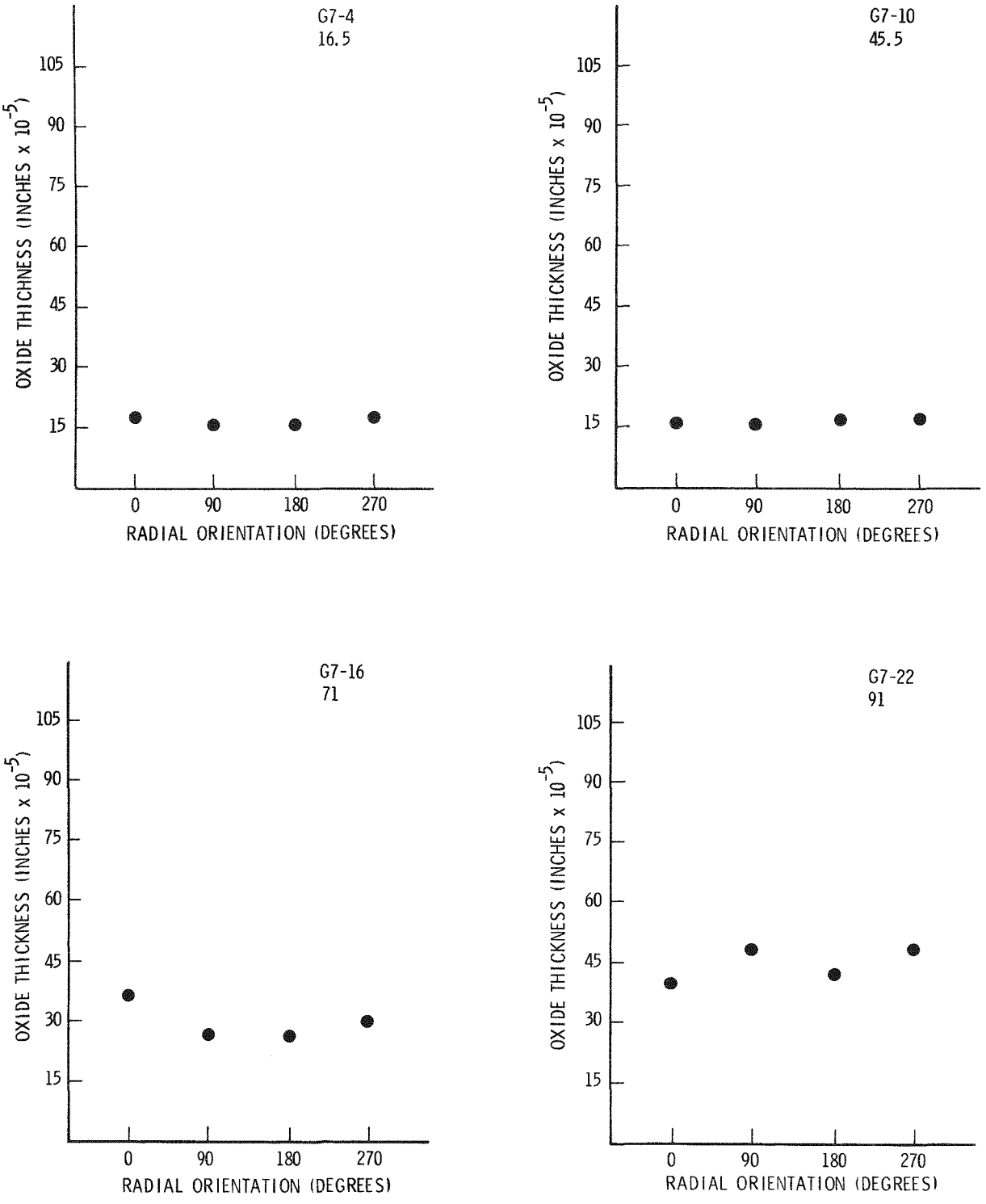

FIGURE C-1. Plots of Oxide Thickness to Radial Orientation for Samples G7-4, G7-10, G7-16, and G7-22.

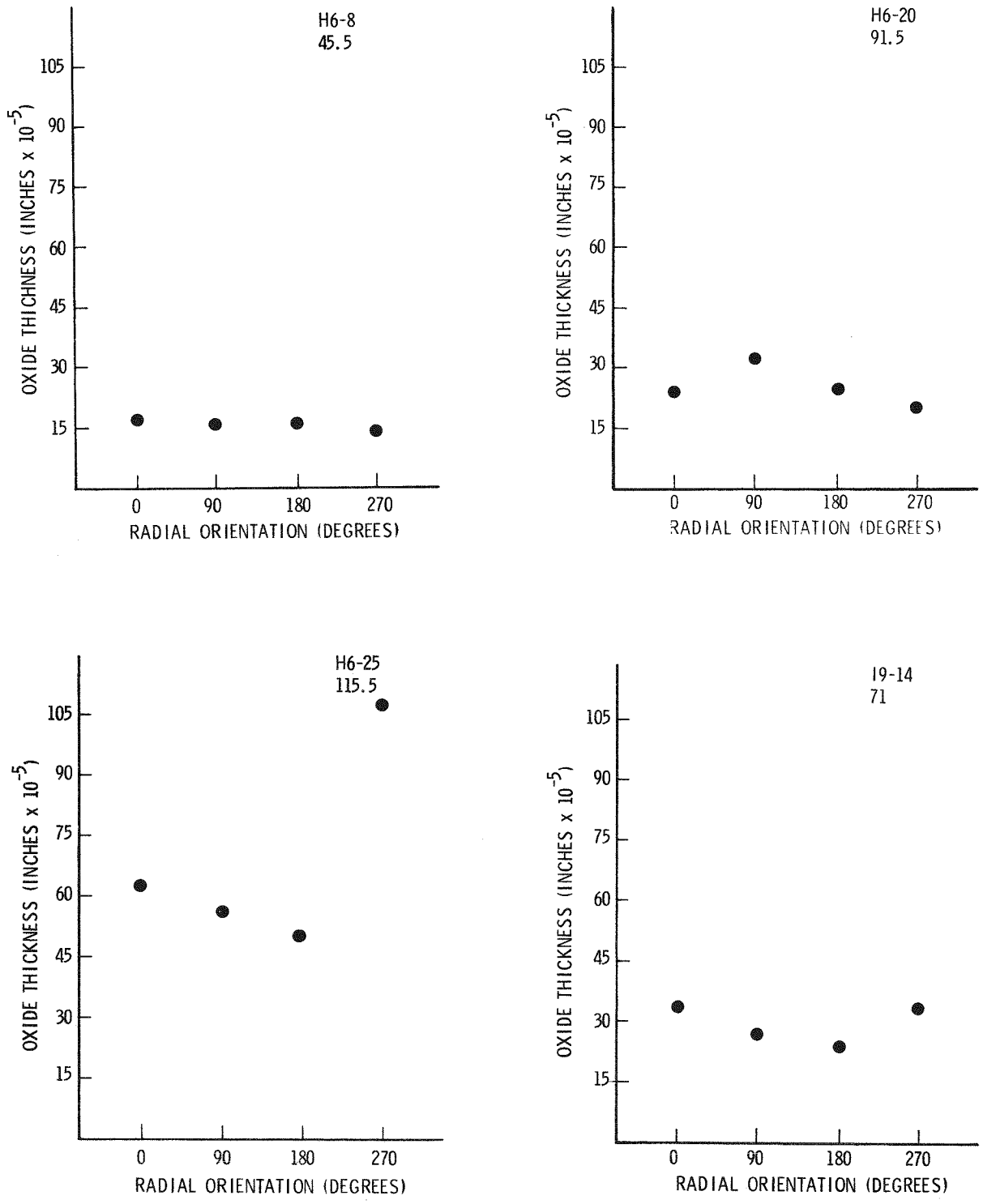

FIGURE C-4. Plots of Oxide Thickness to Radial Orientation for Samples H6-8, H6-20, H6-25, and I9-14.

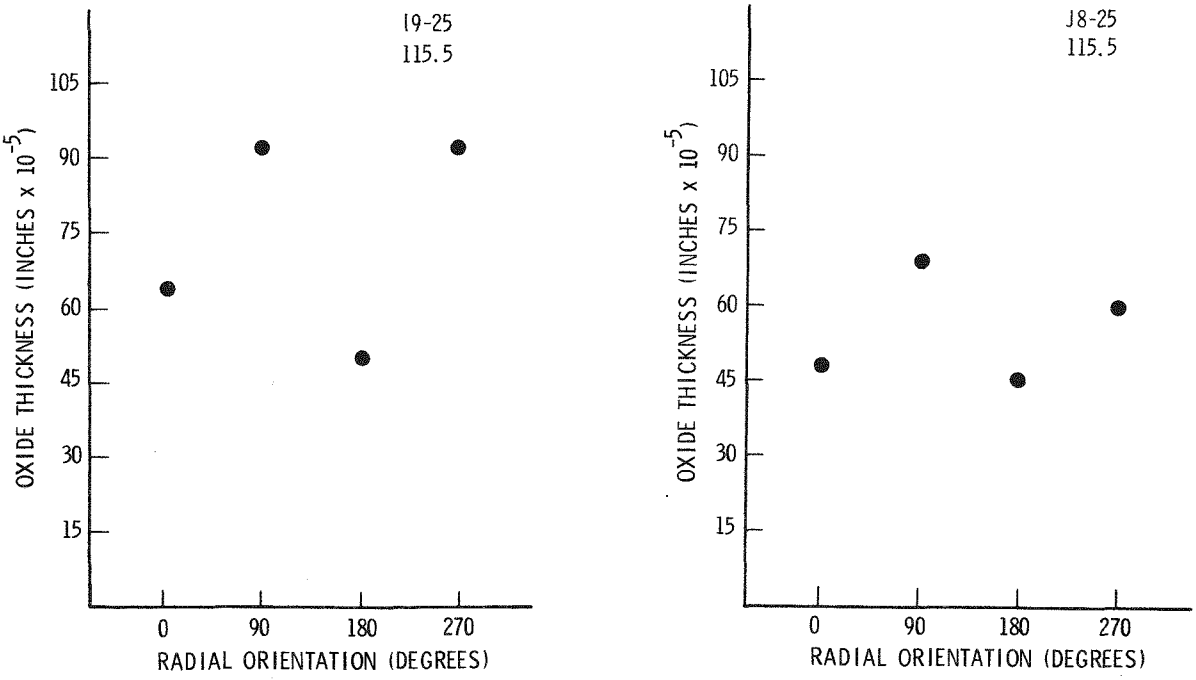

FIGURE C-5. Plots of Oxide Thickness to Radial Orientation for Samples I9-25 and J8-25.

A P P E N D I X D

FISSION GAS RELEASE CALCULATION

FISSION GAS RELEASE CALCULATION

The assembly average burnup was reported to be 25,665 MWd/MTU multiplied by a conversion factor for MWd to MeV,

$$\text{Energy/MTU} = \frac{25{,}665}{1.85 \times 10^{-24}}$$

$$= 1.387 \times 10^{28} \text{ MeV/MTU}$$

With an approximate 200 MeV per fission event of ^{235}U and ^{238}U, the number of fissions is

$$\text{Fissions/MTU} = \frac{1.387 \times 10^{28}}{200}$$

$$= 6.93 \times 10^{25} \text{ Fissions/MTU}$$

The fuel assembly at start-up contained 0.448 MTU metal in 204 fuel rods. The number of fissions per rod is

$$\text{Fissions/Rod} = (6.93 \times 10^{25})(0.448)\left(\frac{1}{204}\right)$$

$$= 1.52 \times 10^{23} \text{ Fissions/Rod}$$

With a fission gas yield* of 0.266, the number of gas atoms per rod is

$$\text{Fission Gas Atoms/Rod} = (1.52 \times 10^{23})(0.266)$$

$$= 4.043 \times 10^{22} \text{ Fission Gas Atoms/Rod}$$

*END/B files, version 4, Brookhaven National Laboratory.

Then if Avogadro's number and the gas constant 22.4 ℓ/mole is used, the number of liters of fission gas created is

$$\text{Liters of Fission Gas/Rod} = (4.043 \times 10^{22})\left(\frac{1}{6.023 \times 10^{23}}\right)(22.4)$$

$$= 1.503 \text{ ℓ/Rod}$$

From mass analysis of the plenum gas 4.63 cc were found to be fission gas (xenon and krypton); therefore, the percent gas release is

$$\% \text{ Fission Gas Release} = \left(\frac{4.63}{1,503}\right)(100) = 0.308\%$$

DISTRIBUTION

UC-70 (359)

DOE/FFTFPO (5)

Director

DOE/RRT-HQ (3)
Mail Stop B-107
Washington, DC 20545

CR Cooley
OP Gormley
CA Heath

DOE/Columbus Program Office (5)
505 King Avenue
Columbus, OH 43201

JO Neff (3)
Chief Patent Attorney (2)

HEDL (30)

SD Atkin	W/A-6	ED Jenson	W/A-6
RJ Cash	W/A-6	RL Knecht	W/A-40
JM Dahlke	W/C-115	RD Leggett	W/E-5
RB Davis	W/A-6	WE Roake	W/C-16
EA Evans	W/C-23	WF Sheely	W/A-62
RE Einziger	W/A-6	ET Weber	W/E-9
VJ Ferrell	W/A-6	JE Weber	W/E-1
RL Fish	W/A-6	RE Woodley	W/A-6
RL Gibby	W/JAD-7	N. Wynhoff	W/A-6
SE Girault	W/A-6	HH Yoshikawa	W/C-44
LM Henricks	W/A-6	Central Files (5)	W/C-110
DA Himes	W/A-6	Publ Services (2)	W/C-115
CW Hunter	W/E-10		

Office of Nuclear Waste Isolation (5)
505 King Avenue
Columbus, OH 43201

JA Carr

Battelle Columbus Laboratories (3)
505 King Avenue
Columbus, OH 43201

RW Klingensmith
DE Stellrecht
V. Pasupathi

☆ U. S. Government Printing Office: 1981—797-977/200